Title
Gyrokinetic simulations of turbulence in the near-edge of fusion plasmas

Author
Neiser, Tom

Publication Date
2019

University of California
Los Angeles

Gyrokinetic simulations of turbulence in the near-edge of fusion plasmas

A dissertation submitted in partial satisfaction
of the requirements for the degree
Doctor of Philosophy in Physics

by

Tom Frederik Neiser

2019

Abstract of the Dissertation

Gyrokinetic simulations of turbulence in the near-edge of fusion plasmas

by

Tom Frederik Neiser
Doctor of Philosophy in Physics
University of California, Los Angeles, 2019
Professor Frank S Jenko, Co-chair
Professor Troy A. Carter, Co-chair

The main purpose of this thesis is the validation of the gyrokinetic method in the near-edge region of L-mode plasmas. Our primary finding is that gyrokinetic simulations are able to match the heat-flux in the near-edge region of an L-mode plasma at $\rho = 0.80$ and $\rho = 0.90$ within the combined statistical and systematic uncertainty σ of the experiment at the 1.6σ and 1.3σ levels, respectively. At $\rho = 0.95$, gyrokinetic simulations are able to match the total experimental heat flux with nominal experimental parameters. In the big picture, this successful validation exercise helps push the gyrokinetic validation frontier closer to the L-mode edge region.

In the course of this validation study, we make three secondary findings that may be helpful to the fusion community. First, the current heuristic rules for the relevance of multi-scale effects appear to be on the cautious side. Multi-scale simulations at $\rho = 0.80$ suggest that single-scale simulations can be sufficient in a scenario when multi-scale effects are expected. This is helpful, because it could increase the realm of applicability of single-scale simulations, which are computationally more affordable than multi-scale simulations. Second, the effect of edge $\boldsymbol{E} \times \boldsymbol{B}$ shear is found to become important already in the near-edge (at $\rho = 0.90$) rather than at larger radial positions. This was unexpected and is relevant for future simulations in the near-edge. Third, nonlinear simulations at $\rho = 0.90$ find a hybrid ion temperature gradient (ITG)/ trapped electron mode (TEM) scenario, which was

not obvious from linear simulations due to the stability of ITG modes. This could also be an important result for spherical tokamaks, where ITG modes are more often linearly stable than in conventional tokamaks.

The dissertation of Tom Frederik Neiser is approved.

George J Morales

Mark R Morris

Troy A. Carter, Committee Co-chair

Frank S Jenko, Committee Co-chair

University of California, Los Angeles

2019

To my family

Table of Contents

List of Figures

List of Tables

ACKNOWLEDGMENTS

I thank my advisors Frank Jenko and Troy Carter for their guidance, patience and friendship. Among many things, I thank Frank for identifying intrinsic motivation as the primary drive for research productivity, for teaching me to find a balance between perfectionism and pragmatism, for his readiness to derive concepts and methods with pen and paper during meetings, and for nurturing a collegial atmosphere during many group lunches. I thank Troy for watching over me throughout my entire graduate career, for teaching me some of his depth and breadth of plasma physics and for giving the right impulses at the right times for fruitful collaborations and directions for further research. I find both Frank and Troy's leadership of large groups of experimental and theoretical plasma physicists inspiring.

I thank George Morales for teaching me plasma physics in a very clear, patient and always helpful manner. The plasma physics course, which included careful reading of original research papers and presentation of a conference-style talk, has prepared me well for my graduate career and beyond. I have benefited from insightful questions asked by George during the plasma physics course and during plasma physics colloquia.

I thank Mark Morris for many helpful discussions on topics of interest in both plasma physics and astrophysics. The UCLA Department of Physics and Astronomy provides an academic environment where curiosities are easily piqued and also easily satisfied. I thank Mark for contributing to this ideal research environment, for providing helpful questions and comments on a manuscript, and for encouraging the continued pursuit of unsolved puzzles.

I thank Lothar Schmitz for many helpful discussions regarding the behavior of plasma in the edge and, in particular, the capture and description of its experimental properties.

I thank Daniel Told, Gabriele Merlo, Alejandro Bañón Navarro, Martin Weidl and Qingjiang Pan, Tobias Görler, Nathan Howard, Chris Holland, Walter Guttenfelder, Craig Petty, Punit Gohil, Wayne Solomon for helpful questions and comments surrounding this work.

Lastly, I am grateful to Elizabeth Mills, Hector Garcia, Allic Sivaramakrishnan, Maurice

Maurer, Paul Crandall, Brett Friedman, Julian Gold, Adam Azzam, Josh Samani and many others for making my life in graduate school as enjoyable as it was.

This work is supported by the United States Department of Energy (DOE) under award number DE-SC0016073. The computational effort was conducted at NERSC, a DOE Office of Science User Facility supported under contract DE-AC02-05CH11231. The experimental work at DIII-D was supported by the US DOE under contract numbers DE-FG02-08ER54984 and DE-FC02-04ER54698.

Vita

2000–2006	Gymnasium Tegernsee, Tegernsee, Germany
2006–2007	International Baccalaureate, SCECGS Redlands, Sydney, Australia
2008–2011	Bachelor of Science & Associate of the Royal College of Science (Physics with Theoretical Physics), Imperial College London, London, UK
2011–2014	Master of Science (Physics), UCLA, Los Angeles, California, USA
2011–2019	Teaching Assistant and Graduate Student Researcher, Department of Physics and Astronomy, UCLA

Publications and Presentations

Gyrokinetic GENE simulations of DIII-D near-edge L-mode plasmas, **T. F. Neiser**, F. Jenko, T. A. Carter, L. Schmitz, D. Told, G. Merlo, A. Bañón Navarro, P. C. Crandall, G. McKee and Z. Yan. Paper accepted to *Physics of Plasmas* (2019). arXiv:1808.06607

Neutrino Star Cosmology, **T. F. Neiser**. Paper submitted to peer review (2019). doi: 10.20944/preprints201806.0175.v1

Gyrokinetic simulations of DIII-D near-edge L-mode plasmas, **T. Neiser**, F. Jenko, T. Carter, L. Schmitz *et al.*, Talk at 59th Meeting of the American Physical Society (APS) Division of Plasma Physics (DPP) (2017). Bibcode: 2017APS..DPPYO4008N

Multi-scale Simulations of DIII-D near-edge L-mode plasmas, **T. Neiser**, F. Jenko, T. Carter, L. Schmitz *et al.*, Talk at 58th APS DPP (2016). Bibcode: 2016APS..DPPTO9011N

ETG-dominated transport regimes in near-edge DIII-D L-mode plasmas: Validation of multiscale gyrokinetic simulations, **T. Neiser**, F. Jenko, L. Schmitz *et al.*, Talk at 57th APS DPP (2015). Bibcode: 2015APS..DPPUO5011N

Indirect evidence for a hybrid ITG/TEM scenario in nonlinear simulations of a DIII-D near-edge L-mode plasma, **T. F. Neiser**, F. Jenko, T. A. Carter, L. Schmitz *et al.*, Poster at 61st APS DPP (2019).

Cosmological implications of a degenerate antineutrino star, **T. F. Neiser**, Poster at 233rd Meeting of the American Astronomical Society (2019). Bibcode: 2019AAS...23334908N

Characterizing near-edge DIII-D L-mode plasmas with gyrokinetic GENE simulations, **T. F. Neiser**, F. Jenko, T. A. Carter, L. Schmitz *et al.*, Poster at 60th APS DPP (2018). Bibcode: 2018APS..DPPN11064N

GENE simulations of near-edge L-mode plasmas in DIII-D: Can gyrokinetics recover the experimental heat fluxes?, **T. F. Neiser**, F. Jenko, T. A. Carter, L. Schmitz *et al.*, Poster at U.S. Transport Task Force Meeting, San Diego (2018). doi: 10.13140/RG.2.2.17287.09129

Computational analysis of two-fluid edge plasma stability in tokamak geometries, **T. Neiser**, D. Baver, T. Carter, J. Myra, P. Snyder, M. Umansky, Poster at 55th APS DPP (2013). Bibcode: 2013APS..DPPPP8034N

Two-fluid edge plasma stability analysis in divertor tokamak geometry, **T. Neiser**, D. Baver, T. Carter, J. Myra, P. Snyder, M. Umansky, Poster at 54th APS DPP (2012). Bibcode: 2012APS..DPPBP8150N

CHAPTER 1

Introduction

> “With each decade the number and the significance of the means increase, whereby mankind learns directly through ... physics to make nature useful for its own purpose.” – Max Planck, *Eight Lectures on Theoretical Physics* (1909)

1.1 Motivation for Fusion Energy Research

Almost a century ago, the prospect of using nuclear fusion for energy production on earth was first proposed in a lecture by Arthur Eddington [1]. In trying to explain the source of thermal energy that is released by the stars, Eddington used the recently established fact[*] that the mass of Helium is 4.003 u while the mass of a Hydrogen atom is 1.008 u, where u is the atomic mass unit. He proposed that four Hydrogen atoms combine to create one Helium atom in the sun, with the mass difference $\delta m \approx 0.029$ u transforming to kinetic energy by Einstein’s mass-energy relation $E = (\delta m)c^2$, where c is the speed of light. In the same lecture, Eddington immediately recognized the potential benefit of this energy source to mankind:

> “A star is drawing on some vast reservoir of ... subatomic energy which, it is known exists abundantly in all matter; we sometimes dream that man will one day learn how to release it and use it for his service.” – Arthur Eddington (1920)

The actual reaction in the sun involves neutrinos and positrons, which had not been discovered yet at the time of Eddington’s lecture, and the most common branched chain reaction

---

[*] This fact was discovered by Francis W. Aston, a colleague of Eddington at Cambridge.

in the sun can be summarized as

$$4{}_1^1\mathrm{H} \rightarrow {}_2^4\,\mathrm{He} + 2{}_1^0e^+ + 2\nu_e + 26.7\ \mathrm{MeV}\,. \tag{1.1}$$

Note that a considerable amount of energy is released in a nuclear reaction, which dwarves the typical change in enthalpy of a chemical reaction. For example, the combustion of a natural gas such as methane gives

$$\mathrm{CH_4} + 2\mathrm{O_2} \rightarrow \mathrm{CO_2} + 2\mathrm{H_2O} + 8.40\ \mathrm{eV}\,. \tag{1.2}$$

Therefore, each fusion reaction releases $\sim 10^6$ times more energy than a typical chemical reaction. For fission, the gain in released energy for each reaction is even higher ($\sim 10^7$), since the electrostatic repulsion between protons in the nucleus energetically favors fission to fusion. Therefore, while chemical energy is powering the majority of society today, the controlled release of nuclear energy would represent a significant increase in resource efficiency. Fission reactors are already in operation today and are meeting the *majority* of the energy needs of three[†] countries, e.g. France. However, fission comes at the cost of long-term radioactive waste, non-proliferation concerns and intrinsic criticality of fission fuel in the simplest reactor designs. Fusion reactions, on the other hand, are intrinsically safe, do not give rise to long-lived radioactive waste or proliferation concerns, and rely on abundant resources. Moreover, high-energy fusion neutrons could break down and thereby "burn up" some of the long-term radioactive waste from fission [2, 3]. Therefore, in order to establish energy security on a planet with limited resources, nuclear fusion provides a viable long-term alternative to fossil fuels.

[†] https://pris.iaea.org/PRIS/WorldStatistics/NuclearShareofElectricityGeneration.aspx; date accessed: 10/5/18

1.2 Successes of Fusion Energy Research

While nuclear fusion is an abundant phenomenon in the universe[‡], it is challenging to induce the conditions necessary for fusion on earth. Currently, the conditions for a substantial number of fusion reactions are routinely met in experiments that use one of two confinement approaches, either inertial confinement (10^{16} fusion reactions/shot [5]) or magnetic confinement (10^{19} fusion reactions/sec [6]). Inertial confinement relies on the inertia of the fusion fuel to contain a very high, externally supplied pressure for long enough to create a substantial number of fusion reactions. The magnetic confinement approach uses magnetic fields to confine particles at relatively low pressures compared to inertial confinement, but for a much longer time, and has so far been more successful for potential fusion energy generation than the inertial confinement approach. The magnetic confinement approach itself benefits from two competing designs, namely the stellarator and the tokamak design[§], which both show promise for future fusion reactors. In the following paragraphs, the major successes of magnetic fusion energy research are highlighted.

Magnetic confinement geometry

The tokamak is presently the most successful tool in achieving sustained nuclear fusion reactions on earth. The design is so successful, because it is able to balance the pressure gradient with magnetic forces without much complexity. This is briefly motivated below.

In a purely toroidal magnetic field configuration the central field scales as $B \propto 1/R$, where R is the major radius. This magnetic field gradient creates a particle drift,

$$\boldsymbol{v}_{\nabla \boldsymbol{B}} = \frac{\mu \boldsymbol{B} \times \nabla \boldsymbol{B}}{q B^2}\,, \tag{1.3}$$

where q is the electric charge of the particle, μ is the magnetic moment and $\boldsymbol{B}$ is the purely toroidal magnetic field. Note that the above equation for the drift velocity is charge-

---

[‡] See for example big bang nucleosynthesis [4], the detonation of white dwarf stars in type Ia supernovae due to Carbon fusion, and stellar nucleosynthesis.

[§] The idea for the tokamak was developed by Soviet physicists Igor Tamm, Andrei Sakharov and Oleg Lavrentiev. ‘Tokamak’ is an acronym of the Russian words for ‘toroidal magnetic chamber’.

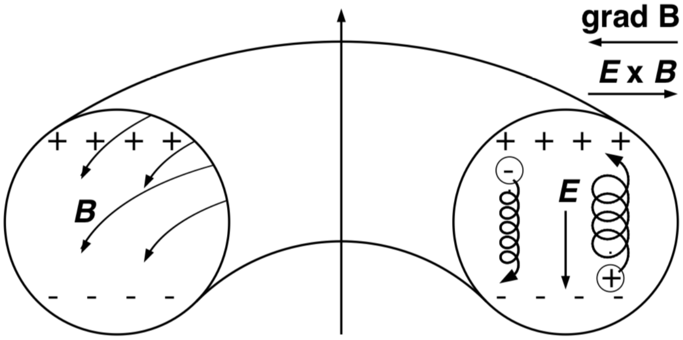

Figure 1.1: Schematic diagram of a purely toroidal magnetic field (i.e. without a poloidal magnetic field component). In the above configuration, ions drift upwards and electrons drift downwards due to the magnetic field curvature and gradient. This creates an electric field that leads to rapid de-confinement of the plasma via $\boldsymbol{E} \times \boldsymbol{B}$ drifts. Magnetic fields with both toroidal and poloidal components, as shown in Fig. 1.2 below, are able to compensate for these drifts. Reprinted with permission from [7].

dependent, causing the ions to drift in a vertical direction opposite to the electrons (see Figure 1.1). This establishes a vertical electric field $\boldsymbol{E}$ that creates a secondary drift velocity,

$$\boldsymbol{v}_{\boldsymbol{E}} = \frac{\boldsymbol{E} \times \boldsymbol{B}}{B^2}\,, \tag{1.4}$$

which always points radially outwards and is charge independent. Therefore a purely toroidal magnetic field would cause rapid deconfinement of the plasma. This problem can be remedied by adding a poloidal component to the magnetic field (B_θ), for example with a toroidal current in the plasma (j_ϕ). The resulting Lorentz force on current-carrying plasma can balance the force on the plasma due to the radial thermal pressure gradient and confine the plasma,

$$\nabla_r\, p = \boldsymbol{j}_\phi \times \boldsymbol{B}_\theta\,. \tag{1.5}$$

This is a key principle behind magnetic confinement and has contributed to the success of magnetic confinement fusion.

In a tokamak, the toroidal current is created by the transformer principle directly inside the plasma. In a stellarator, the toroidal current is supplied together with the poloidal current by external magnetic field coils, which complicates the design but allows for easier access to steady-state operation [9]. Both the tokamak and stellarator are currently under

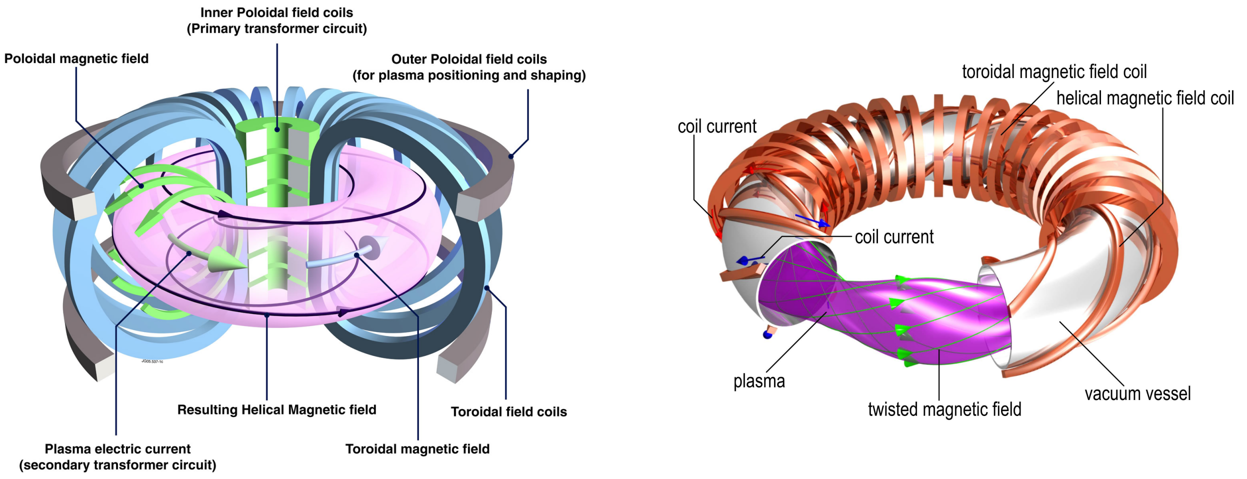

(a) Tokamak.

(b) Stellarator.

Figure 1.2: Schematic diagram of a tokamak and a stellarator. Figure a) shows the schematic design of a tokamak, where the poloidal component of the magnetic field is generated by a plasma current that is induced using the transformer principle (figure courtesy of EUROfusion [8]). Figure b) shows the schematic design of a stellarator, where both the toroidal and poloidal components of the magnetic field are supplied by currents external to the plasma (figure courtesy of Christian Brandt and the Max Planck Institute for Plasma Physics).

active investigation as promising candidates for future fusion reactors.

Lawson criterion

In order to achieve break-even, the fusion power produced must be greater than or equal to the power losses of the plasma, independent of the confinement method. This can be summarized by the inequality

$$P_f \geq \frac{W}{\tau_E}\,, \tag{1.6}$$

where $W = 3nT$ is the total energy density of the plasma, τ_E is the total energy confinement time and the fusion power density is defined as

$$P_f = n_{\mathrm{D}} n_{\mathrm{T}} \langle \sigma v \rangle E_{\mathrm{ch}}\,, \tag{1.7}$$

where n_{D} and n_{T} are the number densities of Deuterium and Tritium ions, respectively. Moreover, $\langle \sigma v \rangle$ is the reactivity and E_{ch} is the energy of charged fusion products (e.g. Deuterium-Tritium fusion produces an alpha particle with $E_{\mathrm{ch}} =$ 3.5 MeV). In the optimum power configuration, the total number density n is made up in equal parts of Deuterium and Tritium, $n_{\mathrm{D}} = n_{\mathrm{T}} = n/2$, giving

$$P_f = \frac{1}{4} n^2 \langle \sigma v \rangle E_{\mathrm{ch}} \tag{1.8}$$

Solving for $n\tau_E$ and multiplying by T gives the following lower limit on the triple product

$$nT\tau_E \geq \frac{12T^2}{\langle \sigma v \rangle E_{\mathrm{ch}}} \,. \tag{1.9}$$

The triple product is a useful figure of merit for various tokamak designs. This is because close to breakeven confinement time τ_E is empirically found to scale as $\tau_E \propto n^{1/3}/P_f^{2/3}$ [10] and $\langle \sigma v \rangle \propto T^2$ (or $P_f \propto n^2 T^2$). As a result, the triple product is independent of density and only weakly dependent on temperature, $nT\tau_E \propto T^{-1/3}$. Therefore the triple product can be used to compare and optimize fusion performance across various operating parameters and tokamak designs. Using reactivities from [11, see Table VII], the lower limit of the triple product is plotted for candidate fusion reactions in Figure 1.3. The most promising reaction for first-generation fusion reactors is the fusion of Deuterium and Tritium (D-T fusion),

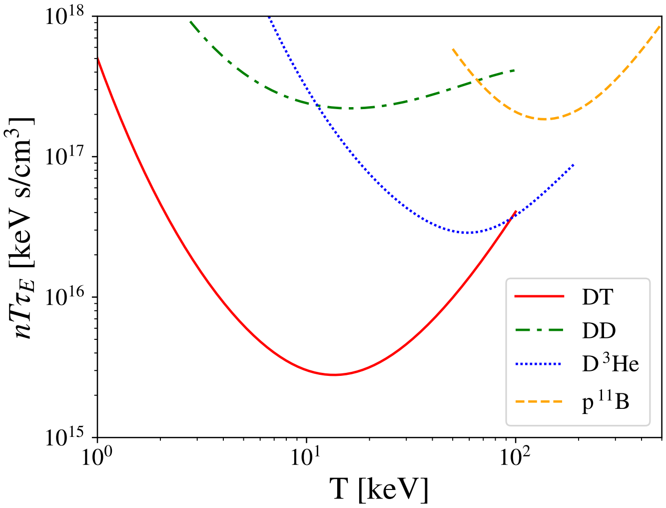

Figure 1.3: Triple product as a function of ion temperature for the most promising fusion fuels. Note that D-T fusion is the favored reaction with a minimum triple product for breakeven found at $T \approx 14$ keV.

$${}^2_1\mathrm{D} + {}^3_1\mathrm{T} \rightarrow {}^4_2\mathrm{He} + {}^1_0\mathrm{n} + 17.6 \ \mathrm{MeV}\,. \tag{1.10}$$

The triple product as a function of temperature for D-T fusion has a minimum at $T = 13.5$ keV or 1.57×10^8 K. Therefore, for a D-T plasma to become self-sustaining at this optimum temperature, the following criterion must be satisfied,

$$nT\tau_E \gtrsim 3 \times 10^{15} \frac{\mathrm{keV\,s}}{\mathrm{cm}^3} \,. \tag{1.11}$$

This criterion is a modern version of the Lawson criterion for D-T fusion [12]. While the Lawson criterion has not been met in a tokamak yet[¶], the triple product $nT\tau_E$ has doubled every 1.8 years in fusion experiments from 1970 to the early 2000s (see Fig. 1.4). This trend has not continued as steeply after the early 2000s, mostly due to delays in the construction of ITER. Note that ITER, currently under construction in southern France and on schedule to achieve first plasma in December 2025, is predicted to satisfy the Lawson criterion with D-T fusion starting in 2035.

First-generation fusion reactors are likely to employ D-T fusion for power generation. Later generations of fusion reactors may be able to employ neutron-poor fusion reactions such as

$${}^2_1\mathrm{D} + {}^3_2\,\mathrm{He} \rightarrow {}^4_2\,\mathrm{He} + {}^1_1\,\mathrm{p} + 18.4\ \mathrm{MeV} \,, \tag{1.12}$$

where some D-D side-reactions can produce neutrons. Even later generations of fusion reactors could employ aneutronic reactions such as

$${}^1_1\mathrm{p} + {}^{11}_5\,\mathrm{B} \rightarrow 3\,{}^4_2\mathrm{He} + 8.68\ \mathrm{MeV} \,, \tag{1.13}$$

which could benefit from reduced radioactive shielding and handling requirements due to low neutron fluxes. Aneutronic fusion could also rely on methods for direct conversion of thermal energy to electrostatic energy [13], perhaps similar to direct conversion methods that improve neutral beam injection (NBI) efficiency [14] (although some innovations in tokamak divertor design will be required [15]).

[¶] Note the Lawson criterion has already been met on earth after dedicated research into nuclear fusion bombs, starting with the "Ivy Mike" test of the first full-scale hydrogen bomb in 1952.

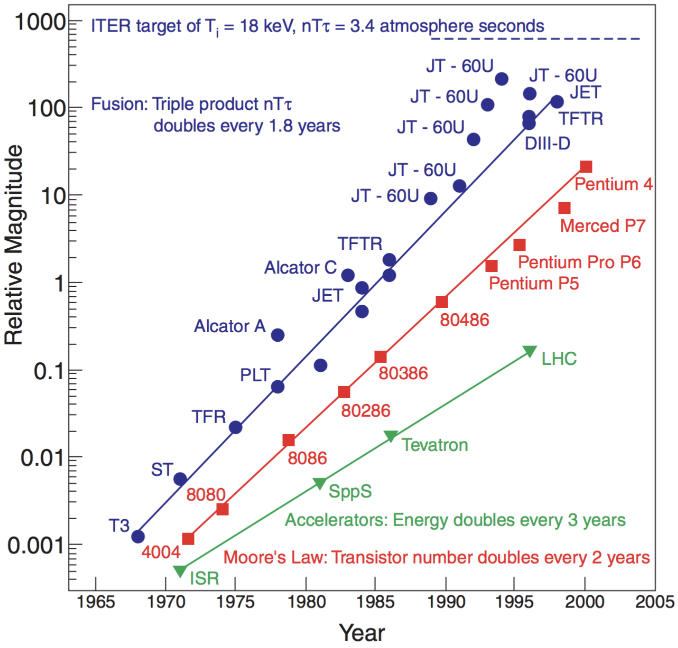

Figure 1.4: Relative magnitude of the triple product in magnetic fusion experiments. The triple product has doubled every 1.8 years from 1970-2000 and is predicted to satisfy the Lawson criterion with ITER in 2035. Reprinted with permission from [16].

Energy confinement time

Particularly noteworthy throughout the entire history of fusion energy research to date are the improvements in energy confinement time with, among other things, the successful application of scaling laws. For example, the energy confinement time in a stellarator of minor radius a and toroidal field strength B scales as

$$\tau_E \propto a^{2.33} B^{0.85}. \tag{1.14}$$

This particular scaling is comparable to the Bohm-type scaling that was found in early tokamak plasma experiments. In high-confinement operation, the more favorable gyro-Bohm scaling has been observed. The origin of these two scaling laws are briefly described below.

In a cylindrical device with minor radius a and length L, the degradation of particle confinement with time is generally exponential,

$$\tau_E \approx \frac{N}{dN/dt} = \frac{n\pi a^2 L}{\Gamma_\perp 2\pi a L} = \frac{na}{2\Gamma_\perp}\,, \tag{1.15}$$

where N is the number of ion-electron pairs, n is the number density and $\Gamma_\perp$ is the cross-field particle flux with diffusion coefficient D,

$$\Gamma_\perp = -D\,\nabla n\,. \tag{1.16}$$

The normalized density gradient can be approximated to be on the order of the machine size [17, Eq. 7.50],

$$\frac{\nabla n}{n} \approx \frac{1}{a}\,. \tag{1.17}$$

The above two equations show that the confinement time has the following proportionality

$$\tau_E \propto \frac{a^2}{D}\,. \tag{1.18}$$

We can determine the diffusion constant by assuming that transport is dominated by turbulence due to drift-wave instabilities. Typical drift-wave frequencies are given by [18, Eq. 21.39]

$$\omega_{de} \approx \frac{k_\perp}{a}\frac{k_B T_e}{eB}\,, \tag{1.19}$$

where $k_\perp$ is the wavenumber of turbulent fluctuations perpendicular to the magnetic field. The turbulent diffusion constant is therefore

$$D \approx \frac{\omega_{de}}{k_\perp^2} = \frac{1}{k_\perp a}\frac{k_B T_e}{eB} \propto \frac{1}{k_\perp a}\frac{T_e}{B}\,. \tag{1.20}$$

Bohm diffusion is observed when these fluctuations are on the order of the minor radius, $k_\perp \approx \frac{1}{a}$, giving

$$\tau_E \propto \frac{a^2 B}{T_e}\,. \tag{1.21}$$

The more favorable gyro-Bohm diffusion is observed when fluctuations are caused by turbulence on the ion gyro-radius scale, $k_\perp \approx \frac{1}{\rho_i}$. This improves the confinement time by a factor $\frac{a}{\rho_i} \gtrsim 1000$,

$$\tau_E \propto \frac{a^2 B}{T_e} \left(\frac{a}{\rho_i} \right) . \tag{1.22}$$

Note that the increase of confinement time with an increase in magnetic field strength means that advances in performance of high-temperature, high-current superconductors can benefit fusion experiments in the future [19–21]. In fact, a doubling in the magnetic field strength can cause a 16-fold increase in the fusion power as follows[‖]. Assuming that fusion reactors operate at a given maximum thermal to magnetic pressure ratio due to instability limits,

$$\beta = \frac{n k_B T}{B_0^2 / 2\mu_0} , \tag{1.23}$$

the plasma can sustain four times the temperature if the magnetic field is doubled at constant β. Note that the fusion reaction rate $\langle \sigma v \rangle$ is approximately proportional to the square of the temperature at reactor relevant pressures and temperatures, $\langle \sigma v \rangle \propto T^2$. Therefore this four-fold increase in the temperature at constant β can increase the fusion power, $P \propto n^2 T^2$, by a factor of sixteen. Therefore, stronger magnetic fields lead to significantly improved reactor performance, such that nuclear fusion research benefits from advances in high temperature superconductivity [22, 23]. Scaling laws similar to the above example have been used to instruct the design of ITER. Based on current calculations, ITER will produce 10 times more fusion power than heating power supplied to the plasma when D-T plasma operation commences after 2035.

Understanding of Anomalous Transport

Transport in a tokamak was initially believed to be dominated by classical transport, which is driven by collisions. Specifically, the electrons were expected to undergo a random walk with a step size ρ_e and step frequency ν_{ei}, giving a diffusion constant

$$D = \nu_{ei} \rho_e^2 , \tag{1.24}$$

[‖] See a white paper by G. W. Hammett and W. Dorland, 2017; date accessed: 11/23/2018 where ρ_e is the electron gyro-radius,

$$\rho_e = \frac{\sqrt{k_B T_e m_e}}{eB}\,, \tag{1.25}$$

and ν_{ei} is the ion-electron collision frequency[**]. However, the measured diffusion constant is several orders of magnitude larger than the classical diffusion constant. Taking the effects of magnetic field curvature into account yields larger step sizes in the so-called "neoclassical transport" model, but still underpredicts the measured transport. The difference between observed transport levels and neoclassical predictions is called anomalous transport. One of the major successes of fusion energy research in the last two decades has been the identification of micro-turbulence as the likely origin of this turbulent transport (for reviews, see [24, 25]). Micro-turbulence associated with fluctuations in the electric field is called electrostatic turbulence, while fluctuations in the magnetic field give rise to electromagnetic turbulence. For instance, ion temperature gradient (ITG) [26–28], electron temperature gradient (ETG) [29–31] and trapped electron modes (TEMs) [32, 33] are known examples of electrostatic turbulence, while micro-tearing modes (MTMs) are examples of electromagnetic turbulence often seen in tokamaks with a low aspect ratio such as NSTX-U [34]; some of these types of turbulent modes will be discussed in more detail in the following chapter. While anomalous transport in the core of a tokamak has been successfully modeled with plasma simulations and compared to experiments, anomalous transport close to the edge region of a tokamak is still poorly understood and will be discussed in the next section 1.3.

1.3 Unsolved Puzzles of Fusion Energy Research

Historically, many advances have been made in fusion energy research since its inception in the late 1950s. However, there remain several unsolved problems on the cutting edge of both the engineering and physics efforts. This work will focus on the physics side, namely on advancing our understanding of micro-turbulence and transport, since this is an important problem pertinent to the energy confinement time of fusion experiments. Modern super-

---

[**] Note that the ion diffusivity is equal to the electron diffusivity due to quasi-neutrality of the plasma.

computers today are capable of modeling turbulence with a high degree of realism that is steadily increasing together with code and computational hardware development. Three major unsolved problems in the study of turbulence and transport are highlighted below.

What is the mechanism for the L-H transition?

Development of a self-consistent theoretical description of the transition into a high-confinement regime (H-mode) with an increase in heating power above a certain threshold is one of the major remaining puzzles of fusion energy research. For a long period of time, the only operational mode accessible in tokamak experiments was the so-called low-confinement mode (L-mode). This mode is characterized by strong turbulence and a general degradation of confinement time with an increase in heating power. Physically, this is caused by the increase of turbulence due to micro-instabilities that are driven by steeper temperature gradients and pressure gradients associated with higher heating power. With an improvement in heating

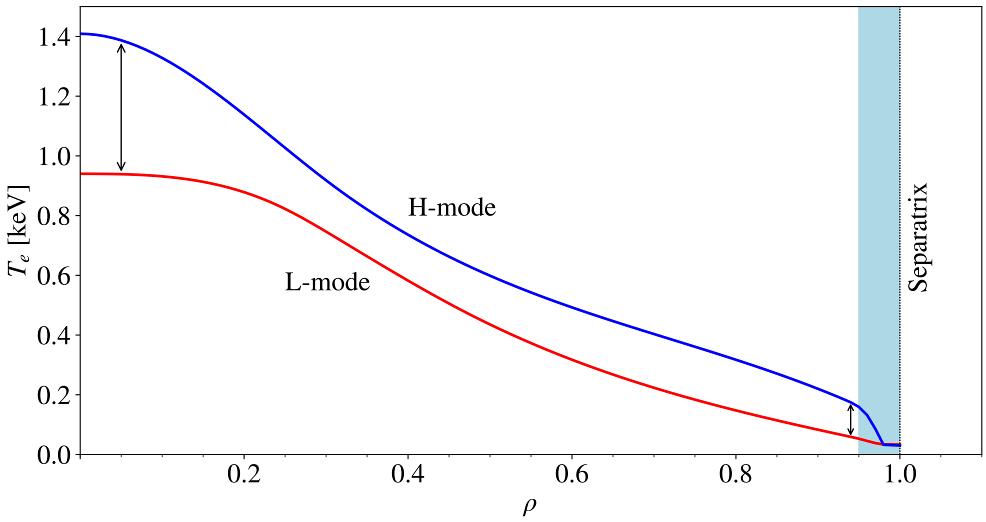

Figure 1.5: Electron temperature profiles of L-mode and H-mode phases of DIII-D discharge #153624. The L-mode phase (data shown for $t = 2400$ ms) shows a relatively smooth electron temperature profile throughout the entire confined plasma, $0.0 \leq \rho \leq 1.0$, where $\rho = (\Phi/\Phi_{\text{edge}})^{1/2}$ is the toroidal flux radius and Φ_{edge} is the toroidal flux at the separatrix. After transition into H-mode (data shown for $t = 2560$ ms), a temperature pedestal develops in the shaded region ($0.95 \leq \rho \leq 1.0$). Due to profile consistency, the pedestal supports $\sim 50\%$ higher core temperatures than L-mode and significantly improves future fusion reactor performance.

power technology, namely the introduction of neutral beam injection (NBI) and more powerful ion-cyclotron heating (ICRH) systems, a high confinement regime was discovered in 1982 [35]. Paradoxically, it was found that above a certain threshold in heating power (P_{th}), a transport barrier develops in the edge region that can support steep pressure and temperature gradients. In the core of a tokamak, temperature and density profiles generally adopt qualitatively similar shapes independent of heating and re-fueling of the plasma, likely due to strong turbulent feedback mechanisms. Therefore, the top of the steep edge gradient acts as a "pedestal" for the core profile [36]. This allows core temperatures in H-mode that are approximately 50% higher than in L-mode (for a realistic example, see Fig. 1.5). Similarly, the energy confinement τ_E is approximately twice as large in H-mode than in L-mode [37]. Therefore, the discovery of H-mode, which has since been reproduced in all major tokamaks and is targeted in the experimental campaign of ITER [38], can be counted among one of the great successes of experimental fusion energy research. At the same time, a self-consistent theoretical description of the L-H transition remains one of the major unsolved problems in the field [38–40].

The present understanding of the transition mechanism relies on the Reynold's stress and can be summarized as follows (for a review, see [41]). In the slab model, where x is a radial coordinate, y is poloidal and z is toroidal, the momentum balance equation gives

$$\frac{\partial u_y}{\partial t} + \nabla_x \left(u_x u_y\right) = -\frac{1}{\rho}\nabla_y P + \frac{1}{\rho}\left(\boldsymbol{j} \times \boldsymbol{B}\right)_y \tag{1.26}$$

After averaging over the flux surface (i.e. over the y-coordinate), the right hand side of the momentum balance cancels, giving

$$\frac{\partial u_y}{\partial t} + \nabla_x \left(u_x u_y\right) = 0 \tag{1.27}$$

Expanding the plasma flow into an average (u_0) and fluctuating component (u_1) gives

$$u = u_0 + u_1\,. \tag{1.28}$$

Plugging this perturbative flow into the flux-surface averaged momentum balance equation gives

$$\frac{\partial u_{0y}}{\partial t} + \nabla_x \langle u_{1x} u_{1y} \rangle = 0\,, \tag{1.29}$$

where the second term is known as the Reynold's stress tensor $R_{xy} = \langle u_{1x} u_{1y} \rangle$. Turbulence itself is thought to induce the correlated fluctuations with a spatial variation due to the background gradients, $\nabla_x \langle u_{1x} u_{1y} \rangle$. This term supplies the non-zero Reynold's stress that leads to a change in the poloidal laminar flow velocity, $\frac{\partial u_{0y}}{\partial t}$. Therefore edge turbulence could induce a poloidal shear flow layer with the Reynold's stress mechanism [42–44].

Typically, a significant shear flow layer is found at $\rho \geq 0.95$, where $\rho = (\Phi/\Phi_{\text{edge}})^{1/2}$ is the toroidal flux radius and Φ_{edge} is the toroidal flux at the separatrix (see also Fig. 1.5). This shear flow stretches the turbulent eddies in the poloidal direction and reduces their radial size, and thus reduces the radial turbulent scale length and the associated radial heat transport. By hampering the efficiency of turbulent heat transport, the flow shear creates a transport barrier that can support steep pressure and temperature gradients in the edge region. However, there is a limit to the size of the pedestal, which is dictated partly by the pressure gradient. Above a certain pressure gradient, a ballooning mode becomes unstable and triggers an edge localized mode (ELM) that causes rapid deconfinement of the plasma and collapses the pedestal. Large ELMs generate potentially damaging heat fluxes towards the plasma-facing components (PFCs) of large fusion experiments. On the other hand, ELMs have the benefit of purifying the plasma by ‘flushing out’ impurities imported from PFCs and the Helium ash that gradually builds up in the plasma. This mixed blessing has led to the desire to trigger small amplitude, high-frequency ELMs that are called “grassy” due to the shape of the plasma's heat-flux time trace. Moreover, research into a new confinement regime that is quiescent in ELMs has recently led to the theoretical prediction and experimental confirmation of a “Super H-mode” [45]. Super H-mode is now predicted to help ITER achieve its mission and could help instruct design of an improved compact pilot plant [46]. As these examples show, there are many potential performance improvements to be gained from studies of the L-H transition. While our understanding of the L-H transition has significantly improved over the years, a self-consistent theoretical picture has not yet emerged [38, 40].

When can multi-scale interactions no longer be ignored?

It has become apparent that interactions between micro-turbulent modes at large and small scales (multi-scale effects) are sometimes important. The micro-turbulence modes usually seen in the core are Ion Temperature Gradient (ITG), Electron Temperature Gradient (ETG) and Trapped Electron Modes (TEM). In the past, it was thought that experimentally relevant heat flux is mainly carried by TEM and ITG modes [25], because these modes transport energy on scales larger than the ion gyroradius ($k_\perp \rho_i \lesssim 1$), while ETG modes ($k_\perp \rho_i \gg 1$) transport energy on much smaller scales. However, gyrokinetic simulations in the early 2000s by Jenko and Dorland predicted that ETG modes can create radially elongated streamers that can contribute experimentally relevant heat transport [29–31]. This was later demonstrated by observations at the National Spherical Torus Experiment (NSTX) [47] and DIII-D [48]. However, it is not clear how ETG streamers interact with large-scale modes. In principle, this can be answered by multi-scale simulations that resolve the important wavenumber range for both ion- and electron-scale turbulence. Pioneering multi-scale simulations with a reduced mass ratio ($\sqrt{m_i/m_e} \approx 20$) and simplified geometry have found a heuristic rule that can gauge the relevance of the ETG-scale contribution to the overall heat transport [49–52]. More recent multi-scale simulations with realistic mass ratio and geometry have found that the degree of instability of ITG modes is a critical parameter determining the degree of cross-scale interactions [53–55]. These multi-scale simulations have instructed a recent model for saturation of multi-scale turbulence by zonal flow mixing, which has given rise to another potentially useful heuristic rule for gauging the importance of multi-scale interactions using linear simulations [56]. Since these heuristic rules provide useful physical insight and can save computational resources, it is helpful to validate these rules with further multi-scale simulations.

What is the nature of turbulent transport in the L-mode edge?

In order to better understand the L-H transition, it is instructive to study an L-mode phase in the near-edge region immediately preceding such a transition. The L-mode phase serves as initial condition for the transition, and turbulence in the edge region in particular is thought to supply the Reynold's stress that establishes the transport barrier in the H-mode edge. Additionally, predictions of turbulent L-mode profiles are needed for vertical stabilization of the plasma during current ramp-up and ramp-down phases in ITER [57]. However, while gyrokinetic simulations in the cores of both H-mode and L-mode plasmas have been successfully validated with experimental data, and similar success has been reported just inside the pedestal of H-mode, gyrokinetic simulations of the L-mode edge have proven difficult to validate. For instance, several simulations of DIII-D discharges with the GYRO code [58] have been in good agreement in the L-mode core, but have under-predicted the heat flux in the range $\rho \geq 0.75$ [59, 60]. This has raised questions on whether a systematic 'shortfall' in gyrokinetic heat flux predictions exists and if gyrokinetics can accurately recover the experimental heat fluxes in the near-edge region. Therefore the reasons to undertake gyrokinetic simulations in the near-edge region of DIII-D L-mode plasmas are threefold: (i) to investigate the characteristics of turbulence that could potentially lead to the proposed Reynold's stress mechanism that generates the flow shear and initiates the L-H transition, (ii) to better understand the nature of micro-turbulence in the near-edge region, and (iii) as a validation exercise of the gyrokinetic simulation method with gyrokinetic codes.

1.4 Scope of the present work

This work validates gyrokinetics and characterizes microturbulence in a DIII-D L-mode plasma with the gyrokinetic turbulence code GENE (www.genecode.org). Specifically, it focuses on the near-edge[††] region of an L-mode plasma immediately preceding an L-H transition in order to better understand the behavior of turbulence preceding this phenomenon.

[††] Throughout this work, we loosely define the near-edge as $0.80 \leq \rho \leq 0.96$.

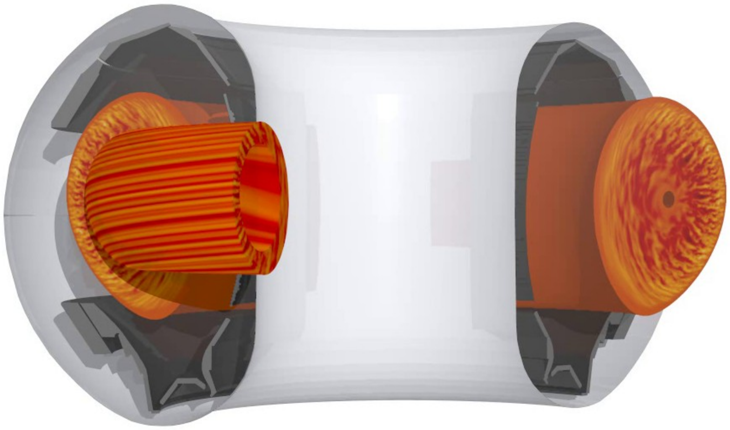

Figure 1.6: Global simulation of an ASDEX Upgrade plasma with GENE (figure courtesy of the Max Planck Institute for Plasma Physics).

This study focuses on three radial locations in the near-edge, namely at $\rho = 0.80$, $\rho = 0.90$ and $\rho = 0.95$. In an effort to better understand the relevance of multi-scale interactions in the near-edge region at $\rho = 0.80$, this work has carried out multi-scale simulations that are, to our knowledge, the first of their kind in the near-edge. At $\rho = 0.90$ and $\rho = 0.95$, the simulations are carried out only at large scales, i.e. only the ion scales rather than also the electron scales. Turbulence at these scales is sufficiently strong to suggest that multi-scale simulations, if they were computationally affordable at this location, would likely not find significant multi-scale effects.

The primary finding of this work is that gyrokinetic simulations are able to reproduce the heat flux observed in the experiment while changing the temperature gradient parameters within a reasonable uncertainty of the experiment. This finding pushes the gyrokinetic validation frontier closer to the L-mode edge region, where it may help to uncover the L-H transition mechanism.

There are three secondary findings associated with this work. (i) Current heuristic rules for the importance of multi-scale simulations appear to be on the cautious side. (ii) The effect of $\boldsymbol{E} \times \boldsymbol{B}$ shearing rate is already important in the near-edge (at $\rho = 0.90$) rather than at larger radial positions. (iii) We uncover a hybrid ITG/TEM scenario, which was unexpected from linear simulations due to the linear stability of the ITG modes. This could also be an important result for spherical tokamaks, where ITG modes are linearly stable more commonly than in conventional tokamaks due to the short connection length between the good and bad curvature regions.

This work is structured as follows. In Chapter 2, we introduce the main turbulent modes found in tokamak plasmas and the basic idea of the gyrokinetic method that can be used to study them numerically. In Chapter 3, we describe the key steps in the derivation of the gyrokinetic Vlasov equation solved by GENE. In Chapter 4, we describe the main numerical modeling tools of the GENE code relevant for this work, where the $\boldsymbol{E}\times\boldsymbol{B}$ shear, the GyroLES techniques, and the Sugama collision operator are particularly important. In Chapter 5, we describe the main linear and nonlinear simulation results at the three radial positions and discuss the successes and limitations of this work. Chapter 6 we summarize the main findings and provide directions for future research.

CHAPTER 2

Overview of turbulent transport in tokamaks

In this section we review the current understanding of turbulent transport in tokamaks and provide a motivation for gyrokinetic theory.

2.1 Micro-Turbulence

Micro-turbulence is generally assumed to be a major contributor to anomalous heat transport in tokamaks. Modes usually seen in the core are Ion Temperature Gradient (ITG), Electron Temperature Gradient (ETG) and Trapped Electron Modes (TEM). These modes are also expected in the near-edge region, in addition to resistive-ballooning modes (RBM) that can arise due to the high collisionality here [61–63]. In the following two sub-sections the underlying mechanism of these instabilities is summarized.

2.1.1 ITG/ETG instabilities

When the temperature gradient in a plasma is in the same direction as the magnetic field gradient (as is the case on the low-field or “bad-curvature” side of the tokamak), then perturbations in the plasma temperature can grow exponentially. This is known as the Rosenbluth-Longmire picture [26] (see Fig. 2.1). Recall that the ∇B-drift is directly proportional to the magnetic moment μ, which in turn is directly proportional to temperature $\mu = k_B T/B$. This proportionality can cause charge separation when there are temperature perturbations in a tokamak plasma as follows. The slower drift velocity of the lower temperature plasma drift is unable to maintain charge neutrality of the high temperature plasma, such that a net charge separation occurs on the high temperature side (see left panel of Fig. 2.1). This

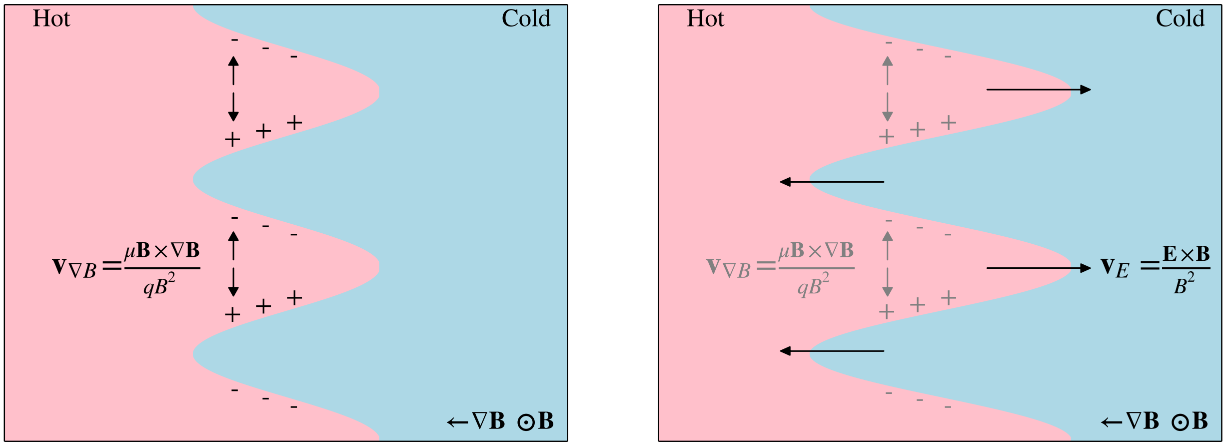

(a) $\nabla\boldsymbol{B}$-drift separates charge

(b) $\boldsymbol{E}\times\boldsymbol{B}$-drift amplifies perturbation

Figure 2.1: Schematic illustration of the ITG-instability using the Rosenbluth-Longmire picture. In the outboard midplane, which is in the "bad curvature" region of the plasma, perturbations are amplified by the simultaneous action of $\nabla\boldsymbol{B}$-drift and $\boldsymbol{E}\times\boldsymbol{B}$-drift. a) The $\nabla\boldsymbol{B}$-drift, which is directly proportional to temperature, causes a net charge separation on the hot plasma side. b) The resulting electric field creates an $\boldsymbol{E}\times\boldsymbol{B}$-drift that amplifies the perturbation amplitude.

charge separation will cause $E \times B$-drift flows that further amplify the temperature fluctuation, creating a positive-feedback loop that transports hot plasma radially outwards and cold plasma inwards (see right panel of Fig. 2.1). Fortunately, when the temperature gradient and magnetic field gradient point in opposite directions, as is the case on the high-field or "good-curvature" side of the tokamak, the $\boldsymbol{E}\times\boldsymbol{B}$ flow reduces the initial perturbation amplitude (see Fig. 2.2).

Note that in the slab model, ion acoustic drift-waves with long wavelengths parallel to and short wavelengths perpendicular to a uniform magnetic field can also create the necessary charge separation to drive the ITG instability. However, the effect of the non-uniform magnetic field illustrated above dominates the turbulent drive in a tokamak.

The electron temperature gradient driven modes are driven unstable in similar fashion to the ITG modes. While ITG modes also create streamers, these are often short-lived due to a predator-prey interaction with large-scale zonal flows [64].

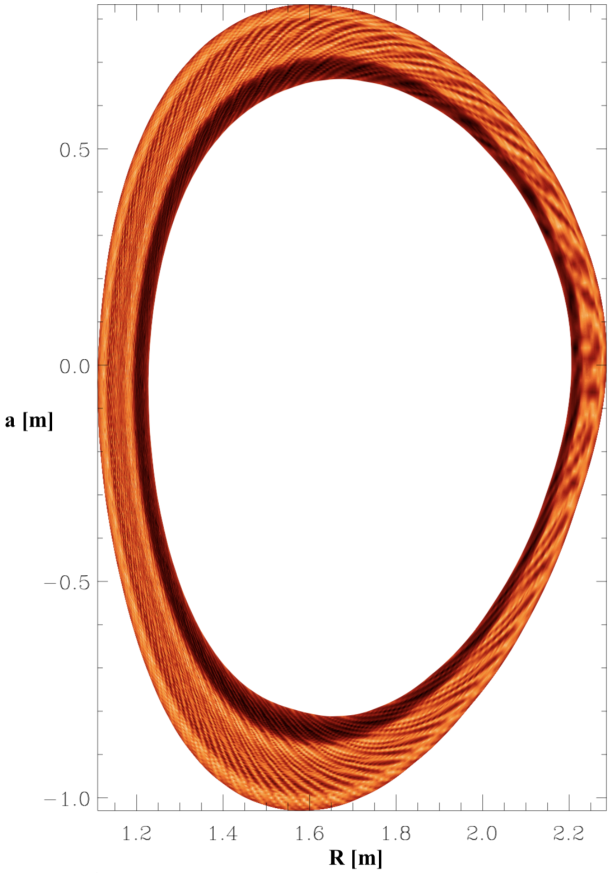

Figure 2.2: Toroidal representation of turbulent fluctuations in the electrostatic potential simulated with the GENE code (arbitrary units). The ITG instability can be seen to be most active in the outboard midplane, also known as the "bad curvature" region where the magnetic field gradient and temperature gradient align. The ITG instability is suppressed at the high-field side by the anti-alignment of magnetic field and temperature gradients.

2.1.2 TEM and RBM instabilities

The toroidal magnetic field gradient ($B_\phi \propto 1/R$) causes particles to become trapped in the low-field side of the tokamak. This can be illustrated briefly using the conservation of energy ϵ and the adiabatic invariance of the magnetic moment μ of a charged particle confined to a flux surface in a tokamak. At the low-field side of the tokamak, the energy of a charged particle can be written as

$$\epsilon = \frac{1}{2}mv_{\parallel,0}^2 + \frac{1}{2}mv_{\perp,0}^2 = \frac{1}{2}mv_{\parallel,0}^2 + \mu B_{\min}(\psi)\,, \tag{2.1}$$

where $B_{\mathrm{min}}(\psi)$ is the minimum field that the particle encounters at the low-field side of a flux surface ($\psi = \text{const.}$). All trapped particles meet the energy condition

$$\epsilon \leq \mu B_{\mathrm{max}}(\psi)\,, \tag{2.2}$$

where $B_{\mathrm{max}}(\psi)$ is the maximum magnetic field at the high-field side of a flux-surface. Therefore, the above two equations give the condition for trapping of

$$v_{\parallel,0} \leq v_{\perp,0}\sqrt{\frac{B_{\mathrm{max}}(\psi)}{B_{\mathrm{min}}(\psi)} - 1}\,. \tag{2.3}$$

The fraction of trapped particles can be shown to be

$$F = \sqrt{1 - \frac{B_{\mathrm{min}}(\psi)}{B_{\mathrm{max}}(\psi)}}\,. \tag{2.4}$$

Density fluctuations in the trapped particles can cause charge separation that is localized on the "bad-curvature" side of the tokamak. Therefore trapped electron modes (TEMs) are particularly effective at radial heat transport [32, 33]. TEMs are stabilized by collisionality, since collisions de-trap particles. However, TEMs are de-stabilized by higher gradients in electron temperature, similar to ETG modes. In addition, they are destabilized by steeper density gradients and generally oscillate in the electron diamagnetic direction.

Resistive-ballooning Modes (RBMs) are de-stabilized by higher collisionality, q-factor and gradients and oscillate in electron diamagnetic direction [61–63]. They are most virulent in the edge region, where the collisionality is high, and have been suspected to contribute to heat transport even in the near-edge region. They have long wavelengths, such that they are seen at low $k_y\rho_s$, and likely require global simulations [61].

2.2 Simulation of turbulent transport in tokamaks

All models are wrong, but some are useful.

– George Box

The discovery of anomalous levels of heat transport in tokamaks has lead to the strong need to identify the main transport mechanisms such that they may be mitigated. The fully kinetic Vlasov equation that accurately describes the behavior of plasma has been known for a long time. However, when applied to tokamaks its direct numerical solution with particle-in-cell codes is prohibitive due to the large number of particles involved (a tokamak reactor contains a few grams of D-T fuel at a time or $N \sim N_A \approx 6 \times 10^{23}$ particles). This provides a key motivation for a reduced numerical and physical model that can capture the majority of the plasma behavior with a large reduction in numerical cost.

2.2.1 Kinetic Theory

In order to provide an exact description of the behavior of collisionless fusion plasmas, in principle the fully kinetic Vlasov equation needs to be solved. It is given by

$$\frac{df_j}{dt} = \frac{\partial f_j}{\partial t} + \boldsymbol{v} \cdot \nabla_{\boldsymbol{x}} f_j + \frac{q_j}{m_j}(\boldsymbol{E} + \boldsymbol{v} \times \boldsymbol{B}) \cdot \nabla_{\boldsymbol{v}} f_j = 0\,, \tag{2.5}$$

where $f_j(\boldsymbol{x}, \boldsymbol{v}, t)$ is the distribution function of the j-th particle species. The electromagnetic fields $\boldsymbol{E}$ and $\boldsymbol{B}$ are calculated from Maxwell's equations,

$$\nabla \cdot \boldsymbol{E} = \frac{4\pi}{c} \sum_j q_j n_j\,, \qquad \nabla \cdot \boldsymbol{B} = 0 \tag{2.6}$$

$$\nabla \times \boldsymbol{E} = -\frac{1}{c}\frac{\partial \boldsymbol{B}}{\partial t}\,, \qquad \nabla \times \boldsymbol{B} = \frac{4\pi}{c} \sum_j \boldsymbol{j}_j + \frac{1}{c}\frac{\partial \boldsymbol{E}}{\partial t}\,, \tag{2.7}$$

where the particle and current densities are calculated by taking the appropriate moments of the distribution function,

$$n_j = \int f_j \, d\boldsymbol{v} \,, \qquad\qquad \boldsymbol{j}_j = q_j \int \boldsymbol{v} f_j \, d\boldsymbol{v} \,. \tag{2.8}$$

Therefore, the electric and magnetic fields are themselves determined by the distribution function and make the corresponding term of the Vlasov equation above a nonlinear function of the distribution function, f_j. The above Vlasov-Maxwell system of equations dictates the time evolution of the distribution function for each particle species in phase space $(\boldsymbol{x}, \boldsymbol{v})$ that is six-dimensional. These equations can only be solved numerically, and to resolve the relevant phase space of a typical tokamak even today's supercomputers are not yet advanced enough to solve the full set of equations without making simplifying approximations. For example, in the strong magnetic field of a tokamak single-particle motion perpendicular to the magnetic field can be divided into relatively fast circular motion and relatively slow drift motion. Averaging over the comparably fast circular motion gives a distribution function of "rings" of charge that is five dimensional in phase space $(\boldsymbol{x}, v_{\|}, \mu)$. Here, $v_{\|}$ represents the velocity along the field lines and μ is the magnetic moment resulting from the gyro-averaged motion of a charge. This is a major example of several gyrokinetic approximations that capture the evolution of the distribution function well, while also making the resulting gyrokinetic equations significantly more computationally tractable than the fully kinetic equations. Solution of the gyrokinetic equations in numerical codes such as GKV [65, 66], GEM [67, 68], GYRO [58] and GENE [69] over the last two decades has contributed significantly to our understanding of micro-turbulence in fusion plasmas.

2.2.2 Basic idea of gyrokinetic theory

The single-particle motion is divided into relatively fast circular motion and relatively slow drift motion. The fast motion arises when charged particles undergo circular motion perpendicular to the magnetic field $\boldsymbol{B} = B_z\hat{z}$ with gyroradius

$$\rho_j = \frac{v_j}{\Omega_j} = \frac{\sqrt{k_B T_j m_j}}{q_j B_z}\,, \tag{2.9}$$

where the angular frequency (or gyrofrequency) is independent of temperature,

$$\Omega_j = \frac{q_j B_z}{m_j}\,. \tag{2.10}$$

Note that the above periodic motion is associated with an adiabatic invariant, the magnetic moment

$$\mu_j = \frac{m_j v_\perp^2}{2B} \propto \frac{T_j}{B}\,. \tag{2.11}$$

A relatively slower motion perpendicular to the field arises due to particle drifts. The mathematical origin of drifts can be found from the equation of motion,

$$m\frac{d\boldsymbol{v}}{dt} = q\boldsymbol{E} + q\boldsymbol{v} \times \boldsymbol{B}\,. \tag{2.12}$$

Replacing $q\boldsymbol{E}$ with a general force component $\boldsymbol{F}$ gives the general equation for drift velocities perpendicular to the magnetic field,

$$\boldsymbol{v} = \frac{\boldsymbol{F} \times \boldsymbol{B}}{qB^2}\,. \tag{2.13}$$

For example, the force can be due to an inhomogeneous magnetic field, $\boldsymbol{F}_{\nabla B} = -\mu\nabla B$, which gives $\boldsymbol{v} = \mu\boldsymbol{B} \times \nabla\boldsymbol{B}/qB^2$ (see Fig. 2.1). In the strong magnetic field of a fusion plasma the drift velocities of charged particles are much smaller than the velocities associated with gyromotion, $v_j = \rho_j\Omega_j$ (for an illustration, see Fig. 2.3). The mathematical and physical details of this and other approximations are highlighted in the following section.

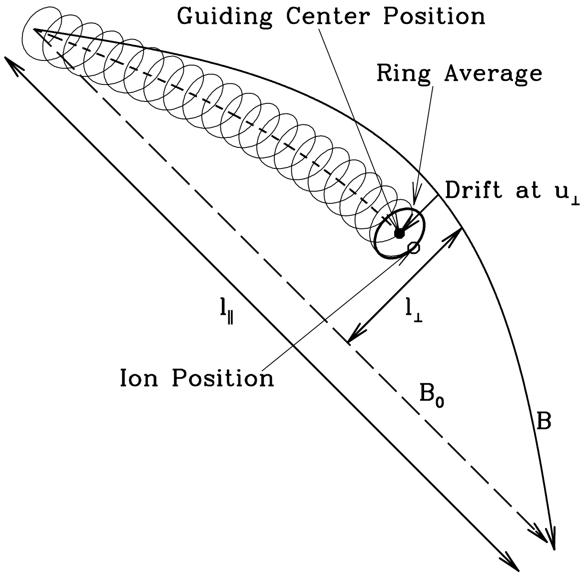

Figure 2.3: Schematic diagram of the gyrokinetic approximation, where fast motion is averaged out such that only the relatively slow drift motion of a "ring" of charge remains (reprinted from [70] by permission of the author and AAS).

2.3 Summary

The main carriers of cross-field transport have been identified as electrostatic and electromagnetic instabilities, which have scale lengths much smaller than the machine size and are therefore commonly called micro-instabilities. The micro-instabilities subject of this work are ion temperature gradient (ITG) and electron temperature gradient (ETG) instabilities, and trapped electron modes (TEMs). In order to study the contribution of these instabilities to the overall heat flux, gyrokinetic codes have been developed. In the following section we highlight the mathematical and numerical approximations that have led to the gyrokinetic theory.

CHAPTER 3

Gyrokinetic Theory

The gyrokinetic approximation reduces the six-dimensional phase space to five dimensions by averaging over a charged particle's gyro-motion perpendicular to the magnetic field, and removes several phenomena on small space-time scales.

3.1 Gyrokinetic Ordering

In the following list, the various approximations employed underneath the umbrella of the gyrokinetic theory are motivated and described:

(i) The averaging over the gyro-motion of charged particles in strong magnetic fields is a major approximation of gyrokinetic theory. This is motivated by the fact that the ion Larmor frequency is much larger than the frequency of microturbulence, $\Omega_i \gg \omega$. Averaging over the gyro-motion gives a five-dimensional distribution function,

$$f(\boldsymbol{X}, v_{\|}, v_{\perp}, t)\,, \tag{3.1}$$

where $\boldsymbol{X}$ is the position of the center of the ring of charge.

(ii) Quantities such as temperature, density, electrostatic potential and magnetic field are assumed to have fluctuations that are small compared to their equilibrium values, which has been corroborated by observations. For example,

$$T(\mathbf{x}, t) = T_0(\mathbf{x}) + T_1(\mathbf{x}, t)\,, \text{ where } T_1 \ll T_0\,, \tag{3.2}$$

and we adopt the notation where the index 1 denotes a first-order perturbation while the index 0 denotes the equilibrium quantity. Note that T_1 varies both in space and time while T_0 forms a time-independent equilibrium quantity.

(iii) As a result of the above approximation, the gyrocenter distribution function of each species can be split into a background Maxwellian distribution function and a small perturbation,

$$f = F_0 + f_1\,, \text{ where } f_1 \ll F_0\,, \tag{3.3}$$

The background Maxwellian for each species is given by

$$F_0 = \left(\frac{m}{2\pi T_0}\right)^{3/2} n_0 \exp\left(-\frac{\frac{1}{2}mv_\parallel^2 + \mu B_0}{T_0}\right)\,, \tag{3.4}$$

This allows us to separate the microturbulence from the macroscopic evolution of the plasma equilibrium, while also benefiting from a reduction in computational intensity.

(iv) In the strong magnetic field of a tokamak, turbulent fluctuations develop elongated structures along the magnetic field and short structures perpendicular to the magnetic field. As a result parallel wavenumbers are much smaller than perpendicular wavenumbers,

$$k_\parallel \ll k_\perp\,. \tag{3.5}$$

Note that perpendicular wavenumbers are on the order of the Larmor radius, $k_\perp \rho_{i,e} \sim 1$.

(v) The gradient scale lengths of the equilibrium quantities are assumed to be much larger than the ion Larmor radius. For example,

$$\frac{1}{L_{T_0}} = \frac{|\nabla T_0|}{T_0} \sim R\,, \tag{3.6}$$

where R is the machine size. Note that the gradient scale lengths of the fluctuating quantities are allowed to be on the order of the Larmor radius. For example,

$$\frac{\nabla T_1}{\nabla T_0} \sim \frac{k_\perp T_1}{T_0/R} \sim k_\perp R \frac{T_1}{T_0} \sim 1\,. \tag{3.7}$$

In summary, these approximations give

$$\frac{\omega}{\Omega_i} \sim \frac{T_1}{T_0} \sim \frac{n_1}{n_0} \sim \frac{q\phi_1}{T_0} \sim \frac{|\mathbf{B}_1|}{|\mathbf{B}_0|} \sim \frac{f_1}{F_0} \sim \frac{k_\parallel}{k_\perp} \sim \frac{\rho_{e,i}}{R} \sim \epsilon \ll 1 \sim k_\perp \rho_{i,e} \,. \tag{3.8}$$

These approximations can now be used to derive the gyrokinetic Vlasov equation. The key steps of the modern derivation of gyrokinetics are described below, following the review article by Brizard & Hahm [71], and summarized in Figure 3.1.

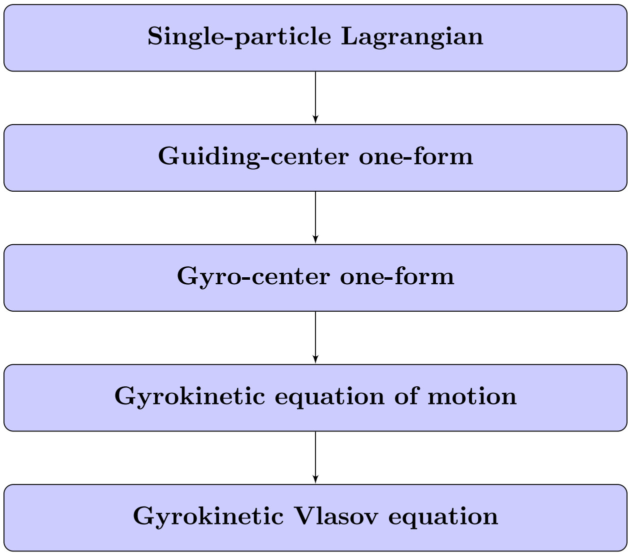

Figure 3.1: Schematic diagram for the main steps of the gyrokinetic derivation.

3.2 Single-particle motion

Starting with the non-relativistic electromagnetic Lagrangian for a single particle, we get

$$\mathcal{L}(\mathbf{x}, \dot{\mathbf{x}}; t) = \frac{1}{2} m \dot{x}^2 + q \dot{\mathbf{x}} \cdot \mathbf{A}(x) - q\phi(x) \,, \tag{3.9}$$

where m is the mass of the particle, q is its charge, $\mathbf{A}(x)$ is the vector potential, $\phi(x)$ the electrostatic potential. This can be written in terms of canonical variables,

$$\mathcal{L}(\mathbf{x}, \dot{\mathbf{x}}; t) = \mathbf{p} \cdot \dot{\mathbf{x}} - H(\mathbf{p}, x) \,, \tag{3.10}$$

where $\mathbf{p} \equiv d\mathcal{L}/d\dot{\mathbf{x}} = m\dot{\mathbf{x}} + q\mathbf{A}(x)$ is the canonical momentum and $H(\mathbf{p}, x) = (\mathbf{p} - q\mathbf{A})^2/2m + q\phi(x)$ is the conserved energy of the particle. The above Lagrangian can be written in terms of a compact one-form, which is defined as follows

$$\gamma \equiv \mathcal{L}\, dt = \mathbf{p} \cdot d\mathbf{x} - H(\mathbf{p}, x)\, dt\,. \tag{3.11}$$

This gives the following variational principle, which is useful to derive the gyrokinetic equations of motion [72],

$$\delta \int \mathcal{L}\, dt = \delta \int \gamma = 0\,. \tag{3.12}$$

As discussed above, the motion of charged particles in strong magnetic fields can be divided into a fast gyration motion around a so-called guiding center and a relatively slow drift of the guiding center. When transforming into guiding-center coordinates and averaging over the fast gyration motion, we obtain the guiding-center Lagrangian as described below. Note that the guiding-center picture does not include electromagnetic fluctuations, which cause the magnetic moment to no longer be a rigorous adiabatic invariant [71]. Capturing electromagnetic fluctuations requires a refined description using so-called gyrocenter coordinates that will also be discussed below.

3.3 Guiding-Center Coordinates

In order to reduce the single-particle Lagrangian of Eq. 3.10 to a guiding-center Lagrangian, we follow the seminal paper by Littlejohn [72]. We start with a coordinate transformation of $(\mathbf{x}, \dot{\mathbf{x}}) \to (\mathbf{x}, \mathbf{v})$, where $m\mathbf{v} = \mathbf{p} - q\mathbf{A}$. This gives

$$\mathcal{L}(\mathbf{x}, \mathbf{v}; t) = (m\mathbf{v} + q\mathbf{A}) \cdot \dot{\mathbf{x}} - \left[\frac{1}{2}mv^2 + q\phi(x)\right]\,, \tag{3.13}$$

We now divide the velocity into two mutually perpendicular components

$$\mathbf{v} = v_{\|}\widehat{\mathbf{b}} + v_{\perp}\widehat{\mathbf{c}}\,, \tag{3.14}$$

where $v_\parallel$ and $v_\perp$ are the average velocities parallel and perpendicular to the averaged background magnetic field direction $\widehat{\mathbf{b}}$, so accordingly $\widehat{\mathbf{c}}$ is an oscillatory unit vector perpendicular to $\widehat{\mathbf{b}}$. Similarly, the position coordinates can be divided into oscillatory and average quantities, namely

$$\mathbf{x} = \mathbf{X} + \boldsymbol{\rho} \tag{3.15}$$

where $\mathbf{X}$ is the average position of the guiding center and $\boldsymbol{\rho} = mv_\perp/qB\,\widehat{\mathbf{a}}$ is an oscillatory position vector of the particle relative to the guiding center. One can refine the definition of the oscillatory component of the position vector with the introduction of a so-called gyrophase angle θ, which is used as follows

$$\begin{aligned} \widehat{\mathbf{a}} &= \cos\theta\,\widehat{\mathbf{e}}_1 - \sin\theta\,\widehat{\mathbf{e}}_2 \\ \widehat{\mathbf{c}} &= -\sin\theta\,\widehat{\mathbf{e}}_1 - \cos\theta\,\widehat{\mathbf{e}}_2\,, \end{aligned} \tag{3.16}$$

where $\widehat{\mathbf{a}} = \widehat{\mathbf{b}} \times \widehat{\mathbf{c}}$ and $\widehat{\mathbf{e}}_1 \times \widehat{\mathbf{e}}_2 = \widehat{\mathbf{b}}$. Averaging over these oscillatory positions and velocities while keeping terms to first order in $\epsilon_B = \rho_{e,i}\nabla \ln B$, we get a guiding-center Lagrangian

$$\mathcal{L}(\mathbf{X}, \dot{\mathbf{X}}; t) = \left[m\dot{X}_\parallel\widehat{\mathbf{b}} + q\mathbf{A}(\mathbf{X})\right] \cdot \dot{\mathbf{X}} + \frac{\mu B(\mathbf{X})}{\Omega(\mathbf{X})}\dot{\theta} - \left[\mu B(\mathbf{X}) + \frac{1}{2}m\dot{X}_\parallel^2 + q\phi(\mathbf{X})\right]\,, \tag{3.17}$$

where we have used the fact that the Lagrangian is independent of θ and therefore $\mu = \frac{1}{2}mv_\perp^2/B$ is an exact adiabatic invariant. This can be re-cast into a guiding-center one-form as follows,

$$\Gamma_0 = q\mathbf{A}_0^*(\mathbf{X}) \cdot d\mathbf{X} + \frac{\mu B(\mathbf{X})}{\Omega(\mathbf{X})}d\theta - H_0(\mathbf{X}, \dot{X}_\parallel, \mu)dt\,, \tag{3.18}$$

where we have adopted '0' indices to distinguish the quantities in the above equations from perturbations that will be added in the next section, and we have made the following substitutions for simplicity,

$$\mathbf{A}_0^*(X) = \frac{m}{q}\dot{X}_\parallel\widehat{\mathbf{b}} + \mathbf{A}_0(\mathbf{X})\,, \tag{3.19}$$

$$H_0(\mathbf{X}, \dot{X}_\parallel, \mu) = \mu B(\mathbf{X}) + \frac{1}{2}m\dot{X}_\parallel^2 + q\phi_0(\mathbf{X})\,. \tag{3.20}$$

While the above 'guiding-center' formalism benefits from the exact invariance of the magnetic moment, it cannot be accurately applied to plasmas where low-frequency electromagnetic perturbations are present with perpendicular wavelengths on the order of $k_\perp \rho_{e,i} \sim 1$ [71,73]. This will be addressed in the following section.

3.4 Gyrocenter Coordinates

> *The best method now available for deriving higher-order terms in the guiding centre expansion is the Lie transform method.*
>
> – Robert G. Littlejohn [72]

Electromagnetic fluctuations associated with micro-turbulence ($k_\perp \rho_{e,i} \sim 1$) lift the exact invariance of the magnetic moment and limit the generality of the guiding-center formalism above [71, 73]. This is due to the fact that electromagnetic perturbations on the order of $k_\perp \rho_{e,i} \sim 1$ are themselves a function of the particle position $\mathbf{x} = \mathbf{X} + \boldsymbol{\rho}(\mathbf{X}, \mu, \theta)$ rather than only the guiding-center position $\mathbf{X}$. Mathematically, these perturbations are expressed as follows

$$\begin{aligned} \phi(\mathbf{x}, t) &= \phi_1(\mathbf{x}, t)\,, \\ \mathbf{A}(\mathbf{x}, t) &= \mathbf{A}_0(\mathbf{X}) + \mathbf{A}_1(\mathbf{x}, t)\,, \end{aligned} \tag{3.21}$$

where the perturbations are small compared to the background quantities,

$$\frac{|\mathbf{E}_{1\perp}|}{v_{th} B_0} \sim \frac{|\mathbf{B}_1|}{B_0} \sim \epsilon \ll 1\,. \tag{3.22}$$

As a result, the guiding-center equations acquire the following gyroradius-scale perturbations

$$\begin{aligned} H &= H_0 + H_1 = H_0 + q\phi_1(\mathbf{x}, t)\,, \\ \Gamma &= \Gamma_0 + \Gamma_1 = \Gamma_0 + q\mathbf{A}_1(\mathbf{x}, t) \cdot d\mathbf{x} - q\phi_1(\mathbf{x}, t) dt\,. \end{aligned} \tag{3.23}$$

We can rewrite the perturbed guiding-center one-form in terms of the total derivative of $\mathbf{x} = \mathbf{X} + \boldsymbol{\rho}(\theta, \mu)$, giving

$$\Gamma_1 = q\mathbf{A}_1(\mathbf{x}, t) \cdot \left(d\mathbf{X} + \frac{\partial \boldsymbol{\rho}}{\partial \theta} d\theta + \frac{\partial \boldsymbol{\rho}}{\partial \mu} d\mu \right) - q\phi_1(\mathbf{x}, t) dt \,. \tag{3.24}$$

To remove the gyro-angle dependence of the above guiding-center equations of motion, we average out the fluctuating contribution over one gyro-orbit. Mathematically, this is carried out using the method of Lie transformations [74]. In this section we will focus mainly on the key steps of a more systematic derivation, which can be found in the literature [71,72,75].

A Lie transformation is a coordinate transformation of the general form [75]

$$\overline{z}^{\alpha} = T z^{\alpha} \,, \tag{3.25}$$

where T is a series of Lie transformations $T = ...T_3 T_2 T_1$, and $z(\mathbf{q}, \mathbf{p}, t)$ is any phase-space coordinate system, where the index α represents the αth coordinate component. We will use T to transform between guiding-center (z) and so-called gyro-center ($\overline{z}$) coordinate systems, where the overbar notation is used to identify the latter. A single Lie transformation T_n is a near-unitary transformation [75],

$$T_n = \exp\left(\epsilon^n L_n\right) \approx 1 + \epsilon^n L_n \,, \tag{3.26}$$

where $\epsilon \ll 1$ is a small ordering parameter and L_n is the operator that carries out the coordinate transformation [75]. The desired transformation from guiding-center to gyro-center one-forms is given by

$$\overline{\Gamma} = T^{-1}\Gamma + dS \,, \tag{3.27}$$

where $\overline{\Gamma}$ is the one-form in gyro-center coordinates with the gyro-angle dependence removed, Γ is the perturbed guiding-center one-form with gyro-angle dependence, and dS is a gauge transformation term that is used to eliminate the remaining gyro-angle dependence from the right hand side of the above equation. Our use of the gauge term relies on the invariance of the Euler-Lagrange equations under gauge transformations of the form $\Gamma \to \Gamma + dS$, where

$S(z^\alpha)$ is any scalar function and dS is its total derivative [75]. We can now transform the perturbed guiding-center one-form, $\Gamma = \Gamma_0 + \Gamma_1 + \Gamma_2$, to the gyro-center coordinate system. First, we look at the Lie transform operator T^{-1}, which is called the *pull-back operator* and can be expanded to second order in ϵ as follows,

$$\begin{aligned} T^{-1} &= \exp(-\epsilon^2 L_2)\exp(-\epsilon L_1) \approx \\ &\approx \left(1-\epsilon^2 L_2\right)\left(1-\epsilon L_1 + \frac{\epsilon^2 L_1^2}{2}\right) = \\ &= 1-\epsilon L_1 + \epsilon^2\left(\frac{L_1^2}{2} - L_2\right) . \end{aligned} \tag{3.28}$$

Ordering terms by their dependence on ϵ^n, we get the gyro-center one-form,

$$\begin{aligned} \overline{\Gamma}_0 &= \Gamma_0 + dS_0 \\ \overline{\Gamma}_1 &= \Gamma_1 - L_1\Gamma_0 + dS_1 \\ \overline{\Gamma}_2 &= \Gamma_2 - L_1\Gamma_1 + \left(\frac{L_1^2}{2} - L_2\right)\Gamma_0 + dS_2 . \end{aligned} \tag{3.29}$$

Applying the operator L_n to a general one-form Γ gives [75]

$$\left(L_n\Gamma\right)_\alpha = G_n^\beta\left(\frac{\partial\Gamma_\alpha}{\partial z^\beta} - \frac{\partial\Gamma_\beta}{\partial z^\alpha}\right) , \tag{3.30}$$

where G_n^β is the generator of the Lie transformation, which will be defined in more detail below. As a result, the αth coordinate component of $\overline{\Gamma}_1$ is

$$\overline{\Gamma}_{1,\alpha} = \Gamma_{1,\alpha} - G_1^\beta\left(\frac{\partial\Gamma_{0,\alpha}}{\partial z^\beta} - \frac{\partial\Gamma_{0,\beta}}{\partial z^\alpha}\right) + \frac{\partial S_1}{\partial z^\alpha} . \tag{3.31}$$

The next key step of the gyrokinetic derivation requires identifying suitable choices of dS and G_n^β to eliminate the gyro-angle dependence on the right hand side of the above gyro-center one-forms. Since Γ_0 is the unperturbed one-form, we have $dS_0 = 0$. To eliminate θ-dependence and μ-dependence of the equations of motion, we want to find dS_1 and G_1^β such that

$$\overline{\Gamma}_{1,\theta} = \overline{\Gamma}_{1,\mu} = \overline{\Gamma}_{1,v_\parallel} = 0 . \tag{3.32}$$

These constraints give the following generator functions [76],

$$
\begin{aligned}
G_1^X &= \frac{1}{B_{0,\parallel}^*}\left[\widehat{\mathbf{b}} \times \left(\mathbf{A}_1 + \frac{\nabla S_1}{q}\right) + \frac{\mathbf{B}_0^*}{m}\frac{\partial S_1}{\partial v_\parallel}\right] \\
G_1^{v_\parallel} &= \frac{\Omega}{B}\frac{\mathbf{B}_0^*}{B_{0,\parallel}^*}\left(\mathbf{A}_1 - \widehat{\mathbf{b}}\langle A_{1,\parallel}\rangle + \frac{\nabla S_1}{q}\right) \\
G_1^\mu &= \frac{\Omega}{B}\left(\frac{m}{B}\mathbf{A}_1 \cdot \mathbf{v}_\perp + \frac{\partial S_1}{\partial \theta}\right) \\
G_1^\theta &= -\frac{\Omega}{B}\left(\frac{1}{v_\perp}\mathbf{A}_1 \cdot \widehat{\mathbf{a}} + \frac{\partial S_1}{\partial \mu}\right) \;,
\end{aligned}
\tag{3.33}
$$

where $\mathbf{B}_0^* = \nabla \times \mathbf{A}_0^*$ and the angled brackets indicate that we have averaged over the fast angular motion

$$
\langle Q \rangle = \frac{1}{2\pi}\oint Q(\mathbf{X} + \boldsymbol{\rho})\, d\theta\,. \tag{3.34}
$$

It remains to define the gauge terms, where we use a result from Ref. [77] that shows the only S_1-dependent term in $\overline{\Gamma}_{1,\alpha}$ that is zeroth order in ϵ depends on $\partial S_1/\partial\theta$. We therefore only need to find a suitable $\partial S_1/\partial\theta$, which is

$$
\frac{\partial S_1}{\partial \theta} = \frac{1}{\Omega}\left[q\widetilde{\phi}_1 + \frac{\widehat{\mathbf{b}} \times \widetilde{\mathbf{A}}_1}{B_{0,\parallel}^*} \cdot \mu \nabla B - q v_\parallel \frac{\mathbf{B}_0^*}{B_{0,\parallel}^*} \cdot \widetilde{\mathbf{A}}_1 - \frac{\Omega}{B}\widetilde{\left(\mathbf{A}_1 \cdot \mathbf{v}_\perp\right)}\right] \;, \tag{3.35}
$$

where we used the tilde symbol to identify fluctuating quantities, which are gyro-angle dependent and defined as

$$
\widetilde{Q} = Q - \langle Q \rangle\,. \tag{3.36}
$$

The above definitions of the generator functions and the gauge function give two non-zero gyro-center components, $\overline{\Gamma}_{1,X}$ and $\overline{\Gamma}_{1,t}$, where the latter is simultaneously the gyro-averaged perturbation to the Hamiltonian $\overline{H}_1$,

$$
\begin{aligned}
\overline{\Gamma}_{1,X} &= q\langle A_{1,\parallel}\rangle \widehat{\mathbf{b}}\,, \\
\overline{\Gamma}_{1,t} &= q\langle \phi_1 \rangle - q\langle \mathbf{A}_1 \cdot \mathbf{v}_\perp \rangle \equiv \overline{H}_1\,.
\end{aligned}
\tag{3.37}
$$

In principle, we have now found a gyrocenter description of the one-form. Before writing it down, however, we can simplify the above expression for $\overline{H}_1$ to a more practical form. We pay particular attention to the averaging procedure $\langle \phi_1 \rangle = \langle \phi_1(\mathbf{X} + \boldsymbol{\rho}) \rangle$ with the goal of simplifying this expression.

We first aim to split the perturbation into a guiding-center-dependent and a gyro-angle-dependent term, which can be done in Fourier space [77]

$$\begin{aligned}
\langle \phi_1(\mathbf{X} + \boldsymbol{\rho}) \rangle &= \frac{1}{2\pi} \int_0^{2\pi} \phi_1(\mathbf{X} + \boldsymbol{\rho}) \, d\theta = \\
&= \frac{1}{(2\pi)^4} \int_0^{2\pi} d\theta \int_{-\infty}^{\infty} \widehat{\phi_1}(\mathbf{k}) e^{i\mathbf{k}\cdot(\mathbf{X}+\boldsymbol{\rho})} \, d^3k = \\
&= \frac{1}{(2\pi)^3} \int_{-\infty}^{\infty} \widehat{\phi_1}(\mathbf{k}) e^{i\mathbf{k}\cdot\mathbf{X}} \, d^3k \cdot \frac{1}{2\pi} \int_0^{2\pi} e^{i\mathbf{k}\cdot\boldsymbol{\rho}} \, d\theta \, .
\end{aligned} \tag{3.38}$$

We now compute the gyro-average of the second integral as

$$\begin{aligned}
\langle e^{i\mathbf{k}\cdot\boldsymbol{\rho}} \rangle &= \frac{1}{2\pi} \int_0^{2\pi} e^{i\mathbf{k}\cdot\boldsymbol{\rho}} \, d\theta = \frac{1}{2\pi} \int_0^{2\pi} e^{ik_\perp \rho \cos\theta} \, d\theta = \\
&= \frac{1}{2\pi} \int_0^{\pi} e^{ik_\perp \rho \cos\theta} \, d\theta + \frac{1}{2\pi} \int_\pi^{2\pi} e^{ik_\perp \rho \cos\theta} \, d\theta = \\
&= \frac{1}{2} J_0\left(k_\perp \rho\right) + \frac{1}{2\pi} \int_0^{\pi} e^{-ik_\perp \rho \cos\theta'} \, d\theta' = \\
&= \frac{1}{2} J_0\left(k_\perp \rho\right) + \frac{1}{2} J_0\left(-k_\perp \rho\right) = \\
&= J_0\left(k_\perp \rho\right) \, ,
\end{aligned} \tag{3.39}$$

where we have used the change of variables $\theta' \to \theta - \pi$ and the parity of $J_0\left(k_\perp \rho\right) = J_0\left(-k_\perp \rho\right)$, where $J_0\left(k_\perp \rho\right)$ is the Bessel function of the first kind of 0th order and given by [78]

$$J_0\left(k_\perp \rho\right) = \frac{1}{\pi} \int_0^{\pi} e^{ik_\perp \rho \cos\theta} \, d\theta = \sum_{n=0}^{\infty} \frac{(-1/4)^n}{(n!)^2} \left(k_\perp \rho\right)^{2n} \, . \tag{3.40}$$

We now employ the above results in the equation for $\langle\phi_1(\mathbf{X}+\boldsymbol{\rho})\rangle$,

$$\begin{aligned}
\langle\phi_1(\mathbf{X}+\boldsymbol{\rho})\rangle &= \frac{1}{(2\pi)^3}\int_{-\infty}^{\infty} J_0\left(k_\perp\rho\right)\widehat{\phi}_1(\mathbf{k})e^{i\mathbf{k}\cdot\mathbf{X}}\,d^3k = \\
&= \frac{1}{(2\pi)^3}\int_{-\infty}^{\infty}\sum_{n=0}^{\infty}\frac{(-1/4)^n}{(n!)^2}\left(k_\perp\rho\right)^{2n}\widehat{\phi}_1(\mathbf{k})e^{i\mathbf{k}\cdot\mathbf{X}}\,d^3k = \\
&= \frac{1}{(2\pi)^3}\int_{-\infty}^{\infty}\sum_{n=0}^{\infty}\frac{(-1/4)^n}{(n!)^2}\left(-i\rho\nabla_\perp\right)^{2n}\widehat{\phi}_1(\mathbf{k})e^{i\mathbf{k}\cdot\mathbf{X}}\,d^3k = \\
&= \frac{1}{(2\pi)^3}\sum_{n=0}^{\infty}\frac{(-1/4)^n}{(n!)^2}\left(-i\rho\nabla_\perp\right)^{2n}\int_{-\infty}^{\infty}\widehat{\phi}_1(\mathbf{k})e^{i\mathbf{k}\cdot\mathbf{X}}\,d^3k = \\
&= J_0(-i\rho\nabla_\perp)\phi_1(\mathbf{X}) = J_0(\lambda)\phi_1(\mathbf{X})\,,
\end{aligned} \tag{3.41}$$

where $\lambda^2 = -\rho^2\nabla_\perp^2$. We have thus analytically computed the gyro-average for the perturbed electrostatic potential ϕ_1. Similarly, we get for $\langle\mathbf{A}_1\cdot\mathbf{v}_\perp\rangle$ [77]

$$\langle\mathbf{A}_1\cdot\mathbf{v}_\perp\rangle = -\frac{2\mu}{q\lambda}J_1(\lambda)B_{1,\parallel} = -\frac{\mu}{q}\langle B_{1,\parallel}\rangle\,, \tag{3.42}$$

where $J_1(\lambda)$ is the Bessel function of the first kind of 1st order,

$$J_1(\lambda) = \sum_{n=0}^{\infty}\frac{(-1)^n}{n!(n+1)!}\left(\frac{\lambda}{2}\right)^{2n+1}\,. \tag{3.43}$$

Therefore, the gyro-averaged Hamiltonian $\overline{H}_1$ can be analytically solved and simplified to

$$\overline{H}_1 = q\langle\phi_1\rangle + \mu\langle B_{1,\parallel}\rangle \equiv q\langle\psi_1\rangle\,, \tag{3.44}$$

where we have introduced an effective potential $\langle\psi_1\rangle$ [76].

In summary, the gyro-center one-form is found to be

$$\overline{\Gamma} = q\left(\mathbf{A}_0^* + \langle A_{1,\parallel}\rangle\widehat{\mathbf{b}}\right)\cdot d\mathbf{X} + \frac{\mu B}{\Omega}d\theta - \left(H_0 + q\langle\psi_1\rangle\right)\,dt\,. \tag{3.45}$$

The above gyrokinetic one-form can now be used to find the equation of motion for $\dot{\mathbf{X}}$ and $\dot{v}_\parallel$, which in turn is needed to solve the gyrokinetic Vlasov equation.

3.5 Gyrokinetic Vlasov Equation

The gyrokinetic Vlasov equation for the distribution function of gyro centers $f_j(\dot{\mathbf{X}}, v_\parallel, \mu)$ becomes

$$\frac{df_j}{dt} = \frac{\partial f_j}{\partial t} + \dot{\mathbf{X}} \cdot \nabla f_j + \dot{v}_\parallel \frac{\partial f_j}{\partial v_\parallel} = 0\,, \tag{3.46}$$

where $\dot{\mathbf{X}}$ and $\dot{v}_\parallel$ are defined below.

$$\dot{\mathbf{X}} = \dot{X}_\parallel \widehat{\mathbf{b}} + \frac{B}{B_\parallel^*}\left(v_{\nabla B} + v_\chi + v_c\right)\,, \tag{3.47}$$

where we have a ∇B_0-drift

$$v_{\nabla B} = \frac{\mu}{m\Omega}\widehat{\mathbf{b}} \times \nabla B_0\,, \tag{3.48}$$

and an effective $\boldsymbol{E} \times \boldsymbol{B}$-drift,

$$v_\chi = -\frac{1}{B_0^2}\nabla \chi_1 \times \mathbf{B}_0\,, \tag{3.49}$$

where we have used the effective potential

$$\chi_{1j} = \langle \psi_1 \rangle - v_\parallel \langle A_{1\parallel} \rangle\,. \tag{3.50}$$

Moreover, we identify an effective curvature drift as

$$v_c = \frac{v_\parallel^2}{\Omega}\left(\nabla \times \widehat{\mathbf{b}}\right)_\perp\,. \tag{3.51}$$

Similarly, using the Euler-Lagrange equations we find

$$\dot{v}_\parallel = -\frac{\mathbf{B}^*}{mB_\parallel^*} \cdot \left(\mu \nabla B + q\nabla \overline{\psi}_1\right) - \frac{q}{m}\dot{A}_{1\parallel}\,. \tag{3.52}$$

Therefore, we are now in principle able to solve the gyrokinetic Vlasov equation.

In practice, further simplification can be obtained by splitting the gyrocenter distribution function into a background Maxwellian and first-order perturbations,

$$f_j = F_{0j} + f_{1j}\,, \text{ where } f_{1j} \ll F_{0j}\,, \tag{3.53}$$

gives the gyrokinetic distribution function

$$g_{1j} \equiv f_{1j} + v_\parallel \frac{q_j}{T_{0j}} F_{0j} \langle A_{1\parallel} \rangle\,, \tag{3.54}$$

and the non-adiabatic part of the distribution function

$$h_{1j} \equiv f_{1j} + \frac{q_j}{T_{0j}} F_{0j} \langle \phi_1 \rangle = g_{1j} + \frac{q_j}{T_{0j}} F_{0j} \chi_{1j}\,. \tag{3.55}$$

3.5.1 Gyrokinetic field equations

The fluctuation potentials $(\phi_1, \mathbf{A}_{1\parallel})$ must be reformulated in terms of the gyrocenter distribution function. Starting with Maxwell's equation for the *fluctuating* field components, while neglecting the displacement current for simplicity, gives

$$\nabla \cdot \mathbf{E}_1 = \frac{4\pi}{c} \sum_j q_j n_j\,, \qquad \nabla \cdot \mathbf{B}_1 = 0 \tag{3.56}$$

$$\nabla \times \mathbf{E}_1 = -\frac{1}{c}\frac{\partial \mathbf{B}_1}{\partial t}\,, \qquad \nabla \times \mathbf{B}_1 = \frac{4\pi}{c} \sum_j \mathbf{j}_j\,. \tag{3.57}$$

The fields themselves can be expressed in term of the electrostatic and scalar magnetic potentials,

$$\mathbf{E}_1 = -\nabla\phi_1 - \frac{1}{c}\frac{\partial \mathbf{A}_{1\parallel}}{\partial t}\,, \qquad \mathbf{B}_1 = \nabla \times \mathbf{A}_{1\parallel}\,. \tag{3.58}$$

This allows us to define Poisson's equation and the parallel Ampère's law,

$$\nabla^2\phi_1 \approx \nabla^2\phi_{1\perp} = -\frac{4\pi}{c} \sum_j q_j n_j\,, \qquad \nabla^2 \mathbf{A}_{1\parallel} \approx \nabla_\perp^2 A_{1\parallel} = -\frac{4\pi}{c} \sum_j j_{j\parallel}\,. \tag{3.59}$$

3.5.2 Gyrokinetic equation solved in GENE

The gyrokinetic equation solved in GENE is given by (see Ref. 79)

$$\frac{\partial g_{kj}}{\partial t} = L\left[g_{kj}\right] + D\left[g_{kj}\right] + N\left[g_{kj}, g_{kj}\right] \,, \tag{3.60}$$

where L represents a linear term, D a dissipation term and N a nonlinear term, and g_{kj} is given by

$$g_{kj} = f_{kj} + v_{Tj} v_{\|} \frac{q_j F_{0j}}{T_{0j}} J_{0kj} A_{1\|k} \,. \tag{3.61}$$

The linear term $L\left[g_{kj}\right]$ can itself be written in terms of three components,

$$L\left[g_{kj}\right] = L_G\left[g_{kj}\right] + L_K\left[g_{kj}\right] + L_{\|}\left[g_{kj}\right] \,, \tag{3.62}$$

where L_G captures the effect due to temperature and density gradients, L_K the effect due to magnetic curvature, and $L_{\|}$ the parallel effects due to magnetic trapping and linear Landau damping. Specifically, the first linear term is

$$L_G\left[g_{kj}\right] = -\left[\omega_{nj} + \left(v_{\|}^2 + \mu B_0 - 2/3\right)\omega_{T_j}\right] F_{0j}\, ik_y \chi_{kj} \,, \tag{3.63}$$

where $\omega_n = \nabla \ln n$ is the logarithmic density gradient, $\omega_T = \nabla \ln T$ is the logarithmic temperature gradient, and χ_{kj} is given by

$$\chi_{kj} = J_{0kj}\phi_{1k} - v_{T_j} v_{\|} J_{0kj} A_{1\|k} \,. \tag{3.64}$$

Moreover, the second linear term is

$$L_K\left[g_{kj}\right] = -\frac{T_{0j}\left(2v_{\|}^2 + \mu B_0\right)}{q_j B_0}\left(K_x\, ik_x + K_y\, ik_y\right) h_{kj} \,, \tag{3.65}$$

where K_x and K_y are geometric factors that depend on the metric coefficients defined in Sec. 4.5.2,

$$\begin{aligned} K_x &= -\frac{L_{\text{ref}}}{B_{\text{ref}}} \frac{g^{xx}g^{yz} - g^{yx}g^{xz}}{B_0^2} \frac{\partial B_0}{\partial z} \,, \\ K_y &= \frac{L_{\text{ref}}}{B_{\text{ref}}} \frac{g^{xy}g^{yz} - g^{yy}g^{xz}}{B_0^2} \frac{\partial B_0}{\partial z} \,. \end{aligned} \tag{3.66}$$

The last of the three linear terms, $L_\parallel$, is given by

$$L_\parallel \left[g_{kj} \right] = \frac{v_{T_j}}{2B_0 J(z)} \left\{ \frac{h_{kj}}{F_{0j}}, g \right\}_{z,v_\parallel} \,, \tag{3.67}$$

where the Poisson bracket represents the operation

$$\{f, g\}_{q,p} = \frac{\partial f}{\partial q}\frac{\partial g}{\partial p} - \frac{\partial f}{\partial p}\frac{\partial g}{\partial q} \,. \tag{3.68}$$

The dissipation term contains the hyper diffusion operators, which are particularly useful when there are no collisions,

$$D\left[g_{kj} \right] = \left(a_x \partial_x^n + a_y \partial_y^n + a_z \partial_z^n + a_{v_\parallel} \partial_{v_\parallel}^n \right) h_{kj} \,, \tag{3.69}$$

where typically $n = 4$ and the coefficients $a_{x,y,z,v_\parallel}$ can be adapted to the physical problem at hand. The nonlinear term captures the $\boldsymbol{E} \times \boldsymbol{B}$ drift velocity,

$$\begin{aligned} N\left[g_{kj}, g_{kj} \right] &= \sum_{k'} \sum_{k''} \left(k_y'' k_x' - k_x'' k_y' \right) \chi_{k'j} h_{k''j} \delta_{k-k'-k''} \\ &= \sum_{k'} \left(k_y k_x' - k_x k_y' \right) \chi_{k'j} h_{(k-k')j} \\ &= \sum_{k'} \left(k_y k_x' - k_x k_y' \right) \chi_{k'j} g_{(k-k')j} \,. \end{aligned} \tag{3.70}$$

3.6 Summary

The main steps necessary to follow the derivation of gyrokinetic theory have been described. In brief, the guiding-center formalism breaks down in the presence of low-frequency electromagnetic fluctuations on the order of the gyroradii. Specifically, the magnetic moment μ acquires a fluctuating component with gyro-angle dependence and therefore loses its exact invariance. With a second coordinate transformation from guiding-center coordinates to gyro-center coordinates, a new magnetic moment $\bar{\mu}$ can be constructed that is invariant [71]. This coordinate transformation generates an appropriate gyrokinetic one-form that can be used to find the equations of motion necessary to solve the gyrokinetic Vlasov equation.

CHAPTER 4

The GENE Code

The GENE code has been developed by Professor Frank Jenko and his team since the 2000s [29,30]. Over time it has acquired many features that allow it to model fusion plasmas with an increasing degree of realism. For example, it can model the plasma in both local and global geometries [80]. In this section we only highlight the main features of the code that have been instrumental in the success of the present work. Of particular note are the local flux-tube approximation (allowing numerically efficient spectral methods to be employed), the realistic implementation of $\boldsymbol{E} \times \boldsymbol{B}$ shear implemented by Daniel Told [76], the so-called GyroLES techniques implemented by Alejandro Bañón Navarro [79], and the Sugama collision operator recently implemented by Paul Crandall into GENE.

4.1 Boundary Conditions in GENE

The spatial coordinates in GENE are defined as

$$\begin{aligned} x &= \rho \\ y &= (q\theta - \zeta)\, C_y \\ z &= \theta\,, \end{aligned} \tag{4.1}$$

where $\rho = (\Phi/\Phi_{\text{edge}})^{1/2}$ is the toroidal flux radius and Φ_{edge} is the toroidal flux at the separatrix, so that ρ is often considered as a flux surface label. Moreover, θ is the straight field line angle, ζ is the toroidal angle and $q(\rho)$ is the safety factor, which is a function of the flux surface. The coefficient C_y is a constant, defined as

$$C_y = \frac{\rho_0}{q_0}\,, \tag{4.2}$$

where $q_0 = q(\rho_0)$ and $\rho_0 = x_0$, which is the reference position in GENE and is typically in the center of the radial extent of the box.

4.1.1 Boundary Conditions in the binormal direction

A tokamak is periodic in the toroidal (ζ) and poloidal (θ) directions. The toroidal periodicity requirement translates into a boundary condition for the binormal direction (y) in GENE. Starting with the toroidal periodicity,

$$f(\rho, \zeta, \theta) = f(\rho, \zeta + 2\pi, \theta)\,, \tag{4.3}$$

we get the equivalent requirement in GENE coordinates,

$$f(x, y, z) = f(x, y - C_y 2\pi, z)\,. \tag{4.4}$$

Therefore, in order to cover one full toroidal turn, a simulation domain must have a binormal extent of $L_y = 2\pi C_y$. Physically, the turbulent correlation lengths are much smaller than one full toroidal turn, such that in practice a binormal simulation domain that is an integer fraction of a full toroidal length can be considered,

$$L_y = \frac{2\pi C_y}{n_0} = \frac{2\pi x_0}{n_0 q_0}\,, \tag{4.5}$$

where n_0 is the lowest resolved toroidal mode number. At the same time, approximate periodicity can be assumed,

$$f(x, y, z) = f(x, y - L_y, z)\,. \tag{4.6}$$

As a consequence of this approximate periodicity, GENE models the toroidal direction in Fourier space with the following mode numbers

$$k_y = jk_{y,\mathrm{min}} = j\frac{2\pi}{L_y} = \frac{jn_0}{C_y}\,, \tag{4.7}$$

where $k_{y,\mathrm{min}} = 2\pi/L_y$ is the lowest resolved wavenumber and for $n_0 = 1$ corresponds to the lowest wavenumber of the system.

4.1.2 Boundary Conditions in the parallel direction

Poloidal periodicity in a tokamak demands that

$$f(\rho, \zeta, \theta) = f(\rho, \zeta, \theta + 2\pi)\,, \tag{4.8}$$

which, in GENE coordinates, corresponds to

$$f(x, y, z) = f(x, y + 2\pi q C_y, z + 2\pi)\,. \tag{4.9}$$

In pseudo-spectral notation, this gives

$$f(x, y, z) = \sum_{k_y} f(x, k_y, z)e^{ik_y y} = \sum_{k_y} f(x, k_y, z + 2\pi)e^{ik_y(y+2\pi q C_y)}\,. \tag{4.10}$$

Using $k_y C_y = jn_0$ from the previous section, it follows that

$$f(x, k_y, z) = f(x, k_y, z + 2\pi)e^{i2\pi j n_0 q(x)}\,. \tag{4.11}$$

This will form the boundary condition for global simulations, where periodic radial boundary conditions are not enforced. However, in the local simulations, the artificial radial periodicity further constrains the boundary conditions. To capture the radial dependence of $q(x)$ we do a Taylor expansion,

$$q(x) \approx q_0 + (x - x_0)\frac{\partial q}{\partial x} = q_0 \left(1 + \frac{x - x_0}{x_0}\hat{s}\right) , \tag{4.12}$$

where

$$\hat{s} = \frac{x_0}{q_0}\frac{\partial q}{\partial x} . \tag{4.13}$$

We get

$$\begin{aligned} f(x, y, z) &= \sum_{k_x, k_y} f(k_x, k_y, z) e^{ik_x x} e^{ik_y y} \\ &= \sum_{k_x, j} f(k_x, k_y, z + 2\pi) e^{ik_x x} e^{ik_y y} e^{i2\pi j n_0 q(x)} \end{aligned} \tag{4.14}$$

Looking only at the exponents with radial dependence in the last line above, we get

$$\begin{aligned} k_x x + 2\pi j n_0 q(x) &= k_x x + 2\pi j n_0 q_0 + 2\pi j n_0 \frac{q_0}{x_0}\left(x - x_0\right)\hat{s} \\ &= \left(k_x + 2\pi\hat{s}\frac{j n_0}{C_y}\right) x + 2\pi j n_0 q_0 (1 - \hat{s}) \\ &= \left(k_x + 2\pi\hat{s}k_y\right) x + 2\pi j n_0 q_0 (1 - \hat{s}) \end{aligned} \tag{4.15}$$

where we have used the relations $C_y = \frac{x_0}{q_0}$ and $k_y = \frac{j n_0}{C_y}$. This gives the boundary conditions to be enforced in the local simulations,

$$f(k_x, k_y, z) = f(k_x, k_y, z + 2\pi) e^{i(k_x + 2\pi\hat{s}k_y)x} e^{i2\pi j n_0 q_0 (1 - \hat{s})} . \tag{4.16}$$

In order resolve the modes with effective wavenumber $k_{\text{eff}} = k_x + 2\pi\hat{s}k_y$ that arise naturally due to the parallel boundary conditions, the following condition has to be satisfied

$$k_{\text{eff,min}} = k_{x,\text{min}} + 2\pi\hat{s}k_{y,\text{min}} = k_{x,\text{min}} \left(1 + \frac{2\pi\hat{s}k_{y,\text{min}}}{k_{x,\text{min}}}\right) = k_{x,\text{min}} \left(1 + \mathcal{N}\right) , \tag{4.17}$$

where k_{eff} is an effective wavenumber present in the system and $\mathcal{N} \in \mathbb{Z}^+$. This gives the following constraint on the minimum radial mode number,

$$k_{x,\text{min}} = \frac{2\pi \hat{s} k_{y,\text{min}}}{\mathcal{N}} \,, \tag{4.18}$$

which translates to

$$\mathcal{N} = \frac{2\pi \hat{s} L_x}{L_y} \,. \tag{4.19}$$

4.2 Observables in GENE

The GENE code has the capabilities to analyze a variety of observables, such as density and temperature fluctuation amplitudes and turbulence cross-phases. This work focuses mainly on the radial heat transport, so it is instructive to review the method with which this observable is obtained [81]. It is derived as a moment of the perturbed part of the particle coordinate distribution function, $f_1^{(\text{pc})}$,

$$Q_j = \left\langle \int d^3v \, \frac{1}{2} m_j v^2 f_1^{(\text{pc})} \mathbf{v}_D \cdot \nabla x \right\rangle \cdot V' \,, \tag{4.20}$$

where m_j is the mass of the j-th particle species, $\mathbf{v}_D$ is the drift velocity, $\langle ... \rangle$ is an average over the flux-surface. Moreover, $V' = \partial V / \partial x$ is the radial gradient of the volume enclosed by the flux-tube. The particle coordinate distribution function, $f_1^{(\text{pc})}$, is derived from the gyro-center distribution function, $f_1^{(\text{gc})}$, with

$$f_1^{(\text{pc})} = f_1^{(\text{gc})} + F_{0j} \left[\frac{q_j \left(\bar{\phi}_1 - \phi_1 \right) + \mu \bar{B}_{1\parallel}}{T_{0j}} \right] , \tag{4.21}$$

where F_{0j} is the equilibrium Maxwellian with temperature T_{0j} and the overbar signifies a gyro-averaged quantity as before. Note that the above transformation from gyro-center distribution to particle-center distribution function includes an intermediate step from gyro-center to guiding-center and from guiding-center to particle-center distribution functions. The steps of this coordinate transformation are qualitatively similar to the steps taken in the derivation of gyrokinetics in Chapter 3. For example, this transformation involves the *push-forward operator*,

$$T_n = \exp\left(\epsilon^n L_n\right) \approx 1 + \epsilon^n L_n\,, \tag{4.22}$$

rather than its inverse, the pull-back operator, of Eq. 3.28. Therefore, we do not elaborate upon the detailed steps of this transformation here (for details, see [79, 82]). The drift velocity $\mathbf{v}_D$ represents the generalized $\boldsymbol{E} \times \boldsymbol{B}$ drift velocity that arises due to the fluctuating perturbations in the potentials,

$$\mathbf{v}_D \approx \frac{c}{B_0^2}\boldsymbol{B}_0 \times \nabla\left[\phi_1 - \mathbf{v}\cdot\mathbf{A}_1/c\right]\,, \tag{4.23}$$

where ϕ_1 is the electrostatic and $\mathbf{A}_1$ is the vector potential [81]. This summarizes the computation of the radial heat transfer in the GENE code.

4.3 Treatment of Electric Field Shear

The flow shear, which is defined as the radial gradient $\gamma_E \equiv \partial v_{E\times B}/\partial r$, can have an important effect on turbulent heat transport. Typically, it becomes relevant when the shearing rate is similar or larger than the maximum linear growth rate, $\gamma_E \gtrsim \gamma_{\text{lin}}$ [83]. The radially varying flow can shear turbulent eddies in the poloidal direction, which increases their poloidal correlation length and reduces their radial correlation length [84, 85]. This can lead to experimentally relevant improvements in particle and energy confinement. The $v_{E\times B}$ velocity is a function of both the radial electric field and the magnetic field. The radial electric field is given by the radial force balance equation,

$$E_r = \frac{\nabla p_i}{Z n_e} + v_\theta B_\zeta - v_\zeta B_\theta\,, \tag{4.24}$$

where p_i is the ion pressure and v_θ the poloidal velocity and v_ζ the toroidal velocity of the ions. Close to the edge, the dominant terms in the above equation are those involving the pressure gradient and the poloidal velocity. Further from the LCFS the term involving the toroidal velocity, which is driven by the co-injected neutral beam, dominates.

In GENE, there exist two ways to implement a flow shear that each have their strengths and weaknesses. In the first method, one can introduce an external electrostatic potential to the $\boldsymbol{E}\times\boldsymbol{B}$-drift term, which was implemented by Tobias Görler. While the external potential can take an arbitrary form in global simulations, periodic boundary conditions in the flux-tube approximation mandate an external potential that is also periodic, $\phi(x) = \phi_0 \sin(k_x x)$. This implementation has the advantage of minimal additional computational complexity, but has the disadvantage that it is not radially uniform in the flux-tube model. In practice, it is often used to study tertiary instabilities.

In the second method, a radially constant shear flow that varies poloidally throughout the flux-tube was implemented by Daniel Told using a method developed by Hammett *et al.* [86]. In the Hammett $E \times B$ model[*], a transformation into the co-moving coordinate system of the equilibrium flow and a discrete time evolution of the sheared radial wavenumber greatly reduce computational intensity while maintaining acceptable numerical accuracy [86]. This method is described in the following first in a slab picture for illustration and then for the local flux-tube simulations.

The goal of Hammett's model is to maintain the periodicity of the simulation domain such that numerically efficient spectral methods can be employed while accounting for the effects of $\boldsymbol{E} \times \boldsymbol{B}$ shear. Translation into the frame moving with the flow shear gives

$$\begin{aligned} x' &= x \\ y' &= y - x\gamma_E t \\ t' &= t\,. \end{aligned} \tag{4.25}$$

In pseudo-spectral notation, the distribution function in the moving frame has the form

$$f(x', y', t') = \sum_k f_k(t') e^{i[k_x x' + k_y y']} \tag{4.26}$$

---

[*] https://w3.pppl.gov/ hammett/refs/2006/APS06-Hammett-ExB.pdf, date accessed: Aug 2$^{\mathrm{nd}}$, 2018

where we have ignored three dimensions $(z, v_\parallel, \mu)$ for simplicity. Transforming back to the stationary laboratory coordinates gives

$$\begin{aligned} f(x,y,t) &= \sum_k f_k(t) e^{i[k_x x + k_y(y - x\gamma_E t)]} \\ &= \sum_k f_k(t) e^{i[(k_x - k_y\gamma_E t)x + k_y y)} \\ &= \sum_k f_k(t) e^{i[k_x^*(t)x + k_y y]} \end{aligned} \tag{4.27}$$

Therefore, this transformation introduces an effective time-dependence to the radial wave number

$$k_x^*(t) = k_x - k_y \gamma_E t \,. \tag{4.28}$$

To avoid a costly re-initialization of many parts of the code with each time-step, the distribution function and electromagnetic fields are shifted at time intervals Δt whenever $k_x^*(t)$ differs from k_x by more than $\Delta k_x/2$, where $\Delta k_x = 2\pi/L_x$ is the grid spacing and L_x is the radial box size,

$$f(k_x^*, k_y) \rightarrow f(k_x - \Delta k_x, k_y) \,. \tag{4.29}$$

This discrete evolution in time is effectively 2$^{\text{nd}}$ order accurate and converges well [86]. These shifts occur at a frequency of $1/\Delta t = 2k_y\gamma_E/\Delta k_x$, such that modes with large wave numbers experience more shifts per unit time. Moreover, note that the finite size of the simulation box requires a definition of the boundary conditions for the flow shear. In GENE, these are defined such that components of the distribution function that leave the domain are discarded and those entering the domain are initially set to zero. Therefore, this method introduces some artificial dissipation into the simulation. Convergence studies can be used to reduce numerical artifacts associated with discrete time-stepping. Specifically, $\Delta k_x = 2\pi/L_x$ can be reduced by increasing the box size. Note that an increase in radial box size should be accompanied by a proportional increase in the number of radial grid points to maintain a similar level of radial resolution. Throughout this work, the Hammett $\boldsymbol{E} \times \boldsymbol{B}$ shear model is well-suited for the near-edge region.

The Hammett $\boldsymbol{E} \times \boldsymbol{B}$ model does not work well with very large shearing rates or in environments where prohibitively large radial box resolution and size are required such as in the edge region ($\rho > 0.95$). Here, steep gradients and large magnetic shear co-exist with large flow shear. Therefore, Tobias' $\boldsymbol{E} \times \boldsymbol{B}$ implementation is better suited for the edge region as part of a global simulation in future work. Note that the rigorous implementation of a general background field would require a different derivation of the gyrokinetic equations, i.e. a modified background distribution function F_0, which may become subject of a future GENE feature.

4.4 Description of GyroLES Techniques

> *Big whirls have little whirls that feed on their velocity,*
> *and little whirls have lesser whirls and so on to viscosity.*
> – Lewis F. Richardson

In order to significantly reduce the computational cost of gyrokinetic simulations while maintaining an acceptable level of accuracy, so-called GyroLES techniques have been implemented into GENE by Alejandro Bañón Navarro [79]. To properly motivate these techniques, which were instrumental for the success of multi-scale simulations presented in this work, we start by describing turbulence in neutral fluids following Ref. 79. Neutral fluids form a useful starting point for two reasons: (i) Physically, neutral fluids provide a simple picture of the general properties of plasma turbulence (with some limitations as described below), and (ii) historically, the study of neutral fluids has first given rise to so-called "Large Eddy Simulation (LES)" techniques that were later adapted to gyrokinetics to form "GyroLES" techniques.

In order to highlight the general properties of neutral fluid turbulence, recall that the Navier-Stokes equation is given by

$$\rho\left(\frac{\partial \mathbf{v}}{\partial t} + \mathbf{v} \cdot \nabla \mathbf{v}\right) = -\nabla p + \nu \rho \nabla^2 \mathbf{v} + \mathbf{f}(\mathbf{x}, t)\,, \tag{4.30}$$

where $\mathbf{v}(\mathbf{x}, t)$ is the velocity of a fluid element at position $\mathbf{x}$ and time t. Moreover, ρ is the mass density, p is the fluid pressure, ν is the kinematic viscosity, and $\mathbf{f}(\mathbf{x}, t)$ represents the external forcing. Note that the Reynold's number is defined as the ratio between inertial force term ($\mathbf{v} \cdot \nabla \mathbf{v}$) and the viscous force term ($\nu \nabla^2 \mathbf{v}$),

$$Re \equiv \frac{\mathbf{F}_i}{\mathbf{F}_\nu} = \frac{\mathbf{v} \cdot \nabla \mathbf{v}}{\nu \nabla^2 \mathbf{v}} \,. \tag{4.31}$$

Systems with a low Reynold's number are dominated by viscous forces and show laminar flow, while systems with high Reynold's numbers show turbulent flow via eddies at many different length scales. By taking the dot product of the Navier-Stokes equation with $\mathbf{v}$ while assuming that the fluid is incompressible ($\nabla \cdot \mathbf{v} = 0$), we get the energy conservation equation

$$\frac{dE_v}{dt} \equiv \frac{d}{dt} \int \frac{1}{2} \rho v^2 \, d\mathbf{x} = \int \mathbf{v} \cdot \mathbf{f} \, d\mathbf{x} - \nu \int \rho \left(\nabla \times \mathbf{v}\right)^2 \, d\mathbf{x} \,, \tag{4.32}$$

where any change of kinetic energy on the left hand side is caused by a difference in energy input due to external forcing (usually at large scales) and viscous heat dissipation (typically at small scales). In a turbulent steady state, the total energy in the system is constant in time, so the forcing and viscous dissipation terms are equal,

$$\frac{dE_v}{dt} = 0 \rightarrow \int \mathbf{v} \cdot \mathbf{f} \, d\mathbf{x} = \nu \int \rho \left(\nabla \times \mathbf{v}\right)^2 \, d\mathbf{x} \, = m\epsilon, \tag{4.33}$$

where ϵ is the energy flux per unit mass and m is the mass of a fluid element. As mentioned above, the forcing and dissipation ranges are separated by large scales. When there is neither forcing nor dissipation, the transport is inertial (see Figure 4.1).

At the boundary between the inertial scales and the dissipation scales, the viscosity becomes important. This boundary is located at the co-called transition length scale l_ν, also known as the Kolmogorov scale. This transition length is proportional to the energy input into the system ϵ and the viscosity ν, which invites the approximate power law

$$l_\nu \propto \nu^\alpha \epsilon^\beta \,. \tag{4.34}$$

The order of magnitude of l_ν can be determined using the following considerations. As the viscosity becomes important, the Reynold's number approaches unity ($Re \sim 1$). This corresponds to an inertial force term (F_i) that is approximately balanced by the viscous force term (F_ν),

$$\mathbf{v} \cdot \nabla \mathbf{v} \sim \nu \nabla^2 \mathbf{v} \, . \tag{4.35}$$

Using order of magnitude relations, we get

$$\frac{v^2}{l_\nu} \sim \nu \frac{v}{l_\nu^2} \, . \tag{4.36}$$

Solving for the transition length l_ν gives

$$l_\nu \sim \frac{\nu}{v} \, . \tag{4.37}$$

In order to express v in terms of ϵ, we note that in a turbulent steady-state the energy dissipated by the viscous force is equal to the injected energy ϵ,

$$\epsilon \sim F_\nu v \sim \nu \frac{v^2}{l_\nu^2} \, . \tag{4.38}$$

Rearranging the above two relations and solving for the transition length l_ν gives

$$l_\nu \sim \left(\frac{\nu^3}{\epsilon} \right)^4 \, . \tag{4.39}$$

Kolmogorov's theory of a "cascade" of energy transport from large scales to small scales is based on the "local hypothesis" that the energy flux is transferred most efficiently between eddies of similar size until it begins to be dissipated at $k_\nu = 1/l_\nu$. The scaling for the turbulent heat flux spectrum in neutral fluids can be qualitatively derived as follows. Writing the total energy in spectral notation (setting units of mass to unity), we get

$$E_v = \langle \frac{v^2}{2} \rangle_V = \int E(k) \, dk \, . \tag{4.40}$$

Dimensionally, energy has the units $[L^2/T^2]$, while in spectral notation it has the units $[L^3/T^2]$. Kolmogorov assumes that the energy flux spectrum in the inertial range depends only on the local scales k and the energy flux ϵ (and not on viscosity ν),

$$E(k) \sim k^{\alpha}\epsilon^{\beta} \, . \tag{4.41}$$

Dimensional analysis gives

$$[E(k)] = \left[\frac{1}{L}\right]^{\alpha} \left[\frac{L^2}{T^3}\right]^{\beta} = \left[\frac{L^3}{T^2}\right] \, . \tag{4.42}$$

where we can solve the equations $\beta = 2/3$ and $2\beta - \alpha = 3$ to give $\alpha = -5/3$ and

$$E(k) \sim k^{-5/3}\epsilon^{2/3} \, . \tag{4.43}$$

This scaling is illustrated in Figure 4.1 and is a surprisingly accurate description of turbulent transport spectrum in the inertial range of neutral fluids.

While not naïvely transferable to plasmas, the general features of the above model of neutral turbulence are preserved when studying fusion plasmas. For example, an effective "gyrokinetic inertial range" in a perpendicular free energy cascade has been identified for ITG turbulence [87]. However, this effective inertial range is different from the inertial range in neutral fluid turbulence, because technically a clear separation between the forcing and the dissipative range is non-existent in plasma turbulence due to the presence of damped modes at all wavenumbers [88]. For example, this can be due to Landau damping, which is an additional dissipation mechanism that is unique to plasma turbulence [71, 89]. Nonetheless, in plasma turbulence the effective inertial range is bounded at the large scales by a net turbulence drive from background gradients and at small scales by a net dissipation via collisions. Moreover, in the numerical study of fusion plasmas, the study of turbulent transport over the entire wavenumber range of unstable modes still poses a challenge for even the most modern supercomputers. As a result, it sometimes becomes necessary to employ so-called GyroLES techniques. These have been developed to replace unresolved wavenumbers with

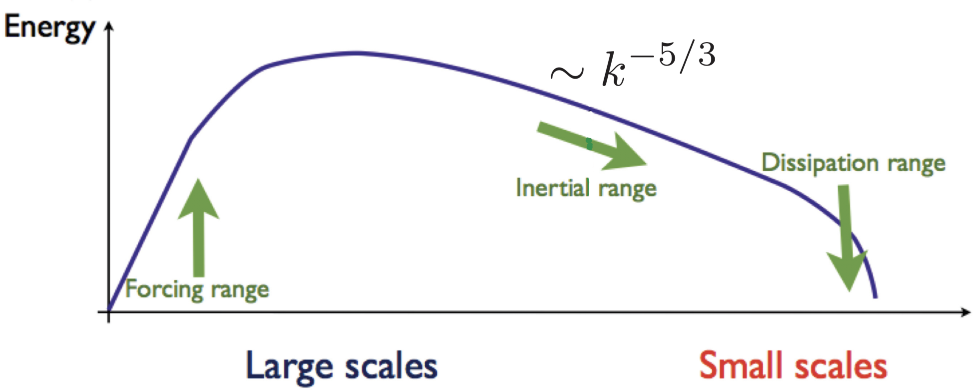

Figure 4.1: Illustration of the Kolmogorov scaling in the inertial range of the turbulent heat flux spectrum. Reprinted with permission from [79].

a model and thereby avoid the unphysical build-up of free energy at the highest resolved wavenumbers [90–92] (see Figure 4.2).

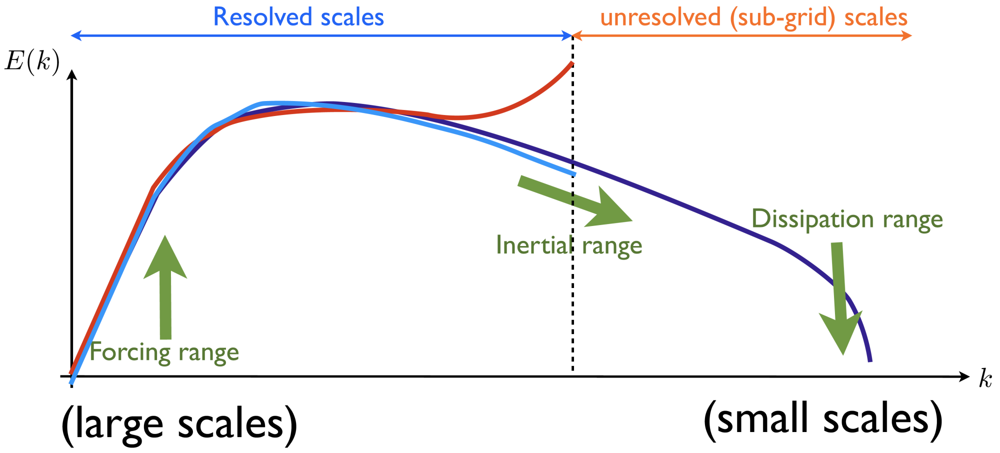

Figure 4.2: Illustration of the GyroLES method. The GyroLES tool approximates any unresolved dissipation (*purple curve*) with a model, avoiding an unphysical build-up of free energy at the highest resolved wavenumbers (*red curve*) and ensuring that the resolved wavenumber domain represents reality (*blue curve*). Reprinted with permission from [79].

Given the above physical and practical motivation for GyroLES techniques, we now briefly summarize its implementation. Recall that the gyrokinetic equations solved by GENE can be expressed as (see Eq. 3.60)

$$\frac{\partial g_{kj}}{\partial t} = L\left[g_{kj}\right] + D\left[g_{kj}\right] + N\left[g_{kj}, g_{kj}\right] \ . \tag{4.44}$$

When we now reduce the number of grid points in the perpendicular direction (n_x, n_y), then this can be thought of as a form of filter. This filter is time-independent and also commutes with the gradient operators in the terms L and D, but not N [79]. Writing the filtered quantities Q as $\widehat{Q}$, we get

$$\frac{\partial \widehat{g}_{kj}}{\partial t} = L\left[\widehat{g}_{kj}\right] + D\left[\widehat{g}_{kj}\right] + \widehat{N}\left[g_{kj}, g_{kj}\right] \,, \tag{4.45}$$

where $\widehat{N}$ still depends on the unfiltered distribution function g_{kj}. This can now be separated into two components

$$\widehat{N}\left[g_{kj}, g_{kj}\right] = N\left[\widehat{g}_{kj}, \widehat{g}_{kj}\right] + M\left[\widehat{g}_{kj}\right] \,, \tag{4.46}$$

where $M\left[\widehat{g}_{kj}\right]$ is a model representing the unresolved nonlinear interaction using the resolved and filtered distribution function $\widehat{g}_{kj}$. This model term takes the general form

$$M\left[c_\perp, \widehat{\Delta}, \widehat{g}_{kj}\right] = -c_\perp \widehat{\Delta}^{n+1/3} k_\perp^n \widehat{h}_{kj} \,, \tag{4.47}$$

where $c_\perp$ is an effective dissipation coefficient that is proportional to the free energy flux, $\widehat{h}_{kj}$ is the resolved non-adiabatic part of the distribution function (see Eq. 3.55), $\widehat{\Delta}$ is an effective filter width defined by the largest resolved scales in Fourier space,

$$\widehat{\Delta} \equiv \frac{1}{k_{\perp,\max}} \,, \tag{4.48}$$

and $k_\perp$ is the perpendicular wavenumber of turbulent fluctuations,

$$k_\perp^2 = g^{xx} k_x^2 + 2 g^{xy} k_x k_y + g^{yy} k_y^2 \,. \tag{4.49}$$

On dimensional grounds $c_\perp \propto \epsilon_f^{1/3}$, where ϵ_f is the free energy flux. The free energy flux is assumed to be constant from scale to scale in the effective gyrokinetic inertial range. Therefore, care must be taken to choose the resolved scales $k_{\perp,\max}$ such that they fall within this range. The above model can be further refined to take into account anisotropies in the perpendicular directions,

$$M\left[c_x, c_y, \widehat{\Delta}_x, \widehat{\Delta}_y, \widehat{g}_{kj}\right] = -\left(c_x \widehat{\Delta}_x^{n+1/3} k_x^n + c_y \widehat{\Delta}_y^{n+1/3} k_y^n\right) \widehat{h}_{kj}\,. \tag{4.50}$$

Note that the above implementation of LES techniques is similar to the constant 2D hyper-viscosity terms already implemented in many gyrokinetic codes [93]. However, the implementation in GENE by Alejandro Bañón Navarro is presently unique in that the model term is dynamically re-calibrated throughout the simulations (e.g. every 50th timestep). This calibration is carried out at the resolved scales as follows. During the simulation one can estimate the free energy flux ϵ_f from scale to scale by sampling a narrower part of the heat flux spectrum, i.e. up to $k'_\perp < k_{\perp,\max}$. This is equivalent to perturbatively applying a larger filter, $\widehat{\Delta} \to \widehat{\Delta} + \delta > \widehat{\Delta}$. Assuming that an effective gyrokinetic inertial range exists, where ϵ_f is approximately conserved from scale to scale, one can calculate ϵ_f at $k'_\perp$ and ensure that the free energy is conserved between $k'_\perp$ and $k_{\perp,\max}$ by introducing the appropriate artificial dissipation in the range $k'_\perp < k_\perp \leq k_{\perp,\max}$. This ensures that the free energy does not build up to unphysical levels at $k_{\perp,\max}$ due to unresolved dissipation at larger wavenumbers, $k_\perp > k_{\perp,\max}$. For adequate calibration, it is important that the largest resolved wavenumber $k_{\perp,\max}$ is well within the effective gyrokinetic inertial range. Empirically, the dynamically calibrated GyroLES method sacrifices some physical accuracy in exchange for computational savings by a factor of 20 [79]. As a result of these large savings in computational resources, this thesis is able to present multi-scale simulations that resolve both electron scales and ion scales in the near-edge of L-mode plasmas (at $\rho = 0.80$) for the first time.

4.5 Treatment of Geometry

GENE can model the plasma in a local (toroidal flux-tube) or a nonlocal (radial annulus) simulation domain. The local approximation is preferred where applicable, because periodic boundary conditions in both the radial (x) and binormal (y) directions allows us to employ numerically efficient spectral methods.

4.5.1 Flux-Tube Approximation

Considering only single-particle motion, we find that without collisions the particles remain confined to motion on a flux-surface. Due to the toroidal periodicity of the magnetic field, the electromagnetic Lagrangian is independent of toroidal angle and gives a conserved angular momentum,

$$p_{\text{can}} = (mv_\phi - qA_\phi)R \approx mv_\parallel R - q\psi = \text{const.}\,, \tag{4.51}$$

where p_{can} is the canonical momentum, ψ is the poloidal magnetic flux and A_ϕ is the vector potential contributing to the poloidal component of the magnetic field [7]. The total energy E of each particle is another conserved quantity due to time-independence of the Lagrangian,

$$E = \frac{1}{2}mv_\parallel^2 + \mu B = \text{const.} \tag{4.52}$$

Since $v_\parallel$ remains bounded by the conserved energy E and the adiabatic invariant μ, the particle motion is bounded around a certain flux-surface ψ. This motivates the flux-tube approximation.

Throughout a flux-tube, the physical parameters are Taylor expanded to first order around the central coordinate r_0 of the flux-tube. Parameters are therefore varying linearly throughout a flux-tube. For example, the the safety factor $q(r)$ is defined as

$$q(r) \approx q_0 + \left.\frac{dq}{dr}\right|_{r_0} (r - r_0) = q_0 \left(1 + \hat{s}\frac{r - r_0}{r_0}\right)\,, \tag{4.53}$$

where

$$\hat{s} = \frac{r_0}{q_0}\left.\frac{dq}{dr}\right|_{r_0}\,. \tag{4.54}$$

4.5.2 Equilibrium geometry

The coordinate system of the magnetic field geometry presents a natural choice for the coordinate system of gyrokinetic codes. Historically, gyrokinetic codes have initially solved the plasma equations in simplified magnetic geometries such as slab and $s-\alpha$ geometry [94].

Since then, geometries have been devised that are noncircular and able to include finite-aspect-ratio effects [95] (as opposed to only large-aspect-ratio effects [?]). The inclusion of realistic magnetohydrodynamic (MHD) equilibrium geometries has allowed for more accurate simulations of both local and global effects [96]. For example, realistic magnetic geometry has recently been used to predict the formation of internal transport barriers without velocity shear as a result of a combination of high density gradients and a high Shafranov shift [97].

Due to the complexity of magnetic geometry in tokamaks (not to mention stellarators), the coordinate system of choice is based on curvilinear coordinates. The basis vectors in this system are neither orthogonal nor unit vectors, and their length and orientation can vary in space. This can lead to interesting properties (see Appendix A). As a reduced example for

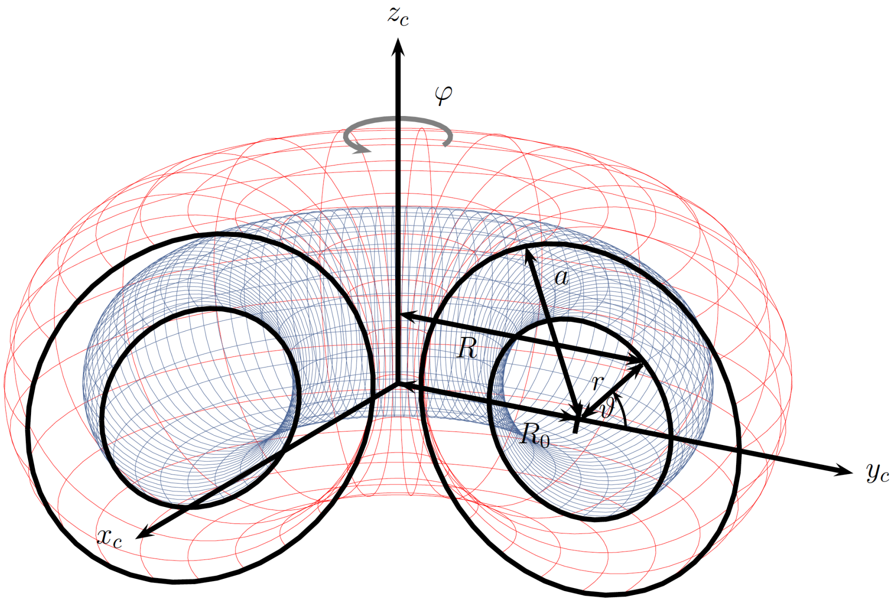

Figure 4.3: Example of a nested toroidal coordinate system. Reprinted with permission from [80].

illustration, the metric tensor components for a nested toroidal coordinate system are given below [80]:

$$
\begin{aligned}
g^{xx} &= 1 \\
g^{yy} &= (\hat{s}z)^2 + \left(\frac{q}{q_0}\frac{r_0}{r}\right)^2 (1 - 2\epsilon\cos\vartheta) - 2\frac{q}{q_0}\epsilon_0\hat{s}z\sin z \\
g^{zz} &= \frac{1}{r^2}(1 - 2\epsilon\cos\vartheta) \\
g^{xy} = g^{yx} &= \hat{s}z - \frac{q}{q_0}\epsilon_0\sin z \\
g^{xz} = g^{zx} &= -\frac{\epsilon\sin z}{r} \\
g^{yz} = g^{zy} &= \frac{1}{r_0}\left[-\hat{s}z\epsilon_0\sin z + \frac{q}{q_0}\frac{r_0^2}{r^2}(1 - 2\epsilon\cos\vartheta)\right] ,
\end{aligned}
\tag{4.55}
$$

where r_0 is the radius of the reference flux surface, q_0 is the magnetic shear at the reference flux surface (see Eq. 4.53), ϵ is the inverse aspect ratio a/R (a is the minor radius and R the major radius of the tokamak), ϵ_0 is the inverse aspect ratio at the reference flux surface r_0/R, ϑ is the poloidal angle as shown in Fig. 4.3.

4.6 Treatment of Collisions

Collisional transport can contribute experimentally relevant levels of heat flux to plasma experiments (see Fig. 4.4). GENE employs several methods to model the effect of collisions. The two main methods are the Landau-Boltzmann collision operator and the more accurate (but also computationally more expensive) Sugama collision operator [98] recently implemented by Paul Crandall into GENE. Their main properties are briefly described below.

4.6.1 Landau-Boltzmann Operator

Recall that the distribution functions are separated into perturbed and Maxwellian background distributions,

$$f_j = F_{0j} + f_{1j}\,, \text{ where } f_{1j} \ll F_{0j}\,. \tag{4.56}$$

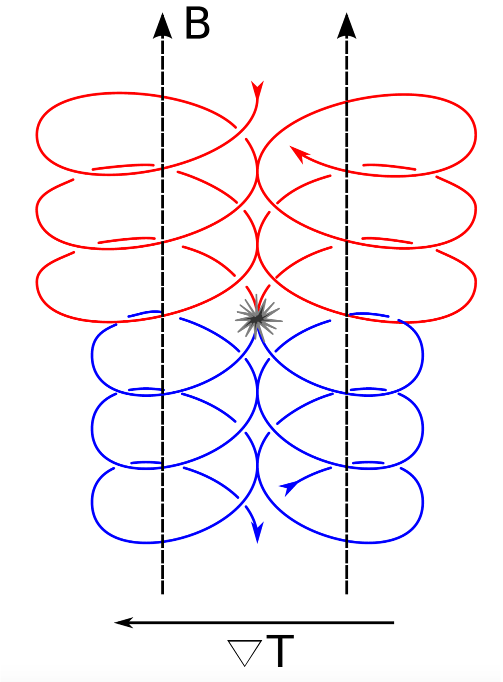

Figure 4.4: Illustration of neoclassical transport. Collisions of charged particles in a magnetic field with a temperature gradient contribute to thermal heat flux perpendicular to the magnetic field. Reprinted with permission from [**?**].

The general Landau collision operator is a bilinear function of the full distribution functions f_j and f_k, where j and k identify the colliding particle species of interest, and can be written as [99]

$$C_{jk}(f_j, f_k)\,. \tag{4.57}$$

With the splitting of the distribution functions into background and perturbed quantities, the Landau-Boltzmann operator can be linearized into C^L_{jk} of the following form

$$C^L_{jk}(f_{1j}, f_{1k}) = C_{jk}(f_{1j}, F_{0k}) + C_{jk}(F_{0j}, f_{1k})\,, \tag{4.58}$$

where the first term $C_{jk}(f_{1j}, F_{0k})$ is the test-particle collision operator and the second term $C_{jk}(F_{0j}, f_{1k})$ is the field-particle collision operator. The field-particle collision operator is ignored in the following for simplicity. The test-particle collision operator is further given by

$$C_{jk}(f_{1j}, F_{0k}) = \nu_D^{jk}(v)\lambda f_{1j} + \mathcal{C}_v^{jk} f_{1j} + \frac{1}{2}\frac{m_j}{T_k}\left(1 - \frac{T_k}{T_j}\right)\frac{1}{v^2}\frac{\partial}{\partial v}\left[\nu_\parallel^{jk}(v)\, v^5 f_{1j}\right], \tag{4.59}$$

where $\nu_D^{jk}(v)$ is the collision frequency for pitch-angle scattering, λ is the pitch-angle scattering operator, $\nu_\parallel^{jk}(v)$ is the energy diffusion frequency, and the operator $\mathcal{C}_v^{jk}$ acts on a general function of velocity $f(v)$ as follows

$$\mathcal{C}_v^{jk} f(v) \equiv \frac{1}{2}\frac{1}{v^2}\left[\nu_\parallel^{jk}(v)\, v^4 F_{0j}\frac{\partial f(v)}{F_{0j}}\right]. \tag{4.60}$$

The above terms and operators are defined in more detail in Ref. [98]. The main purpose of the above equations is to highlight the dependence of the last term in the collision operator of Eq. 4.59 on the temperature ratio T_k/T_j. Mathematically, the linearized Landau collision operator is no longer self-adjoint when the term containing the temperature ratio is non-zero (i.e. when $T_e \neq T_i$ or $T_{\text{Carbon}} \neq T_{\text{Deuterium}}$). Since self-adjointness allows for a more accurate numerical implementation of a collision model, the Sugama collision operator was developed [98].

4.6.2 Sugama Operator

When the collisionality is very high and the temperature ratio between species is far from unity, such as can be found in the near-edge region, the collision operator developed by Sugama *et al.* can be used [98]. The Sugama collision operator, recently implemented by Paul Crandall into GENE, is motivated by its mathematical property of self-adjointness and its physical property of free energy conservation, in addition to the properties already present in the Landau collision operator.

A comparison between the free-energy conservation of the two collision operators in the near-edge (at $\rho = 0.90$) of a DIII-D L-mode plasma is shown in Fig. 4.5. In the simulation with the Landau-Boltzmann collision operator the free energy grows with time. In the simulation with a fourth-order Sugama collision operator (and otherwise identical simulation

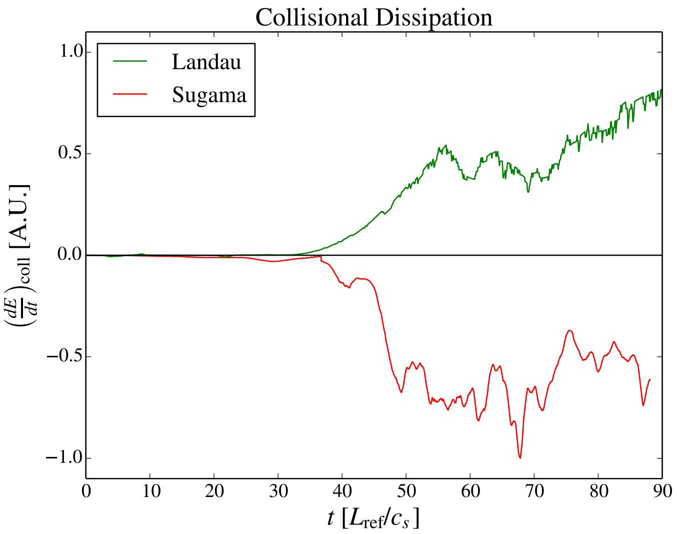

Figure 4.5: Comparison between the Landau-Boltzmann collision operator and the Sugama collision operator at $\rho = 0.90$. When using the Landau-Boltzmann collision operator the free energy was found to grow rather than being dissipated by collisions (*green curve*). This was resolved by using the fourth-order Sugama collision operator, where free energy is dissipated by collisions as expected (*red curve*).

parameters), the free energy is significantly dissipated by collisions, as expected. Collision operators of fourth and sixth order are available to be employed as necessary to ensure free energy dissipation. Note that the Landau collision operator is sufficiently accurate for simulations with lower collisionality and smaller temperature ratio T_i/T_e at a location further inward in the near-edge (at $\rho = 0.80$) of the same L-mode plasma.

4.7 Summary

The main features of the GENE code that were employed in this work have been described above. Of particular importance for the following results are the GyroLES techniques implemented by Alejandro Bañón Navarro, the Sugama collision operator implemented by Paul Crandall, and the $\boldsymbol{E} \times \boldsymbol{B}$ shear implemented by Daniel Told. Without the concomitant resource savings of the GyroLES techniques, the multi-scale simulations presented in this work would not have been affordable with typical supercomputer time allocations at the National Energy Research Scientific Computing (NERSC). Moreover, the improved physical realism of constant $\boldsymbol{E} \times \boldsymbol{B}$ shear in the local flux-tube and of free energy dissipation by the Sugama collision operator are important components of our simulation method. The simulation results are described below.

CHAPTER 5

Gyrokinetic GENE Simulations of DIII-D near-edge L-mode plasmas

Large parts of the following text are from a paper accepted for publication in *Physics of Plasmas* under the title "*Gyrokinetic GENE simulations of DIII-D near-edge L-mode plasmas*" by T. F. Neiser, F. Jenko, T. A. Carter, L. Schmitz, D. Told, G. Merlo, A. Bañón Navarro, P. C. Crandall, G. McKee and Z. Yan (for an earlier version, see arXiv:1808.06607).

5.1 Abstract

We present gyrokinetic simulations with the GENE code addressing the near-edge region of an L-mode plasma in the DIII-D tokamak. At radial position $\rho = 0.80$, simulations with the ion temperature gradient increased by 40% above the nominal value give electron and ion heat fluxes that are in simultaneous agreement with the experiment. This gradient increase is consistent with the combined statistical and systematic uncertainty σ of the Charge Exchange Recombination Spectroscopy (CER) measurements at the 1.6σ level. Multi-scale simulations are carried out with realistic mass ratio and geometry for the first time in the near-edge. These multi-scale simulations suggest that the highly unstable ion temperature gradient (ITG) modes of the flux-matched ion-scale simulations suppress electron-scale transport, such that ion-scale simulations are sufficient at this location. At radial position $\rho = 0.90$, nonlinear simulations show a hybrid state of ITG and trapped electron modes (TEMs), which was not expected from linear simulations. The nonlinear simulations reproduce the total experimental heat flux with the inclusion of $\boldsymbol{E} \times \boldsymbol{B}$ shear effects and an increase in the electron temperature gradient by $\sim 23\%$. This gradient increase is compatible with the

combined statistical and systematic uncertainty of the Thomson scattering data at the 1.3σ level. These results are consistent with previous findings that gyrokinetic simulations are able to reproduce the experimental heat fluxes by varying input parameters close to their experimental uncertainties, pushing the validation frontier closer to the edge region.

5.2 Introduction

In order to improve the energy confinement time of magnetic fusion experiments, a thorough understanding of turbulent transport is necessary. The main carriers of cross-field transport in tokamaks are gyroradius-scale micro-instabilities with scale lengths much smaller than the machine size. These micro-instabilities are physically driven by electron and ion temperature gradients and density gradients. Since microturbulence is suspected to reduce energy confinement time with an increase in heating power, its mitigation is of intrinsic interest to the fusion community.

Paradoxically, a state of improved confinement arises together with steepened gradients in the edge region when the heating power is increased above a certain threshold power, P_{th}. This transition from low confinement mode (L-mode) to high confinement mode (H-mode) was first discovered at the ASDEX tokamak in 1982 and has since been reproduced in all major tokamaks [35,38]. H-mode is the favored operational regime for nuclear fusion reactors and ITER. However, finding a self-consistent description of the L-H transition is a major unsolved problem [38–40]. An important first step towards understanding the L-H transition is to correctly describe L-mode in the near-edge and edge regions. This is also important for ITER, which will be in L-mode during plasma current ramp-up and ramp-down phases; correctly predicting the L-mode profiles is important for vertical stabilization of the plasma during these phases [100, 101]. This motivates a study of micro-instabilities in the L-mode near-edge just before an L-H transition.

Gyrokinetic theory provides an accurate description of microturbulence in magnetically confined plasmas. Here, the assumptions of high background magnetic field, low frequencies relative to the ion cyclotron frequency and small fluctuation amplitudes typically apply [102].

Gyrokinetic codes such as GKV [65, 66], GEM [67, 68], GYRO [58] and GENE [69] have been in good agreement with the experiment and with each other in the core of both L-mode [59, 60, 81] and H-mode [103–105] plasmas. Similarly, the near-edge region of H-mode plasmas has been successfully modeled [103, 104, 106]. However, these codes have been in occasional disagreement in the near-edge of L-mode plasmas. For example, simulations have shown an underprediction of heat transport of ~ 7 for GYRO [59] and ~ 2 for GENE [81] for nominal parameters of DIII-D discharge #128913. This has raised fears of an apparent systematic shortfall of heat flux predictions [59, 60]. However, these fears have recently been reduced [53, 54, 81, 107, 108]. For example, increasing the ion temperature gradient within the experimental error bars has produced flux-matched simulations with GENE [81]. Recent GYRO simulations of a different L-mode discharge, namely DIII-D #101391, have revisited this shortfall problem and found good agreement with experiment [108]. Similarly, the CGYRO code [109] matches the experimental heat flux of this discharge [108], as does the GENE code. Studies with GYRO on the Alcator C-Mod tokamak have also been in good agreement with experiment near the edge region of L-modes, with the use of multi-scale simulations in some cases [53, 54]. These gyrokinetic validation exercises reduce fears that the shortfall is a universal feature of near-edge L-mode plasmas. However, these fears have not been completely removed yet. Moreover, the role of microturbulence and its interactions on multiple scales is still poorly understood in the near-edge. Therefore, there exists a continued need for code validation and microturbulence characterization in the near-edge of L-mode plasmas.

As part of the above gyrokinetic simulation studies, it has become apparent that interactions between microturbulent modes at large and small scales (multi-scale effects) are sometimes important. The microturbulence modes usually seen in the core are Ion Temperature Gradient (ITG), Electron Temperature Gradient (ETG) and Trapped Electron Modes (TEM). These modes are also expected in the near-edge region, in addition to resistive-ballooning modes that can arise due to the high collisionality here [61–63]. In the past, it was thought that experimentally relevant heat flux is mainly carried by TEM and ITG modes [25], because these modes transport energy on scales larger than the ion gyroradius

($k_\perp \rho_i \lesssim 1$), while ETG modes ($k_\perp \rho_i \gg 1$) transport energy on much smaller scales. However, gyrokinetic simulations in the early 2000s by Jenko and Dorland predicted that ETG modes can create radially elongated streamers that can contribute experimentally relevant heat transport [29–31]. This was later demonstrated by observations at the National Spherical Torus Experiment (NSTX) [47] and DIII-D [48]. However, it is not clear how ETG streamers interact with large-scale modes. In principle, this can be answered by multi-scale simulations that resolve the important wavenumber range for both ion- and electron-scale turbulence. Pioneering multi-scale simulations with a reduced mass ratio ($\sqrt{m_i/m_e} \approx 20$) and simplified geometry have found a heuristic rule that can gauge the relevance of the ETG-scale contribution to the overall heat transport [49–52]. More recent multi-scale simulations with realistic mass ratio and geometry in the tokamak core have found that the degree of instability of ITG modes is a critical parameter determining the degree of cross-scale interactions [53–55]. These multi-scale simulations have instructed a recent model for saturation of multi-scale turbulence by zonal flow mixing, which has given rise to another potentially useful heuristic rule for gauging the importance of multi-scale interactions using linear simulations [56]. Since these heuristic rules provide useful physical insight and can save computational resources, it is helpful to validate these rules with further multi-scale simulations.

To address these issues, we present a gyrokinetic validation study of a DIII-D near-edge L-mode plasma just before an L-H transition with the gyrokinetic turbulence code GENE. Our primary finding is that gyrokinetic simulations are able to match the heat-flux in the near-edge[†] of the L-mode plasma at $\rho = 0.8$ and $\rho = 0.9$ within the uncertainty of the experiment at the 1.6σ and 1.3σ levels, respectively. In the course of this validation study, we make three secondary findings. First, current heuristic rules for the relevance of multi-scale effects appear to be on the cautious side; multi-scale simulations at $\rho = 0.80$ suggest that single-scale simulations can be sufficient in a scenario when multi-scale effects are expected, which could increase the realm of applicability of single-scale simulations. Second, the effect

---

[†] We loosely define the near-edge as $0.80 \leq \rho \leq 0.96$, where $\rho = (\Phi/\Phi_{\mathrm{edge}})^{1/2}$ is the toroidal flux radius and Φ_{edge} is the toroidal flux at the separatrix.

of edge $\boldsymbol{E} \times \boldsymbol{B}$ shear is found to be already important in the near-edge at $\rho = 0.90$, which was unexpected. Third, nonlinear simulations at $\rho = 0.90$ find a hybrid ion temperature gradient (ITG)/ trappend electron mode (TEM) scenario, which was not obvious from linear simulations. This successful validation exercise helps push the gyrokinetic validation frontier closer to the L-mode edge region.

5.3 Summary of Experimental Data

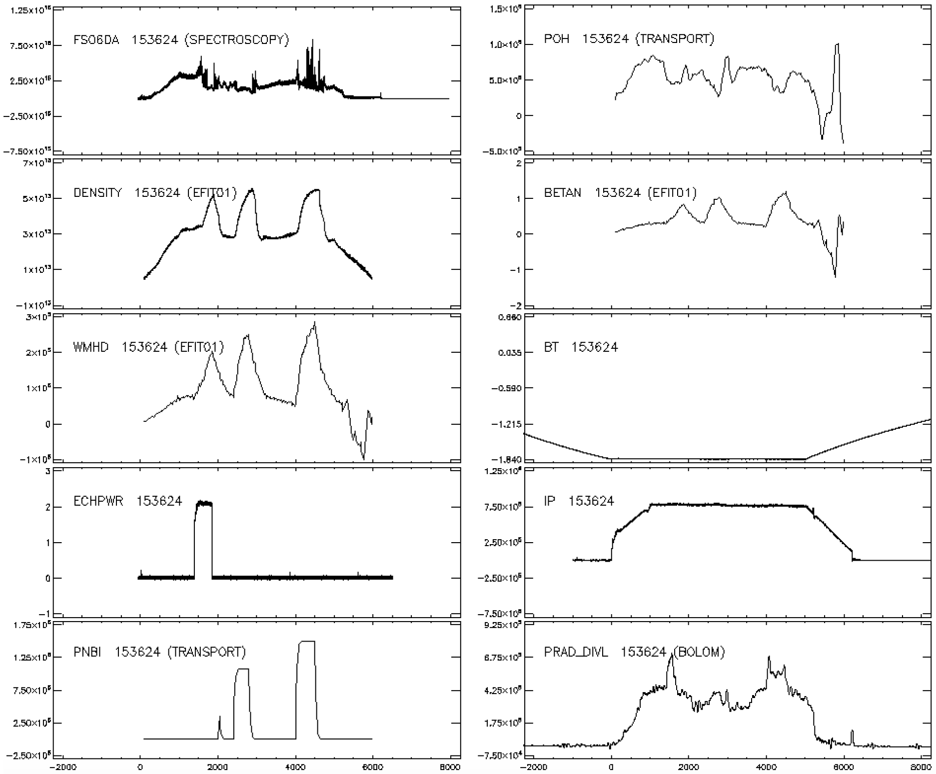

Figure 5.1: Time traces of various properties of DIII-D discharge #153624. From top to bottom in the left column, we have plotted the D_α recycling light emission, the line integrated density, the total energy stored in the plasma, the electron cyclotron heating (ECH) power and the NBI heating power. From top to bottom in the right column, we have plotted the ohmic heating power, the normalized plasma beta, the toroidal magnetic field, the plasma current and the power radiated in the lower diverter. The plots show that the plasma undergoes three L-H transitions, the first from ECH and the second two from NBI heating.

The subject of this study is DIII-D discharge #153624. This discharge exhibits three L-H transitions, where the first was induced with Electron Cyclotron Resonance Heating

(ECRH) and the following two with Neutral Beam Injection (NBI) heating (see Fig. 5.1). Note the marked variation in line integrated density and total energy stored in the plasma as the plasma transitions three times between low and high confinement modes. Figure 5.2 shows highly resolved time-traces taken at $\rho = 0.96$ during the second L-H transition (since we focus our study on $t_0 = 2400$ ms, only data relevant to this transition is shown). Note

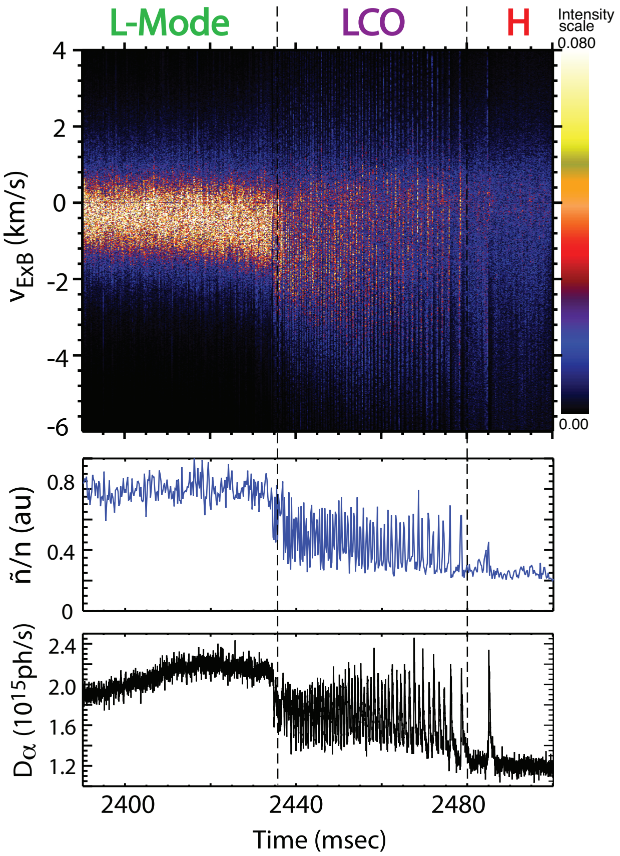

Figure 5.2: Time traces of $v_{E\times B}$ shear velocity, density fluctuation amplitude and D_α recycling light emission at $\rho = 0.96$ during an L-H transition. This work studies the L-mode in the near-edge, defined here as $0.80 \leq \rho \leq 0.96$, and focuses at $t = 2400$ ms, before transition times $t_{\text{LCO}} = 2436$ ms and $t_{\text{H}} = 2480$ ms shown by vertical dashes.

the remarkable change in density fluctuation amplitude $\tilde{n}/n$ and divertor D_α recycling light emission as the plasma changes its operational state from L-mode to H-mode via an extended phase of Limit Cycle Oscillations (LCOs) [64, 110]. The $\boldsymbol{E} \times \boldsymbol{B}$ velocity $v_{E\times B}$ and density fluctuation amplitude were obtained with the Doppler Backscattering (DBS) diagnostic [111], which probes a wavenumber range of $0.3 \lesssim k_y\rho_s \lesssim 0.6$.

The plasma is in the lower single-null shape, where the ion ∇B-drift direction is towards the single active X-point and the power threshold for the L-H transition is relatively low (as compared to the upper single-null shape) [38]. Therefore, the neutral beam is deliberately operated at a relatively low beam power of 1.1 MW, which is in the vicinity of this power threshold. In steady-state operation, this heating power plus Ohmic heating is comparable to the total heat flux relevant for flux-matching gyrokinetic simulations. Note that the heat flux is typically carried by radiation losses and by radial conductive and convective transport due to microturbulence in the electron and ion channels, which are sometimes difficult to separate empirically at moderate to high collisionality.

This work will focus on a constant time $t_0 = 2400$ ms, because this is when the turbulence is still in a quasi-steady equilibrium state before the L-H transition begins (see Fig. 5.2). At t_0 the plasma has temperature and density profiles as shown below in Figure 5.3. Both the

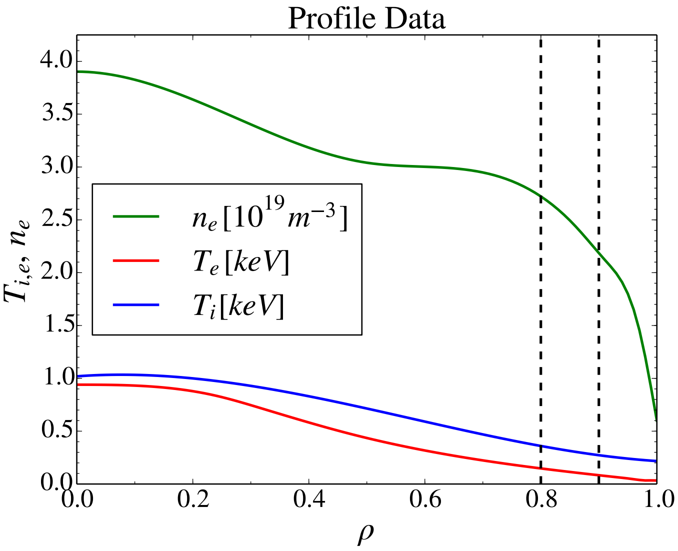

Figure 5.3: Experimental profiles of electron density (*green*), electron temperature (*red*) and ion temperature (*blue*). This work studies the L-mode plasma in the near-edge with nonlinear simulations at $\rho =$ 0.80 and $\rho = 0.90$ as indicated by the vertical dashes.

electron temperature and density are measured by the Thomson scattering diagnostic. This method produces highly resolved profile data for the electrons, but cannot be used effectively for the ions. This is due to their much lower Thomson scattering cross section σ_t, which scales as $\sigma_t \propto 1/m_j^2$, where m_j is the mass of the scattered charge. Therefore, a Charge Exchange Recombination Spectroscopy (CER) diagnostic is used for the impurity ions, which studies the emission lines from neutral beam injection. Specifically, the impurity ion CER diagnostic detects predominantly charge exchange recombination radiation from fully ionized impurity Carbon ions (C^{6+}). The measured Carbon temperature profile is assumed to be equal to the Deuterium ion temperature profile in this discharge.

In general, the comparatively lower detection number statistics of CER data versus Thomson data causes the statistical uncertainty of the ion temperature to be larger than the uncertainty in the electron temperature (see Fig. 5.4). For instance, the statistical uncertainty for the ion temperature gradients at $\rho = 0.80$ is estimated to be $\sigma_{\text{ITG, stat}} \sim\ 15\%$ (see Section 5.4). On the other hand, the statistical uncertainty in the electron temperature gradient (ETG) at $\rho = 0.90$ is estimated to be $\sigma_{\text{ETG, stat}} \sim 8\%$. Moreover, the systematic uncertainty for both electron and ion temperature gradients is estimated to be $\sigma_{\text{sys}} \sim 10\%$. Recall that only slightly more than two thirds (68%) of normally distributed measurements fall within $1\sigma_{\text{stat}}$, while most (95%) fall within $2\sigma_{\text{stat}}$ and nearly all (99.7%) fall within $3\sigma_{\text{stat}}$ of the mean. Therefore, changes in temperature gradient of up to $\leq 2\sigma_{\text{stat}} + 1\sigma_{\text{sys}}$ can reasonably be attributed to combined uncertainties in the measurement and model assumptions[*].

The physical parameters at four radial positions in the near-edge and edge region are summarized in Table 5.1. The variables in the table are defined as follows. The logarithmic gradients are defined as

$$\omega_X = -\frac{1}{X}\frac{dX}{d\rho}\,,\ \text{with}\ X \in \{T_i, T_e, n\}\,, \tag{5.1}$$

where $\rho = (\Phi/\Phi_{\text{edge}})^{1/2}$ is the toroidal flux radius normalized by Φ_{edge}, which is the toroidal flux at the separatrix. The shear parameter is given by

$$\hat{s} = \frac{\rho}{q}\frac{dq}{d\rho}\,, \tag{5.2}$$

where q is the safety factor. The electron beta is defined as the ratio of thermal to magnetic

---

[*] We conservatively add statistical and systematic errors linearly rather than in quadrature.

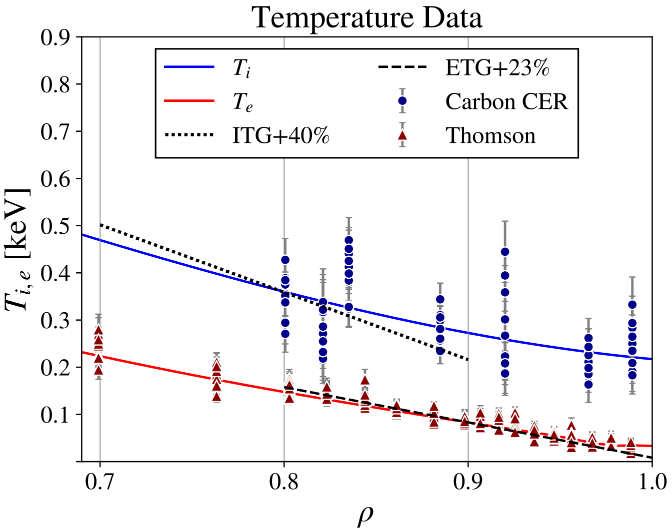

Figure 5.4: Close-up view of electron (*red line*) and ion temperature profiles (*blue line*) with experimental data from the CER (*blue circles*) and Thomson diagnostics (*red triangles*). The data was collected in a ±20 ms time window centered at $t_0 = 2400$ ms. The total (systematic and statistical) uncertainty σ in the ion temperature gradient (ITG) at $\rho = 0.80$ is estimated to be $\sigma_{\mathrm{ITG}} \sim 25\%$. The uncertainty in electron temperature gradient (ETG) at $\rho = 0.90$ is estimated to be $\sigma_{\mathrm{ETG}} \sim 18\%$ (see Section 5.4). For reference, we show a 40% increase in ITG at $\rho = 0.80$ (*dotted line*) and a 23% increase in ETG at $\rho = 0.90$ (*dashed line*).

pressure,

$$\beta_e = \frac{n_e T_e}{B_{\mathrm{ref}}^2/2\mu_0}\,, \tag{5.3}$$

where B_{ref} is the magnetic field on axis and the other variables take their usual meaning. The effective atomic number of the plasma, $Z_{\mathrm{eff}} = \Sigma_i Z_i^2 n_i/n_e$, is greater than that of a pure Deuterium plasma ($Z = 1$) mostly due to Carbon impurities that enter the plasma from the divertor and the wall. The electron-ion collision frequency is defined as

$$\nu_{ei} = \frac{Z_{\mathrm{eff}} n_e e^4 \ln\Lambda}{2^{7/2}\pi\epsilon_0^2 m_e^{1/2} T_e^{3/2}}\,, \tag{5.4}$$

where $\ln\Lambda$ is the Coulomb logarithm and other variables take their usual meaning. Convenient reference lengths are given by $L_{\mathrm{ref}} = \sqrt{\Phi_{\mathrm{edge}}/\pi B_{\mathrm{ref}}}$ and $\rho_s = \sqrt{T_e m_i/e^2 B_{\mathrm{ref}}^2}$. For example, we will use ρ_s to rescale the wavenumber of turbulent modes as $k_y\rho_s$. For a better comparison with other work, a conversion from $k_y\rho_s$ to the toroidal mode number n is useful.

ρ	0.80	0.85	0.90	0.95
Time/[s]	2.40	2.40	2.40	2.40
$\hat{s}$	1.41	1.98	2.98	5.18
q	2.86	3.15	3.69	4.47
ω_{T_i}	2.78	2.80	2.68	2.32
ω_{T_e}	4.69	5.62	7.32	13.51
ω_{n_e}	1.34	2.21	2.91	7.05
$\beta_e\,/[\%]$	0.0557	0.0396	0.0252	0.0132
$T_i\,/[\mathrm{keV}]$	0.360	0.320	0.281	0.244
$T_e\,/[\mathrm{keV}]$	0.148	0.119	0.0831	0.0531
$n_e\,/[10^{19}\,\mathrm{m}^{-3}]$	2.72	2.68	2.19	2.12
Z_{eff}	1.80	1.80	1.80	1.80
$\nu_{ei}\,/[c_s/L_{\mathrm{ref}}]$	7.28	10.9	17.8	35.21
$B_{\mathrm{ref}}\,/[\mathrm{T}]$	1.70	1.70	1.70	1.70
$L_{\mathrm{ref}}\,/[\mathrm{m}]$	0.770	0.770	0.770	0.770
$\rho_s\,/[10^{-3}\mathrm{m}]$	1.03	0.927	0.775	0.619
$n\,/[k_y\rho_s]$	208	224	242	264

Table 5.1: Physical parameters for radial positions in the near-edge region, with variables as defined in the text.

The conversion factor is given by the relation [107]

$$\frac{n}{k_y\rho_s} = \frac{\rho}{q}\frac{L_{\mathrm{ref}}}{\rho_s}\,, \tag{5.5}$$

which is evaluated numerically in the bottom row of Table 5.1.

In this work, we also take into account the effect of the $\boldsymbol{E}\times\boldsymbol{B}$ shearing rate, which is a function of both the radial electric field gradient and the magnetic field geometry. For realistic geometry, the $\boldsymbol{E}\times\boldsymbol{B}$ shearing rate is given by the so-called Hahm-Burrell formalism [112],

$$\omega_{E\times B} = \frac{cRB_\theta}{B}\frac{d}{dr}\left(\frac{E_r}{B_\theta R}\right)\,, \tag{5.6}$$

where E_r is the radial electric field, B_θ is the poloidal component of the magnetic field B, and R is the major radius. Note that $(E_r/B_\theta R)$ is constant on the flux surface, but the factor cRB_θ/B is not constant (it is larger on the outboard midplane). In the simulation community, a flux-surface-averaged formalism for the $\boldsymbol{E}\times\boldsymbol{B}$ shearing rate in shaped geometry is often used for simplicity [113],

$$\omega_{E\times B} \approx \frac{r}{q}\frac{d}{dr}\left(\frac{E_r}{B_\theta R}\right) , \tag{5.7}$$

where the factor preceding the derivative, r/q, is now a flux function. The present work will also employ this so-called Waltz-Miller formalism. The experimental shearing rate values are inferred using data from the magnetic field geometry and the Doppler Backscattering diagnostic (see Fig. 5.5).

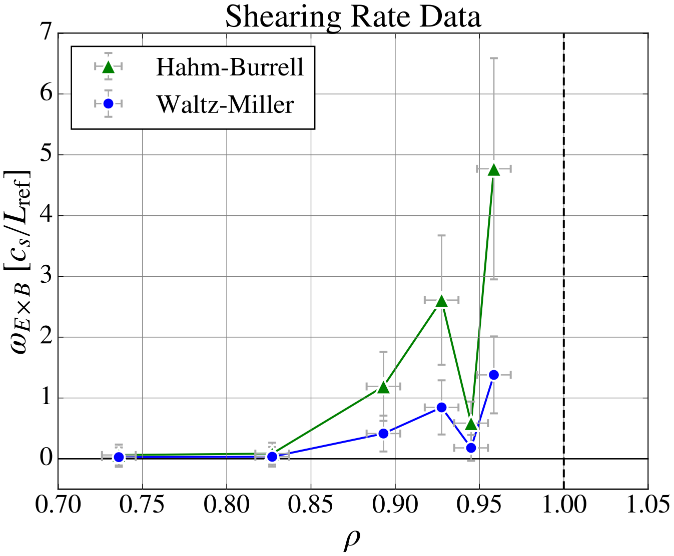

Figure 5.5: The Hahm-Burrell shearing rate in the edge region, as evaluated by magnetic field geometry and the Doppler Backscattering measurements at the outboard midplane (*green triangles*). A flux-surface average of the Hahm-Burrell rate is known as the Waltz-Miller rate and commonly used in the simulation community (*blue circles*). The flow shear generally increases towards the separatrix (*dashed line*).

5.4 Error analysis

In order to quantify the statistical uncertainty of the ion temperature data, a χ^2 fitting procedure is employed. As theoretical model for the temperature, we use a polynomial of the lowest order ($n = 3$) that can pass through all data points within their uncertainty, namely

$$T_{i,\mathrm{th}}(\rho) = a(\rho - 0.80)^3 + b(\rho - 0.80)^2 + c(\rho - 0.80) + T_{i,0}\,, \tag{5.8}$$

where $T_{i,0}$ is the temperature at $\rho = 0.80$. Note that this model does not rely on the underlying physics that generates this profile, but rather represents a suitable functional form. We assume that experimental temperature measurements $T_{i,\mathrm{exp}}(\rho)$ are independent and normally distributed, inviting a χ^2 statistic

$$\chi^2(\theta) = \sum_i \frac{[T_{i,\mathrm{th}}(\rho_i) - T_{i,\mathrm{exp}}(\rho_i)]^2}{\sigma_i^2}\,, \tag{5.9}$$

where $\theta = (a, b, c, T_{i,0})$ are the free parameters. We want to quantify the error associated

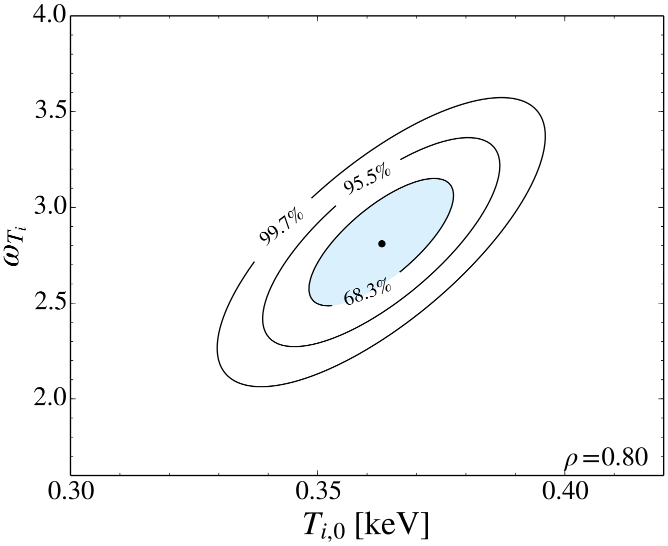

Figure 5.6: Illustration of the χ^2 contours when only varying ω_{T_i} and T_i while keeping the remaining free parameters fixed at their best-fit values. The shaded region corresponds to a 1σ variation around the best-fit value.

with the temperature gradient,

$$\nabla T_{i,\mathrm{th}}(\rho = 0.80) = c\,. \tag{5.10}$$

We use Bayes' theorem to find the probability density function (PDF) of the free parameter c,

$$p(c|\theta) = \frac{\int_{-\infty}^{\infty} da \int_{-\infty}^{\infty} db \int_{0}^{\infty} \exp(-\chi^2/2)\, dT_{i,0}}{\int_{-\infty}^{\infty} da \int_{-\infty}^{\infty} db \int_{-\infty}^{\infty} dc \int_{0}^{\infty} \exp(-\chi^2/2)\, dT_{i,0}} \,. \tag{5.11}$$

This gives a best-fit value of $c \approx 1.0 \pm 0.15\,(\text{stat.})$ keV or $\sigma_{\text{ITG, stat}} \sim 15\%$. One known weakness of the χ^2 fitting procedure is that it assumes the theoretical model is correct. To account for possible systematic errors in the model assumptions, e.g. a polynomial fit to the data, and the experimental setup, e.g. neutral beam halo effects [114] or Zeeman splitting of the (Carbon) impurity line used for CER [115], we allow for a systematic uncertainty of $\sigma_{\text{ITG, sys}} \sim 10\%$. This gives a total uncertainty of

$$\sigma_{\text{ITG}} \sim 25\% \,. \tag{5.12}$$

Thus the nominal experimental value of the logarithmic ion temperature gradient at $\rho = 0.80$ has a combined statistical and systematic uncertainty of $\omega_{T_i} = 2.78 \pm 0.70$. Note that a gradient increase of 40% satisfies the condition of $\leq 2\sigma_{\text{ITG, stat}} + 1\sigma_{\text{ITG, sys}}$, such that this gradient increase may reasonably be associated with the uncertainty in the temperature measurements alone.

The above method is also used to estimate the uncertainty in the electron temperature gradient at $\rho = 0.90$. We find that a third order polynomial fits the electron temperature data well in the range $0.33 < \rho < 1.00$, which supplies a sufficiently large data set for our error analysis. Applying equations (5.8)-(5.11) to this scenario gives a statistical uncertainty of $\sigma_{\text{ETG, stat}} \sim 8\%$ for the electron temperature gradient at $\rho = 0.90$. However, the temperature profile of a tokamak plasma is subject to microscopic fluctuations due to predator-prey dynamics between gradient-driven microturbulence and zonal flows [64, 110]. While these dynamics have been observed at large scales, current experimental techniques do not yet capture these dynamics on small scales. Therefore, a systematic uncertainty in the temperature gradients is physically motivated. Allowing for a systematic uncertainty of

$\sigma_{\mathrm{ETG,\,sys}} \sim 10\%$ gives a total uncertainty of

$$\sigma_{\mathrm{ETG}} \sim 18\%\,. \tag{5.13}$$

Therefore, an increase in the electron temperature gradient by 23% would consistent with the combined statistical and systematic uncertainty σ of the experimental value at the $\sim 1.3\sigma$ level. Note that this gradient increase also satisfies condition of $\leq 2\sigma_{\mathrm{ETG,\,stat}}+1\sigma_{\mathrm{ETG,\,sys}}$, such that it may reasonably be associated with the uncertainty in the temperature measurements alone.

5.5 Gyrokinetic Simulation Method

Throughout this work, we employ the gyrokinetic turbulence code GENE [69]. The gyrokinetic approximation reduces the six-dimensional phase space to five dimensions by averaging over a charged particle's gyro-motion perpendicular to the magnetic field, and removes several phenomena on small space-time scales. The resulting Vlasov equation can be coupled self-consistently to Maxwell's equations. GENE is a Eulerian code that solves the relevant equations on a field-aligned coordinate system ($\boldsymbol{x}$, $v_{\parallel}$, μ), which minimizes the necessary number of grid points [116, 117]. Here, $v_{\parallel}$ represents the velocity along the field lines and μ is the magnetic moment resulting from the gyro-averaged motion of a charge.

GENE can model the plasma in a local (toroidal flux-tube [118]) or a global (radial annulus) simulation domain. The local approximation is preferred where applicable, because periodic boundary conditions in both the radial (x) and binormal (y) directions invite numerically efficient spectral methods. The local approximation holds where the turbulent correlation lengths are smaller than the gradient scale lengths, such that the plasma parameters do not vary much across a typical turbulent structure. This condition appears to be satisfied in the near-edge region of the L-mode plasma considered here, so we will use the local approach throughout this work.

In our nonlinear simulations we consider two particle species (electrons and Deuterons), and thereby neglect the effect of Carbon as motivated by linear simulations presented below in section 5.6 and 5.8. Electromagnetic effects are included in our simulations by solving for the parallel component of Ampère's law. Moreover, GyroLES techniques were used to model dissipation at unresolved wavenumbers, thus avoiding the unphysical build-up of energy at the highest resolved wavenumbers [90–92]. The flux-tube geometry is calculated with the TRACER-EFIT interface [119]. Due to the high collisionality in the near-edge region, a collision operator developed by Sugama *et al.* was used [98].

It became evident that the effects of sheared flow on turbulent heat transport can be ignored at $\rho = 0.80$ but need to be included closer to the edge region at $\rho = 0.90$ (see Fig. 5.5). The radial flow shear can have an important effect, because it shears turbulent eddies in the poloidal direction, which increases their poloidal correlation length and reduces their radial correlation length [83–85]. This can lead to experimentally relevant improvements in particle and energy confinement. Specifically in GENE, the constant Waltz-Miller shearing rate throughout the flux-tube is implemented using a method developed by Hammett *et al.* [86]. Here, a transformation into the co-moving coordinate system of the equilibrium flow and a discrete time evolution of the sheared radial wavenumber greatly reduce computational intensity while maintaining acceptable numerical accuracy [86].

In order to investigate the interaction between strong ETG streamers and ion-scale modes, it is instructive to carry out multi-scale simulations resolving both ion and electron scales. These simulations are very computationally intensive and cannot currently be carried out resolving the full wavenumber domain of linearly unstable modes. Therefore, a reasonable reduction in the resolved wavenumber domain is sought with nonlinear single-scale simulations. For example, nonlinear electron-scale simulations with varying $k_{y,\max}\rho_s$ can help determine the reliability of GyroLES techniques; they help identify a reasonable maximum extent of the wavenumber domain that still captures the main nonlinear turbulent transport. A similar nonlinear scan in $k_{y,\min}\rho_s$ is carried out at the ion scales to determine a feasible multi-scale simulation domain that still captures the majority of the ion-scale physics. With this method, we are able to carry out multi-scale simulations with realistic electron-Deuteron mass ratio and realistic geometry for the first time in the near-edge, at $\rho = 0.80$.

Throughout this work, the simulation domain in velocity space extends in the parallel direction up to $v_{\parallel,\max} = 3v_{\mathrm{th},j}$, where $v_{\mathrm{th},j} = \sqrt{2T_{0,j}/m_j}$ is the thermal velocity. In the perpendicular direction, it extends to $\mu_j = 9T_{0,j}/B_{\mathrm{ref}}$. Further details of the simulation method, such as the number of grid points or the radial size of the simulation box, are described together with the results of the relevant nonlinear simulation. Throughout this work, the GyroLES methods, the Sugama collision operator and the inclusion of $\boldsymbol{E} \times \boldsymbol{B}$ shear effects mentioned above are of particular relevance.

5.6 Results at first radial position ($\rho = 0.80$)

All micro-instabilities ultimately saturate due to nonlinear interactions between modes of differing wavenumbers. Nonetheless, linear simulations often give useful insight into the nature of the nonlinear instabilities. Generally, the distribution of linear growth rates in wavenumber space highlights the scales of the nonlinear turbulent drive. This can inform the size of the nonlinear simulation box. Moreover, sensitivity of these linear growth rates to changes in physical parameters such as temperature gradients can help identify the nature of modes encountered in nonlinear simulations. Therefore, we will first present linear simulation results, followed by nonlinear simulation results.

5.6.1 Linear Simulations

In the following we have used the initial value solver and the eigenvalue solver in GENE to find linear growth rates of modes at the electron and ion scales. This subsection is organized to first cover the linear simulation results at $\rho = 0.80$ and subsequently interpret these results in the context of heuristic rules for the relative importance of multi-scale effects. The resolution for these linear simulations, which analyze each k_y mode individually, is $\left(n_x, n_z, n_{v_\parallel}, n_\mu\right) = (31, 32, 32, 24)$.

At $\rho = 0.80$, linearly unstable ion temperature gradient (ITG) modes can be identified by the positive frequencies associated with the diamagnetic drift direction of the ions. Similarly, trapped electron modes (TEM) and electron temperature gradient (ETG) modes are identified by the negative frequencies associated with the electron diamagnetic drift direction (see Fig. 5.7). The frequencies of these modes are much smaller than the ion-cyclotron frequency such that the gyrokinetic approximation can be used to describe these modes (see Fig. 5.8). The unstable ITG and TEM/ETG modes are separated by a stable region in wavenumber space ($0.68 < k_y\rho_s < 0.90$). These separate domains allow us to clearly define ion scales ($0.05 \leq k_y\rho_s \leq 0.80$) and somewhat overlapping electron scales ($0.70 \leq k_y\rho_s \leq 180$) for separate nonlinear analysis.

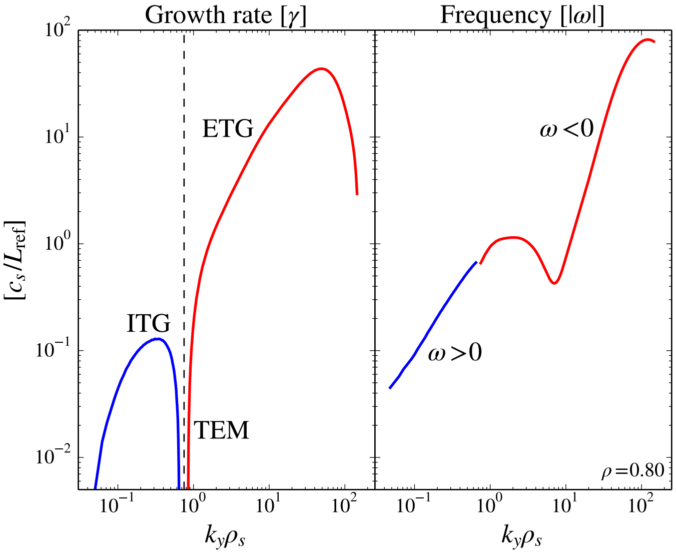

Figure 5.7: Linear growth rates γ (*left*) and absolute values of frequency $|\omega|$ (*right*) as a function of poloidal wavenumber $k_y\rho_s$. The growth rates are separated by a stable region (where $\gamma < 0$) at $0.68 < k_y\rho_s < 0.90$. For nonlinear simulations, we define the ion scales in the domain $0.05 \leq k_y\rho_s \leq 0.80$ and the electron scales in the somewhat overlapping domain $0.70 \leq k_y\rho_s \leq 180$.

It is not clear how the heat fluxes found with nonlinear ion-scale and electron-scale simulations contribute to the collective heat flux. Generally, multi-scale simulations that simultaneously resolve both scale ranges are necessary to answer this question. These simulations are very expensive and may not be possible in all scenarios. A heuristic rule has emerged from pioneering work [49–52] using a reduced mass ratio ($\sqrt{m_i/m_e} = 20$) and $\hat{s} - \alpha$ geometry, with $\alpha = 0$. Namely, if the ratio of maximum growth rates at the electron and

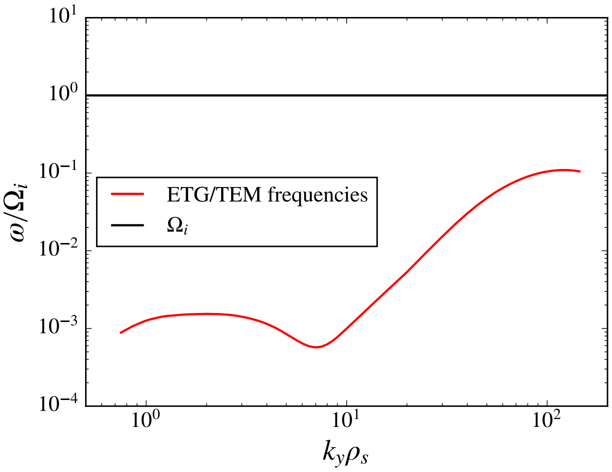

Figure 5.8: Frequencies of the TEM/ETG modes as a fraction of the ion cyclotron frequency at $\rho = 0.80$. For the validity of the gyrokinetic approximation it is necessary (but not sufficient) that $\omega\,/\Omega_i \ll 1$ for all wavenumbers.

ion scales is much larger than the square root of the mass ratio,

$$\gamma_{\mathrm{ETG}}^{\max}\,/\gamma_{\mathrm{ITG}}^{\max} \gg \sqrt{m_i\,/m_e}\,, \tag{5.14}$$

then multi-scale effects could be present. This is because the contributions by the electron-scale turbulence to the overall heat transport could be important. Otherwise, turbulent structures at the ion scales disrupt the efficient heat transport at the electron scales. In our case the mass ratio is $\sqrt{m_i/m_e} \approx 60$ and the ratio between the maximum growth rates is $\gamma_{\mathrm{ETG}}^{\max}/\gamma_{\mathrm{ITG}}^{\max} = 338$. Therefore our linear simulations with the nominal experimental parameters indicate that multi-scale effects could be present. For an increase in the ion temperature gradient by $\sim 40\%$, we get $\gamma_{\mathrm{ETG}}^{\max}/\gamma_{\mathrm{ITG+40\%}}^{\max} = 161$, so multi-scale effects could also be present at this point in parameter space, according to this rule-of-thumb. More recently, a model for saturation of multi-scale turbulence by zonal flow mixing has been proposed [56]. In this model, an important parameter is the RMS velocity of zonal flows (V_{ZF}), which saturates at $V_{\mathrm{ZF}} = \mathrm{Max}\,(\gamma/k_y)$, where γ is the linear growth rate of a turbulent mode with wavenumber k_y. According to this model, multi-scale effects could be present when

$$\mathrm{Max}\,(\gamma_{\mathrm{ETG}}/k_y) \geq \mathrm{Max}\,(\gamma_{\mathrm{ITG}}/k_y)\ . \tag{5.15}$$

This criterion has been validated on recent multi-scale simulations using realistic mass ratio and geometry [53,54]. For our linear simulations at $\rho = 0.80$, this criterion is satisfied for the cases where the ion temperature gradient (ITG) is at its nominal value or increased by 10%; it is also satisfied when the ITG is increased by 40%, but by a small margin (see Fig. 5.9). Therefore, single-scale simulations are likely not sufficient for the cases considered here and multi-scale simulations will need to be carried out. This will be presented in the following subsection 5.6.2.

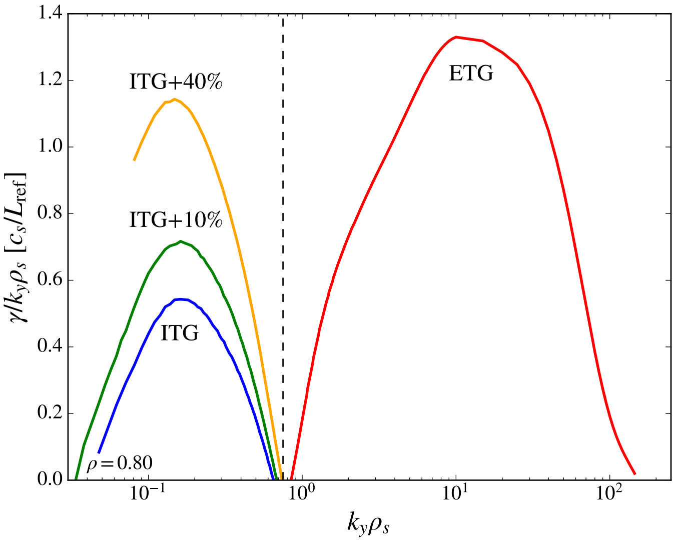

Figure 5.9: Ratio of linear growth rates and poloidal wavenumber ($\gamma/k_y\rho_s$) as a function of wavenumber. For cases where the ITG is nominal (*blue*) or increased by 10% (*green*), the peak of said ratio is smaller at the ion scales than at the electron scales. For the case where the ITG is increased by 40% (*orange*), the difference between the peaks is much less pronounced.

It is not *a priori* clear whether impurities significantly affect turbulence in the Deuterium plasma. The DIII-D tokamak has a Carbon divertor and wall that add Carbon as the main impurity to the Deuterium plasma. Using the impurity ion Charge Exchange Recombination (CER) diagnostic [120], the plasma is observed to have an effective atomic number of $Z_{\mathrm{eff}} = 1.80$ (see Table 5.1). In order to quantify the effect of this impurity, linear simulations are carried out with three particle species, namely Deuterium and Carbon ions, and electrons. We find that the Carbon impurity has a negligible effect on the linear growth rates of ITG modes (see Fig. 5.10). Due to this observation, to first order in accuracy, Carbon

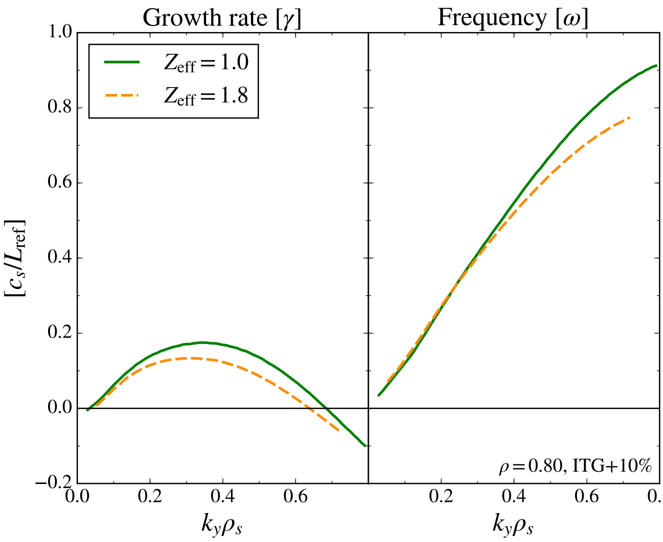

Figure 5.10: Linear growth rates and frequencies for a pure Deuterium plasma (*green*) and for a plasma with an added Carbon impurity species corresponding to $Z_{\rm eff} = 1.8$ (*orange*). For both cases, the ITG is increased by 10%, which is above the nonlinear critical gradient as shown in Figure 5.13. The Carbon impurity has a small effect on the linear growth rates compared to the pure Deuterium plasma.

impurities can be neglected in our nonlinear simulations at $\rho = 0.80$. In summary, linear simulations at $\rho = 0.80$ identify coexisting ITG and ETG modes that could engage in multi-scale interactions.

At each wavenumber, the linear growth rates and frequencies are the imaginary and real roots, respectively, of the linearized dispersion relation. The dependence of the linear growth rates of ITG modes on the ion temperature gradient is illustrated in Figure 5.11. The left panel shows that the growth rates increase with the ITG and that there are regions where $\gamma < 0$ and $\gamma > 0$ for each linear mode (identified by wavenumber). Since the linear mode grows exponentially when $\gamma > 0$ (only to be damped by nonlinear interactions that are not captured in the linear model), the temperature gradient for which $\gamma = 0$ is called the linear critical gradient. The ion temperature gradient for which all linear modes are stable is referred to as the linear critical gradient of the entire plasma (calculated in the left panel of Figure 5.11 to be $\omega_{T_i} = 1.80$). There also exists a critical gradient for nonlinear simulations, where the nonlinearly interacting modes become collectively unstable. Often the linear critical gradient is smaller than the nonlinear critical gradients. The difference

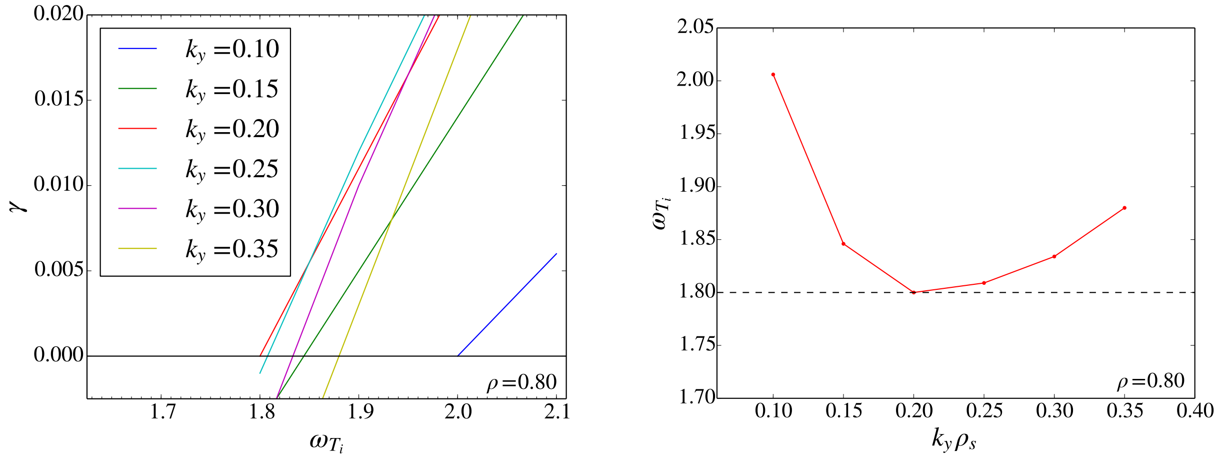

(a) Linear critical gradient for each k_y mode

(b) Minimum linear critical gradient

Figure 5.11: Critical linear ion temperature gradient at $\rho = 0.80$. Linear simulations find a critical linear gradient of $\omega_{T_i} = 1.80$. The difference between the linear and nonlinear critical gradients quantifies the Dimits shift.

between the linear and nonlinear critical gradient is the so-called Dimits shift [121].

5.6.2 Nonlinear Ion-scale Simulations

Fully nonlinear gyrokinetic simulations can be used to diagnose experiments in the hope to improve them in the future. When carrying out these simulations, several steps have to be taken to accurately extract the radial heat flux of the system. After each simulation, we ensure that the perpendicular box size (L_x, L_y) accommodates several correlation lengths of the turbulence. This reduces the effect of boundary conditions on the turbulent structures and avoids their end-to-end connection across the boundaries. We check the grid resolution for convergence, $(n_x, n_y, n_z, n_{v_\parallel}, n_\mu)$, by repeating a certain run with higher resolution in certain dimensions and checking for consistency with previous runs. This is particularly important closer to the edge, where high shear ($\hat{s} > 2$) demands high radial resolution [107]. Computational expense on the order of ten million CPU hours (MCPUh) of multi-scale simulations presently restricts convergence tests to the single-scale simulation domain. To ensure an accurate reading of the simulated heat flux, it is averaged over a time greatly exceeding the turbulent correlation time.

Nonlinear ion-scale simulations are performed with grid points

$$(n_x, n_y, n_z, n_{v_\parallel}, n_\mu) = (256, 64, 24, 32, 24) \tag{5.16}$$

and perpendicular box size $(L_x, L_y) = (140\rho_s, 126\rho_s)$. For the nominal experimental parameters as input we see a nonlinear quench of radial ion heat fluxes (see Fig. 5.12). This is due to the formation of a strong poloidal zonal flow (see lower inset, Fig. 5.13). Continuing the simulation for several hundred time units ($\sim 400\ L_{\mathrm{ref}}/c_s$) to ensure nonlinear saturation, we find a time average ion heat flux that indicates nonlinear "stability" of ITG modes. In this case, the primary ITG instability leads to a secondary instability that generates a poloidal zonal flow and quenches the radial ion heat transport to $\langle Q_i \rangle \sim 10$ kW (see lower inset of Fig. 5.13). Increasing the ion temperature gradient by $\sim 3.5\%$ to $\omega_{T_i} \simeq 2.9$ marks the onset of nonlinear instability of ITG modes. This indicates a strong Dimits shift [121], defined as the difference between the nonlinear and linear critical temperature gradients for onset of turbulent transport. Further increasing the ion temperature gradient leads to approximately linear increases in the electron and ion heat fluxes. These heat fluxes are carried by radially

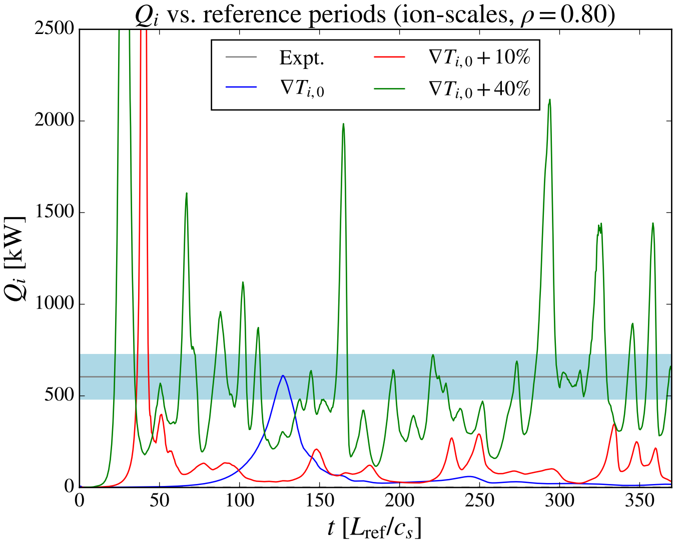

Figure 5.12: Time-traces of the ion heat flux for nonlinear ion-scale simulations with ITG nominal (*blue*), ITG+10% (*red*) and ITG+40% (*green*). The experimentally measured heat flux (*grey horizontal line*) and its uncertainty of ±20% (*blue shaded region*) are also shown. The average heat fluxes of the simulation are shown in Fig. 5.13 below.

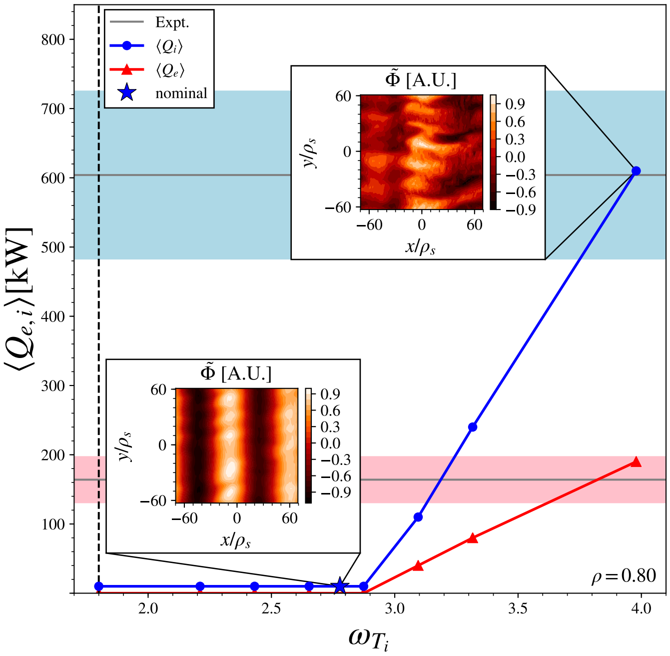

Figure 5.13: Nonlinear ion-scale simulations with a clear Dimits shift. The vertical black dashed line marks the linear critical ion temperature gradient $(\omega_{T_i})_{\text{crit}} = 1.80$. A strong poloidal zonal flow is found at nominal parameters (*lower inset*) and large-scale turbulence is found in the form of radially-elongated streamers at higher gradients (*upper inset*). The uncertainty in the experimental heat fluxes is ±20% (*shaded regions*). Increasing the ITG by $\sim 40\%$ recovers the experimentally inferred heat fluxes of *both* the ions and electrons.

elongated turbulent structures (streamers) at the ion scales [118, 122] (see upper inset of Fig. 5.13). This behavior is typical of plasmas in the core and has been used to infer the ion temperature gradient with gyrokinetic simulations [123].

With the ion temperature gradient increased by 40% (ITG+40%), our simulations recover the experimentally inferred heat fluxes for, remarkably, both the ion and electron heat channels. This ITG+40% scenario is consistent with the uncertainty of the ion temperature data at the 1.6σ level, where for brevity $\sigma = \sigma_{\text{stat}} + \sigma_{\text{sys}}$ (see Section 5.4). Specifically, the simulations give $\langle Q_i \rangle = 610$ kW and $\langle Q_e \rangle = 190$ kW, while the experimental values obtained with the ONETWO transport code are $\langle Q_i \rangle = (600 \pm 120)$ kW and $\langle Q_e \rangle = (164 \pm 33)$ kW (see Fig. 5.13).

5.6.3 Nonlinear Electron-scale Simulations

The nonlinear electron-scale simulations are performed with resolution

$$(n_x, n_y, n_z, n_{v_\parallel}, n_\mu) = (64, 512, 16, 32, 9) \tag{5.17}$$

and perpendicular box size $(L_x, L_y) = (9\rho_s, 9\rho_s)$. Note that the box size is smaller relative to the ion-scale simulations because the electron-scale domain is defined by linear simulations as $0.70 \leq k_y\rho_s \leq 180$. While finite Larmor radius (FLR) effects for $k_y\rho_s \gtrsim 60$ can be expected to significantly damp ETG modes, note that these high-k modes are mapped to smaller physical wavenumbers by geometric effects (encapsulated in the metric tensor). Thus, high-k modes can contribute meaningfully to the turbulent drive and it is advisable to extend the nonlinear electron-scale simulation domain over the entire wavenumber range of linearly unstable TEM/ETG modes. Note that for our electron-scale simulations we include fully kinetic ions (rather than only adiabatic ions).

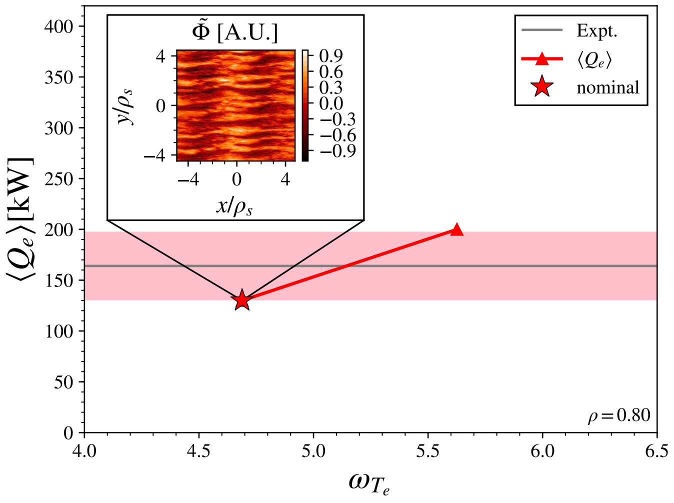

Figure 5.14: Dependence of the electron heat flux on the electron temperature gradient for nonlinear electron-scale simulations. Experimentally relevant heat transport could be carried at relatively large wavenumbers ($k_y\rho_s \sim 8$) by streamers (*inset*), which motivates multi-scale simulations.

For the nominal experimental input parameters we find a time average electron heat flux of $\langle Q_e \rangle = 130$ kW. Increasing the electron temperature gradient, which is the main driver of the electron heat flux, by its experimental error of $\sim 20\%$, we get a flux of $\langle Q_e \rangle = 200$ kW. This heat flux is within the experimentally inferred range of electron heat flux values obtained with the ONETWO transport code, namely $\langle Q_e \rangle = 164 \pm 33$ kW (see Fig. 5.14). This suggests that electron-scale heat transport could contribute to the overall heat transport, which will need to be studied with multi-scale simulations. Physically, we find that the electron heat flux is carried by radially elongated structures called streamers [124]. These structures are well-defined in a contour plot of electrostatic potential fluctuations, $\tilde{\Phi}(x, y)$ (see inset in Fig. 5.14).

5.6.4 Multi-scale Simulations

Linear and nonlinear simulations have indicated that multi-scale interactions could be present. We have therefore carried out the first nonlinear gyrokinetic multi-scale simulations using a realistic mass ratio and experimental input parameters in the near-edge, at $\rho = 0.80$. These used on the order of 23 k processors and 10 MCPUh on NERSC supercomputers.

Resolving the full ion and electron scales is computationally prohibitive (for the full extent of the electron and ion scales, see section 5.6.1). We therefore conducted a series of single-scale simulations with a sequentially reduced box size. This was done to identify an affordable domain that still resolves the main physical behavior of the plasma. For example, at the ion scales, we found that we could increase $k_{y,\min}\rho_s = 0.05 \rightarrow 0.15$ while maintaining the nonlinear heat flux to an accuracy of $\sim 10\%$. In the type of plot shown below (see Fig. 5.15), adapted from Görler and Jenko [49–52], the area under the curve roughly corresponds to the total heat flux carried at the corresponding wavenumbers. Similarly, at the electron scales, we were able to reduce $k_{y,\max}\rho_s = 180 \rightarrow 40$ with GyroLES techniques while maintaining a similar level of accuracy ($\sim 15\%$) in the heat flux carried at the electron scales (see Fig. 5.16). This is significantly aided by the fact that most of the heat advection at the electron scales is carried by modes with $k_y\rho_s \approx 7$. The flux-spectrum at the electron scales is plotted as the red dotted line in Fig.'s 5.16 and 5.17. It is evident that, while the maximum growth rate in the linear flux spectrum is located at $k_y\rho_s \approx 50$ (see Fig. 5.7), the

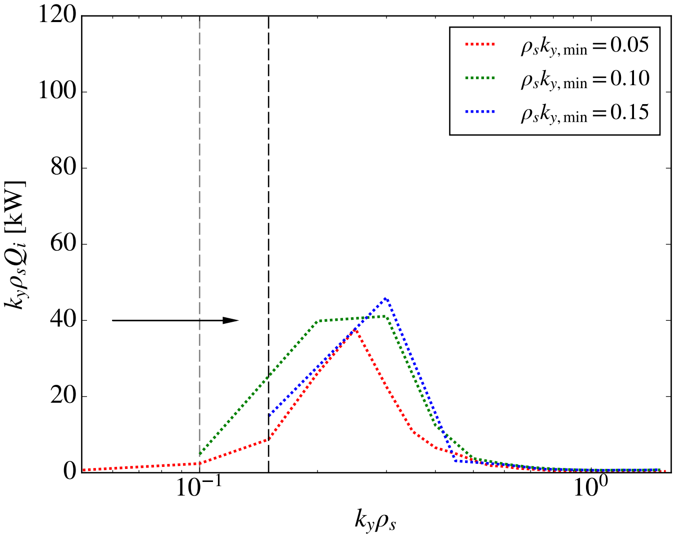

Figure 5.15: Flux spectra from nonlinear ion-scale simulations at $\rho = 0.80$ with ITG+10% and varying box size in binormal direction. In this type of plot, adapted from Görler and Jenko [49–52], the heat flux carried by a range of wavenumbers is proportional to the area under the curves. This figure illustrates that a careful reduction in box size, corresponding to an increase in minimum resolved wavenumber $\rho_s k_{y,\min} = 0.05 \to 0.15$, continues to capture the heat flux carried at the ion scales.

nonlinear heat flux is carried predominantly by streamers associated with ETG modes with wavenumbers in the vicinity of $k_y \rho_s \approx 7$. This facilitates the above reduction in the resolved electron scales in the preparation for multi-scale simulations. At the ion scales, the heat flux is carried predominantly by modes with $k_y \rho_s > 0.15$. We thus resolve both the electron and ion scales in a carefully selected domain of poloidal wavenumbers of $0.15 \leq k_y \rho_s \leq 40$ (see Fig. 5.17). Note that these nonlinear scans in simulation domain, while themselves computationally intensive, reduced the resource intensity of multi-scale simulations by a factor of $\gtrsim 10$, bringing them into the realm of the possible.

The nonlinear multi-scale simulations are performed with grid points

$$(n_x, n_y, n_z, n_{v_\parallel}, n_\mu) = (512, 512, 16, 32, 18) \tag{5.18}$$

and perpendicular box size $(L_x, L_y) = (75\rho_s, 42\rho_s)$. These simulations give the following qualitative results. First, we find that ETG-scale streamers co-exist with a zonal flow at ion scales when ITG modes are stable at nominal ω_{T_i} (see Fig. 5.18). Second, we find that ETG-

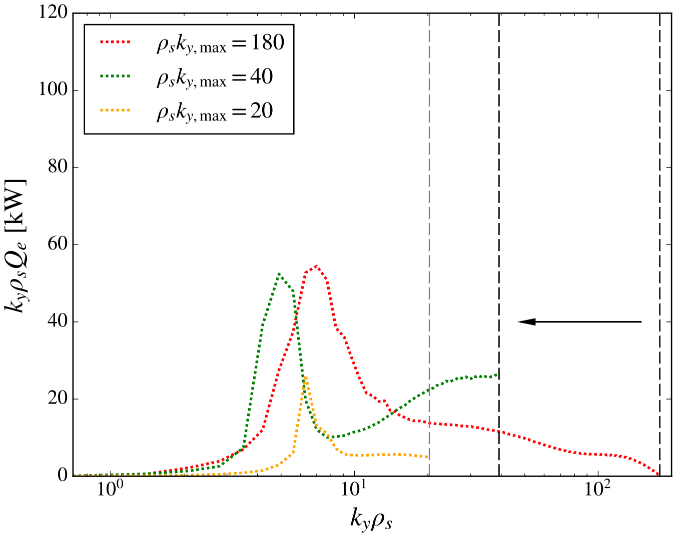

Figure 5.16: Flux spectra from nonlinear electron-scale simulations at $\rho = 0.80$ with varying box size in binormal direction. This figure illustrates that a careful reduction in maximum resolved wavenumber $\rho_s k_{y,\max} = 180 \rightarrow 40$ continues to capture the heat flux carried at the electron scales (particularly around $k_y \rho_s \sim 7$). There is a moderate increase in the heat flux carried at the high wavenumbers ($k_y \rho_s > 20$), which is due to the unresolved dissipation at ($k_y \rho_s > 40$) but within acceptable limits. A further reduction $\rho_s k_{y,\max} = 180 \rightarrow 20$ would not yield a physical result.

scale streamers are strongly sheared apart by ITG modes in the ITG+40% scenario (see Fig. 5.17 and Fig. 5.19). Therefore, electron-scale transport does not contribute significantly to the total transport when ITG modes are highly unstable, such as when ITG+40%. Thus, the heat-flux-matching single-scale simulation in Fig. 5.13 is representative of the multi-scale heat flux.

In summary, simulations at $\rho = 0.80$ reproduce both the experimental ion and electron heat fluxes consistent with the combined statistical and systematic uncertainty of the CER data at the 1.6σ level. Multi-scale simulations suggest that turbulent structures on the ion scales strongly disrupt the streamers found on the electron scales.

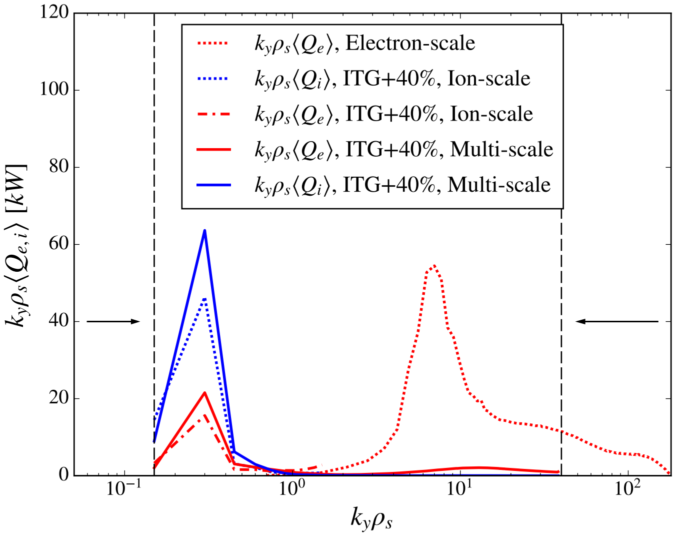

Figure 5.17: Nonlinear flux spectrum of multi-scale simulations (with simulation domain bounded by the dashed lines) and single-scale simulations. The area under the curves is proportional to the total heat flux carried at low- and high-k [50,51]. Multi-scale simulations with ITG modes driven unstable by an increase in ITG by 40% show that electron-scale heat flux via streamers is greatly reduced by large turbulent structures at the ion scales (see upper inset in Fig. 5.13).

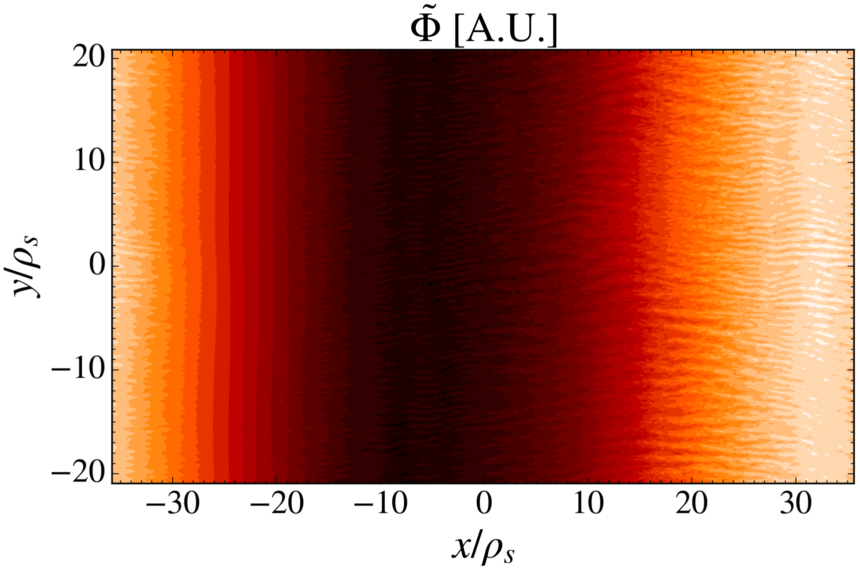

Figure 5.18: Contour of fluctuations in $\tilde{\Phi}(x, y)$ for multi-scale simulations at $\rho = 0.80$ and nominal ion temperature gradient. The ITG modes are nonlinearly quenched by a strong poloidal zonal flow. ETG-scale streamers are found to co-exist with this large ion-scale zonal flow.

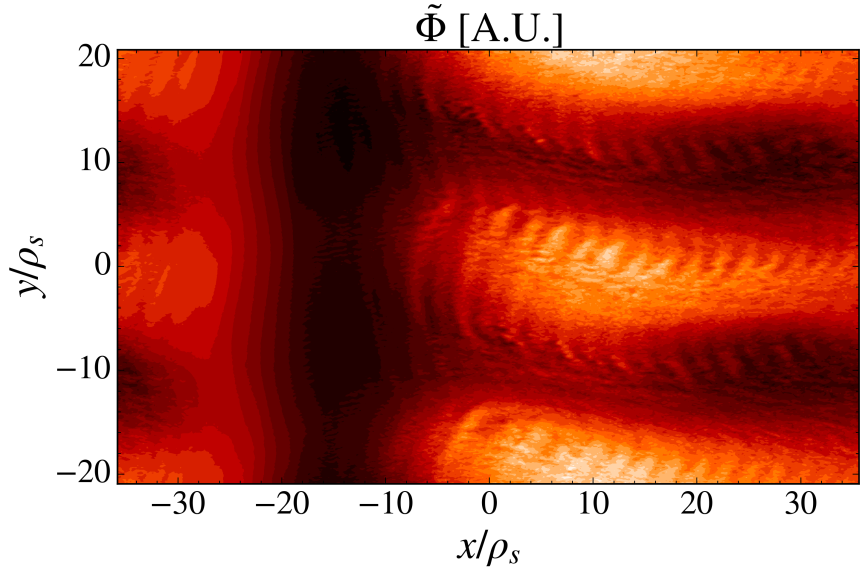

Figure 5.19: Contour of fluctuations in $\tilde{\Phi}(x, y)$ for multi-scale simulations at $\rho = 0.80$ and ITG+40%. The large structures on the order of $12\rho_s$ are associated with ITG modes and shear apart electron-scale streamers, which have a vertical width on the order of $\lesssim 1\rho_s$.

5.6.5 Sensitivity Study

In this subsection we describe a dedicated linear sensitivity study at $\rho = 0.80$, which is carried out by simultaneously changing several input parameters close to their measured uncertainty range. The purpose of this sensitivity study is to explore whether a flux-matching result might also be obtained without varying only ω_{T_i}, but also other gradient quantities. It may be possible to vary several parameters over smaller uncertainty ranges than the 1.6σ variation of ω_{T_i}. However, we find that ω_{T_i} is the most suitable parameter to vary due to the large uncertainty of CER data and the strong physical effect of ω_{T_i} on the turbulence.

By their very nature, linear simulations do not capture nonlinear saturation of fluxes and instead calculate fluxes that grow exponentially in time. However, the *ratio* of ion and electron fluxes at every time-step and mode number remains constant due to their equal growth rates. Comparing the ratios of electron and ion heat transport at the same time-step of linear simulations for various input parameters provides a useful prediction of the flux ratio found in nonlinear simulations. This quasi-linear study could guide us to a parameter set that, if used as input for a nonlinear simulation, could give not only the experimental ratio but also the experimental values of the ion and electron heat fluxes.

The linear simulations for this study are performed at a constant point in wavenumber space of $k_y\rho_s = 0.20$. This point was chosen, as it is in proximity of the peak in the ion-scale energy flux spectrum of nonlinear simulations (see Fig. 5.20). We concentrate on the dominant mode to maximize the predictive power of this study.

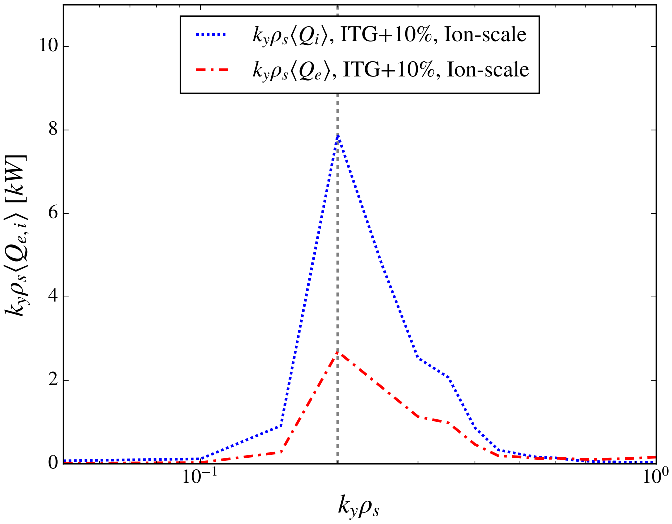

Figure 5.20: Flux spectrum at $\rho = 0.80$ with ITG+10%. For the nonlinear simulations the flux spectrum peaks at $k_y\rho_s = 0.20$ (*vertical dashes*), which serves as the wavenumber used for a linear sensitivity study (see Fig. 5.21).

We seek to recover the experimental ratio of $Q_i/Q_e = 3.68 \pm 0.74$. Physically, the ratio of ion to electron heat fluxes depends primarily on logarithmic gradients ω_X, but can also depend on the temperature ratio T_i/T_e. Results of the input parameter scan are summarized in Fig. 5.21. The flux ratio Q_i/Q_e is plotted as a function of two variables, with the temperature ratio on the x-axis and the variables ω_X on the y-axes. We find that (i) the flux ratio depends mostly on the ion and electron temperature gradients, as expected; (ii) the density gradient has a comparably weak effect; (iii) the temperature ratio has a negligible effect. We thus neglect the effect of the temperature ratio and consider only the effects of the gradient parameters. To quantify this sensitivity, we carry out a Taylor expansion of

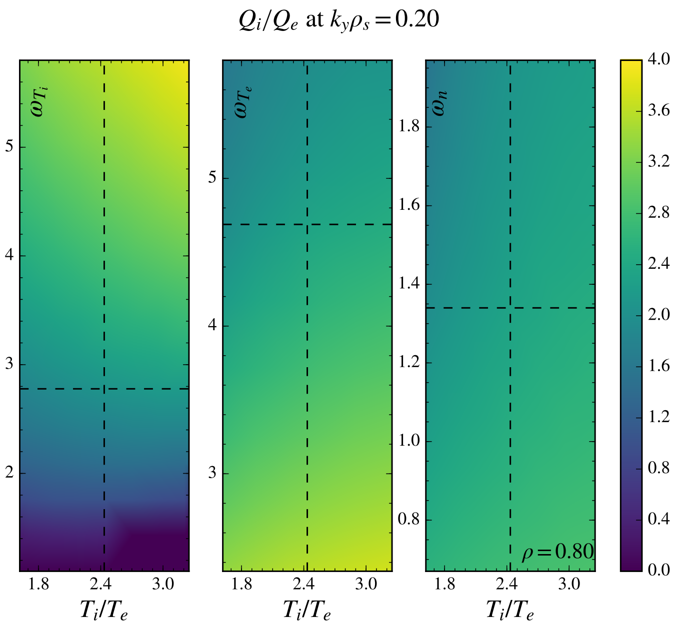

Figure 5.21: Variation of the flux ratio (Q_i/Q_e) with logarithmic gradients ω_{T_i}, ω_{T_e}, ω_n and the temperature ratio T_i/T_e. For reference, the experimental flux ratio is $Q_i/Q_e = 3.68 \pm 0.74$. The dashed lines indicate the nominal values of these parameters. We find a strong dependence of the flux ratio on ω_{T_i} and ω_{T_e}, and a weak dependence on ω_n and T_i/T_e.

Q_i/Q_e with respect to the logarithmic gradients ω_X, giving

$$Q_i/Q_e \approx Q_{i,0}/Q_{e,0} + \sum_X \frac{\partial(Q_i/Q_e)}{\partial\omega_X}\bigg|_{\omega_{X,0}} \delta\omega_X \; , \tag{5.19}$$

where X is a variable identifying the nature of the gradient scale lengths, $X \in \{T_i, T_e, n\}$, and the subscript 0 identifies the results for nominal experimental input parameters (e.g. $Q_{i,0}/Q_{e,0} = 2.1$ is the flux ratio for nominal input parameters). The linear scans quantify the gradient terms in the Taylor expansion, which are summarized in the second column of Table 5.2. Using equation (5.19), we choose the $\delta\omega_X$ values such that the value of Q_i/Q_e

X	$\partial(Q_i/Q_e)/\partial\omega_X$	$\delta\omega_X$	$\omega_{X,0}$	$\delta\omega_X/\omega_{X,0}$	$\omega_{X,0} + \delta\omega_X$
T_i	**0.74**	**0.31**	2.78	+11%	3.09
T_e	**−0.41**	**−1.88**	4.69	−40%	2.81
n	**−0.35**	**−0.54**	1.34	−40%	0.80

Table 5.2: Quasi-linear Model: Taking only linear terms in a Taylor expansion, we get $Q_i/Q_e = 3.26$ for the above values of $\delta\omega_X$.

is close to the experimentally inferred value of $Q_i/Q_e = 3.68 \pm 0.74$. With changes $\delta\omega_X$ as shown in the third column in Table 5.2, our quasi-linear study predicts $Q_i/Q_e = 3.26$ for a nonlinear simulation. To truly quantify the turbulent heat transport and to test this prediction, nonlinear simulations are necessary.

The nonlinear simulation with the multiple-parameter variations give $\langle Q_i \rangle = 100$ kW and $\langle Q_e \rangle = 30$ kW. Therefore, the ratio of ion and electron heat fluxes is correctly predicted by the quasi-linear study ($\langle Q_i \rangle / \langle Q_e \rangle = 3.33$). However, in practice this ratio was obtained by a reduction in the electron heat transport rather than an increase in ion heat transport. This confirms that ITG is the dominant driver of ion-scale heat flux and supports our method of varying only the ion temperature gradient.

5.7 Simulation Results at second radial position ($\rho = 0.90$)

We now direct our attention further outwards to the near-edge region at $\rho = 0.90$. We first carry out linear simulations to identify the linear mode spectrum, which is dominated by TEM/ETG turbulence. Subsequent nonlinear simulations show high sensitivity of the total heat flux to changes in the electron temperature gradient. This could be due to a hybrid ITG/TEM scenario that was not predicted by linear simulations. With the inclusion of $\boldsymbol{E}\times\boldsymbol{B}$ shear and an increase in the electron temperature gradient by 23%, which is consistent with the experimental temperature data at the 1.3σ level, we are able to match the heat flux of the experiment. These results validate our gyrokinetic method and help push the gyrokinetic validation frontier closer to the edge region.

5.7.1 Linear Simulations

Linear simulations indicate that the main turbulent drive is carried by TEM/ETG modes at $\rho = 0.90$ (see Fig.'s 5.22 and 5.23). Note that this can be explained by the increased density gradient driving TEM turbulence closer to the plasma edge (see Fig. 5.3). Figure 5.23 shows the turbulent modes in low-wavenumber domain, which is most interesting for nonlinear simulations because the turbulent advection is most efficient at these large scales. To

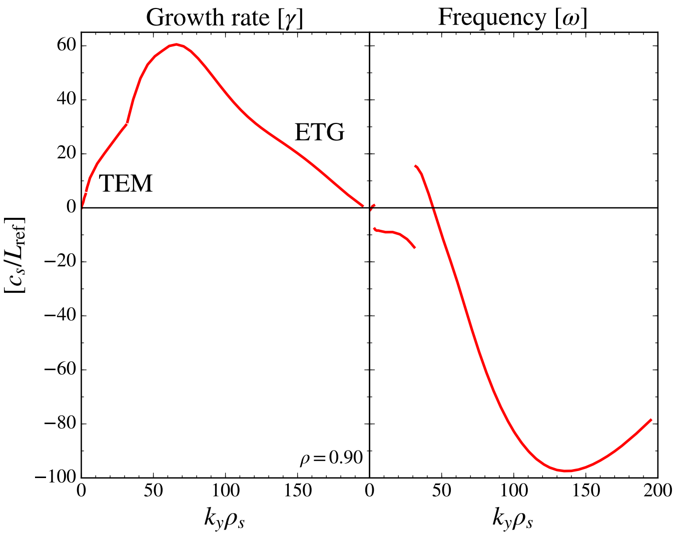

Figure 5.22: Linear growth rates and frequencies at $\rho = 0.90$ on linear axes for nominal input parameters. We expect trapped electron modes (TEMs) at low-k and ETG modes at high-k.

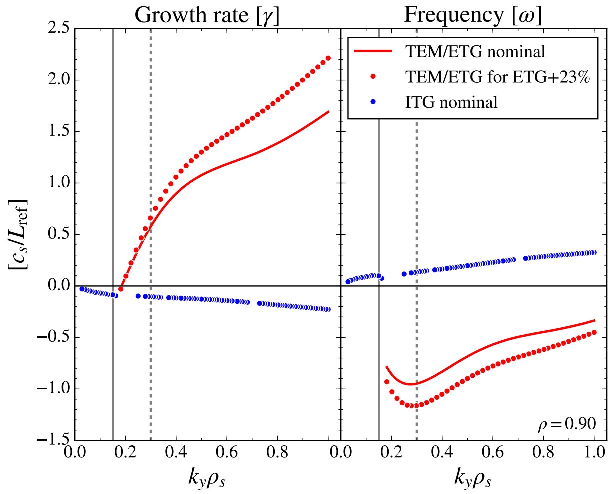

Figure 5.23: Linear growth rates and frequencies of TEM/ETG modes for nominal parameters (*red line*) and with ETG increased by 23% (*red circles*). We also find subdominant and stable ITG modes (*blue circles*). For comparison with nonlinear results below, the vertical lines highlight the position of the $k_y\rho_s = 0.15$ mode (*solid*) and the $k_y\rho_s = 0.30$ mode (*dashed*).

identify the subdominant modes that can play a role in nonlinear simulations, we employ the eigenvalue solver in GENE. Curiously, the subdominant mode is an ITG-type mode that is stable over all considered wavenumbers, which can be seen by its negative growth rates (see Fig. 5.23). Moreover, we find that an increase in electron temperature gradient by

23% further destabilizes the TEM/ETG modes. These linear simulations indicate that the TEM/ETG modes are likely to dominate in nonlinear simulations, with negligible effect of ITG modes.

At $\rho = 0.90$, the Carbon impurity has a small effect on the linear growth rates compared to the pure Deuterium plasma (see Figure 5.24). Therefore, to reduce computational complexity by approximately 30%, we will carry out nonlinear simulations at $\rho = 0.90$ with two rather than three particle species.

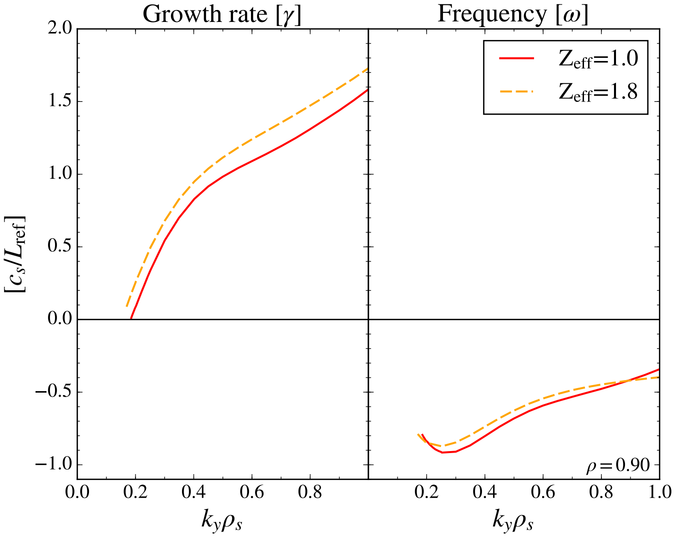

Figure 5.24: Linear growth rates and frequencies for a pure Deuterium plasma (*red*) and for a plasma with $Z_{\mathrm{eff}} = 1.8$ due to a Carbon impurity species (*orange*). The effect of Carbon impurities on growth rates is small and will be neglected in nonlinear simulations.

When carrying out nonlinear simulations, it may sometimes be necessary to vary experimental parameters close to their experimental uncertainty in order to reproduce the experimental heat flux (see simulations at $\rho = 0.80$). Therefore, it is useful to identify the sensitivity of the linear growth rates to various changes in experimental parameters. For example, in Figure 5.25 we study the sensitivity of the dominant TEM/ETG branch with respect to changes in the density and electron temperature. We find that there is limited sensitivity to changes in the density or *increases* in electron temperature, while there is some sensitivity to *decreases* in electron temperature. This may be due to the higher collisionality of electrons at lower temperatures and the sensitivity of TEM to collisions, which tend to

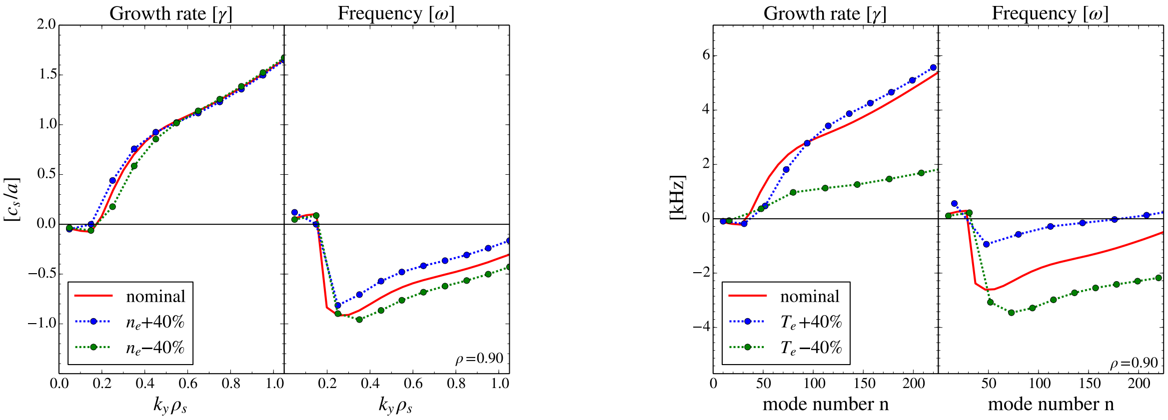

(a) Dependence on density.

(b) Dependence on temperature.

Figure 5.25: Sensitivity study of linear growth rates and frequencies at $\rho = 0.90$. Growth rates and frequencies are shown to have limited susceptibility to changes in density and temperature. Note that the growth rates are plotted as a function of mode number in Figure b). This is due to the dependence of the normalization parameters on T_e (recall that $\rho_s = c_s/\Omega_i$ and $c_s = \sqrt{T_e/m_i}$).

de-trap electrons and therefore weaken the TEM growth rates. This further underscores the TEM character of the dominant linear modes.

Moreover, in Figure 5.26 we investigate the sensitivity of linear growth rates to changes in the gradient parameters such as the density gradient, and the ion temperature gradient (in addition to the electron temperature gradient studied previously). We find relatively little sensitivity of the growth rates to changes in the density gradient and ion temperature gradient when compared to similarly-sized changes in the electron temperature gradient. This further helps identify the electron temperature gradient as the most likely drive of nonlinear turbulence.

In order to further test the sensitivity of nonlinear turbulence to *simultaneous* changes in the electron temperature gradient and the density gradient, we perform a linear sensitivity study at the wavenumber that ultimately carries most of the nonlinear heat transport, $k_y\rho =$ 0.20, as will be shown below (see Fig. 5.40). We simultaneously vary the electron temperature gradient and the density gradient and plot the corresponding contour of the growth rates in Figure 5.27. The growth rate is much more sensitive to the electron temperature gradient, so this forms the key parameter for nonlinear simulations.

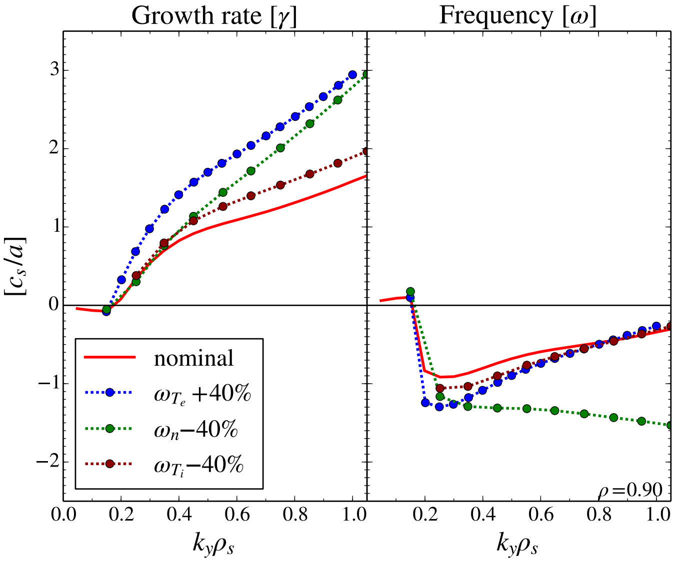

Figure 5.26: Sensitivity of growth rates and frequencies to changes in density and temperature gradients at $\rho = 0.90$. Linear growth rates are most sensitive to changes in the electron temperature gradient. Therefore ω_{T_e} is chosen as free parameter for nonlinear simulations.

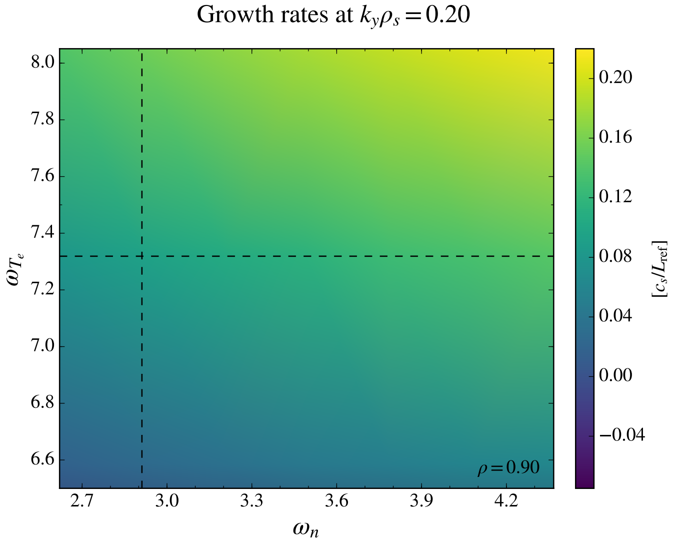

Figure 5.27: Linear growth rates as a function of logarithmic gradients ω_{T_e} and ω_n. This study was carried out for poloidal wavenumber $k_y\rho_s = 0.20$, where a large fraction of the nonlinear heat flux is carried at $\rho = 0.90$. The dashed lines indicate the nominal values of these parameters. The growth rates depend less on ω_n than on ω_{T_e}, identifying the latter as a key parameter for nonlinear simulations.

5.7.2 Nonlinear Simulations at Ion Scales

Our linear simulations have shown that the growth rates at $\rho = 0.90$ are sensitive to changes in ω_{T_e} (see Fig. 5.23). This is due to the predominance of TEM/ETG-type modes with ITG modes subdominant and stable at nominal gradients. We thus study the sensitivity of nonlinear simulations to changes in ω_{T_e}.

The nonlinear ion-scale simulations are performed with resolution $(n_x, n_y, n_z, n_{v_\parallel}, n_\mu) = (512, 64, 32, 32, 18)$ and perpendicular box size $(L_x, L_y) = (188\rho_s, 126\rho_s)$. Note that convergence tests found that a higher resolution was required for the ion scales at $\rho = 0.90$ than at $\rho = 0.80$. Physically, this is due to the need to resolve higher magnetic shear here (see Table 5.1). Moreover, the radial box size was increased because the simulated plasma was more susceptible to simulation boundary effects at $\rho = 0.90$ than at $\rho = 0.80$.

We define the ion-scale domain as $0.05 \leq k_y\rho_s \leq 1.60$ and employ GyroLES techniques to avoid the unphysical build-up of free energy at $k_y\rho_s \simeq 1.60$. The individual ion and electron heat channels are difficult to distinguish experimentally with current techniques due to the high collisionality at $\rho = 0.90$, so that the observable here is the *total* heat flux.

Nonlinear simulations with an increase in ETG by up to $\sim 30\%$ were performed. Without the inclusion of experimental $\boldsymbol{E} \times \boldsymbol{B}$ shear, we found a saturated time-average flux of up to $\langle Q_{\mathrm{tot}} \rangle = 5$ MW (see Fig. 5.28).

Interestingly, we see high sensitivity to increases in ETG between the +22% and +23% mark. Figure 5.29 shows a contour plot of electrostatic potential fluctuations with high (but "healthy") levels of turbulence at large scales for the +23% scenario without $\boldsymbol{E} \times \boldsymbol{B}$ shear. The observations persisted with an increase in the radial box size (see Fig. 5.30) and an independent numerical test of the validity of GyroLES techniques (see Fig. 5.31). This indicates that there may be a physical origin for this high sensitivity of the heat flux to changes in ETG.

The following analysis shows that TEM turbulence may nonlinearly destabilize the linearly stable ITG modes, leading to a hybrid ITG/TEM scenario in our nonlinear simulations. Recall that the ITG modes are *stable* for all wavenumbers (see Fig. 5.23). Moreover,

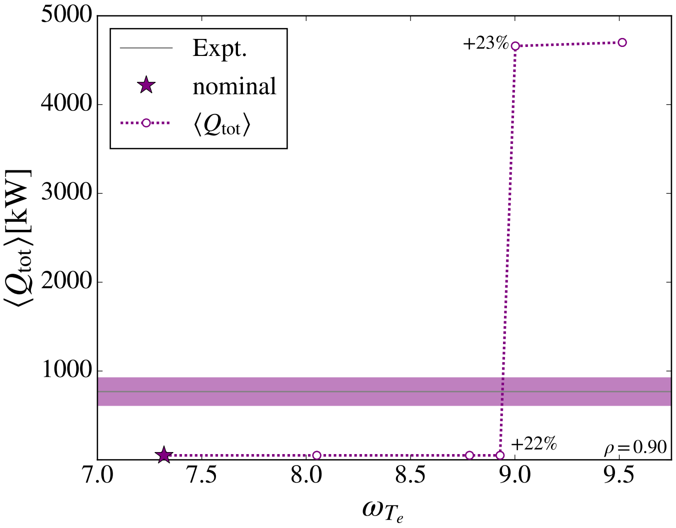

Figure 5.28: Total heat flux as a function of electron temperature gradient in nonlinear simulations at $\rho = 0.90$. Small changes in gradient from +22% to +23% show large changes in the heat flux. This sensitivity to the electron temperature gradient is investigated in the following figures, which suggest that TEM turbulence may nonlinearly excite the linearly stable ITG turbulence and create a hybrid ITG/TEM scenario.

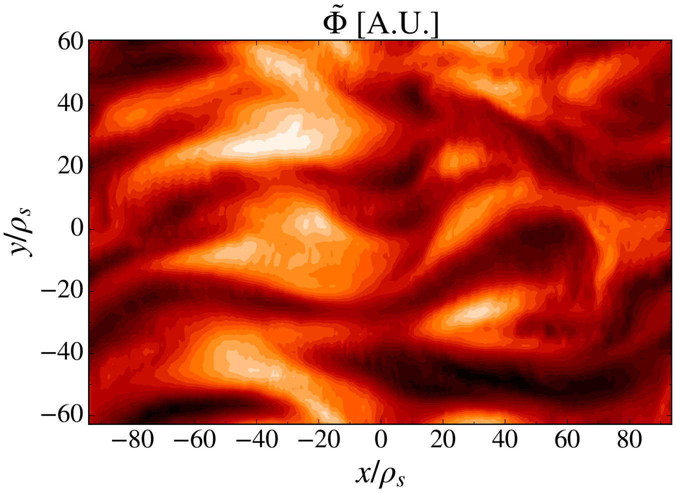

Figure 5.29: Contour plot of $\tilde{\Phi}$ at $\rho = 0.90$ with ETG+23%. The ion-scale structures show high (but "healthy") levels of turbulence.

the ETG/TEM branch with ETG increased by 23% (ETG+23%) is linearly unstable for $k_y\rho_s > 0.18$. Based on these observations, we expected nonlinear simulations to show that the majority of the heat flux is carried by electrons in the vicinity of $k_y\rho_s \sim 0.30$. However, the heat-flux spectrum of nonlinear simulations with ETG+23% shows that the majority of the heat flux is carried by ions in the vicinity of $k_y\rho_s \sim 0.15$ (see Fig. 5.32). This indicates

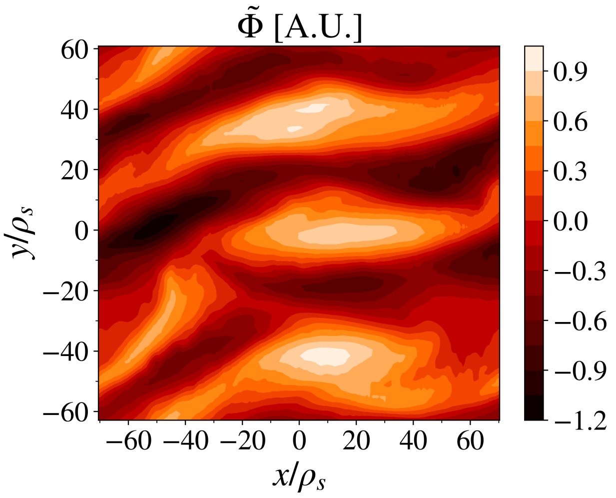

(a) Too small radial box.

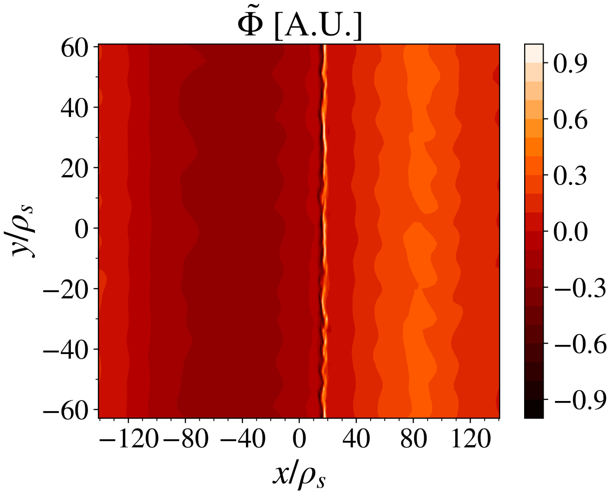

(b) Insufficient radial resolution.

Figure 5.30: Illustration of possible numerical errors. Figure a) shows a diagonal end-to-end connection of turbulent structures for a simulation box that *a posteriori* is too small, namely box size $(L_x, L_y) = (141\rho_s, 126\rho_s)$ and $(n_x, n_y, n_z, n_{v_\parallel}, n_\mu) = (512, 32, 32, 32, 18)$, which can also be identified by an unphysical spike in the heat flux by a factor of three in a short time period. Figure b) shows an example of a simulation that has *a posteriori* insufficient radial resolution, namely box size to $(L_x, L_y) = (282\rho_s, 126\rho_s)$ with grid points as in Figure a), which causes a build-up of energy at the lowest resolved scales. The optimal configuration is found to have grid points as in Figure a) with a 33% larger box size, namely $(L_x, L_y) = (188\rho_s, 126\rho_s)$.

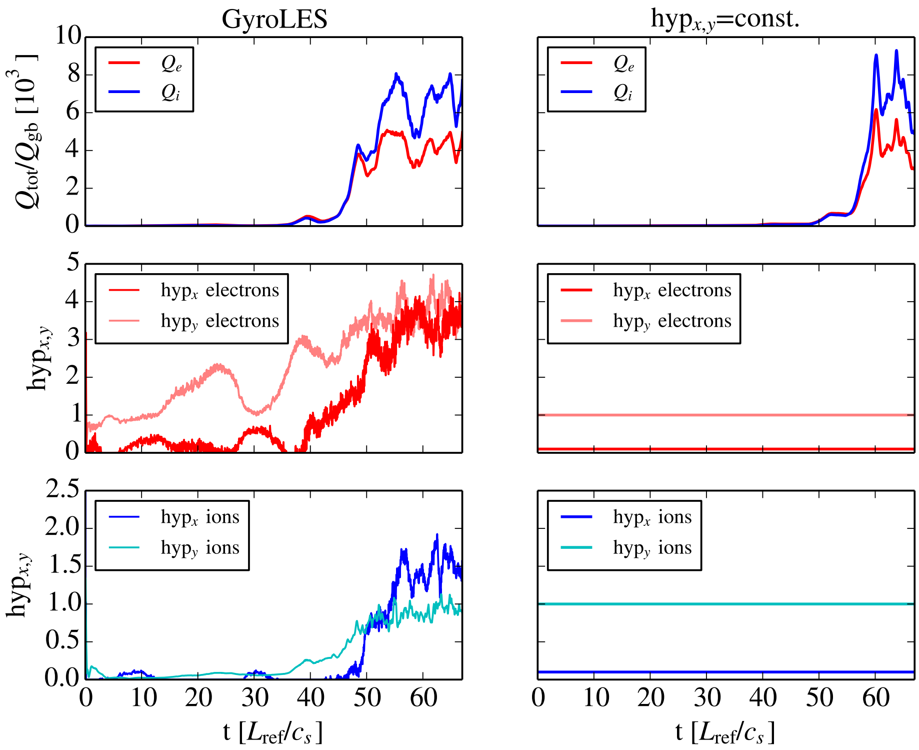

Figure 5.31: Test of GyroLES techniques at $\rho = 0.90$ with an electron temperature gradient +30% above nominal. The left column shows the time trace of the heat flux and the hyper-diffusion values chosen by the GyroLES tool. The right column shows that keeping the hyper-diffusion values constant (*bottom two rows*) gives a qualitatively similar heat flux time trace that saturates at a value comparable to the simulations with GyroLES (*top row*). This highlights the robustness of the GyroLES technique and, together with the results of Figure 5.30, suggests that the sensitivity of the heat flux to changes in ω_{T_e} is likely not caused by numerical issues.

high ITG mode activity, which was not predicted by linear simulations. To test the suspected ITG-dependence of the heat flux, we reduced the ion temperature gradient by 100% and uncovered the purely TEM/ETG turbulence with electron-dominated heat flux carried predominantly at $k_y\rho_s \sim 0.30$ as originally expected (see Fig. 5.32 and 5.33).

To further identify the nature of nonlinear turbulence at $\rho = 0.90$, we have plotted the frequency spectrum of electrostatic potential fluctuations (see Fig. 5.34). We find that the modes that carry most of the heat flux (i.e. $k_y\rho_s \sim 0.15$) have positive frequency and therefore are associated with ITG turbulence. Moreover, when the ITG is reduced by 100%, the nonlinear frequencies at $k_y\rho_s = 0.30$ are in good agreement with linear frequencies of the TEM/ETG branch as expected (see Fig. 5.35). This indicates that both TEM and

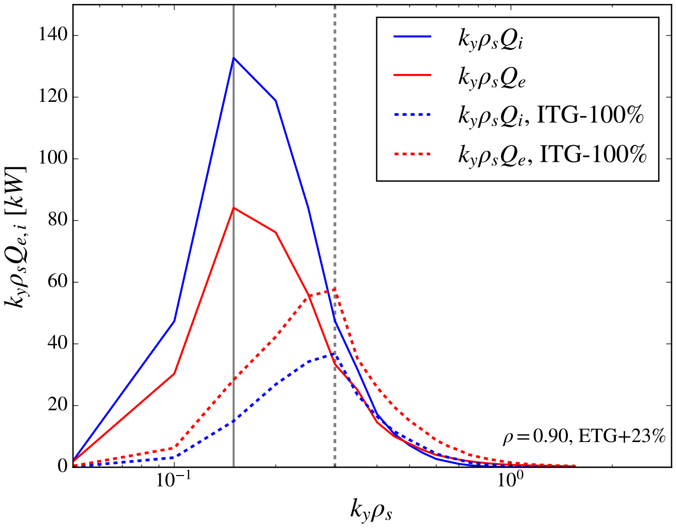

Figure 5.32: Heat-flux spectra of simulations with ETG increased by 23% (ETG+23%) and varying ITG. For nominal ITG, the majority of the heat flux is carried by the ions in the vicinity of $k_y \rho_s = 0.15$ (*solid line*), indicating high ITG mode activity. For ITG reduced by 100%, the majority of the heat flux is carried by the electrons in the vicinity of $k_y \rho_s = 0.30$ (*dashed line*), indicating high TEM activity as originally predicted by linear simulations.

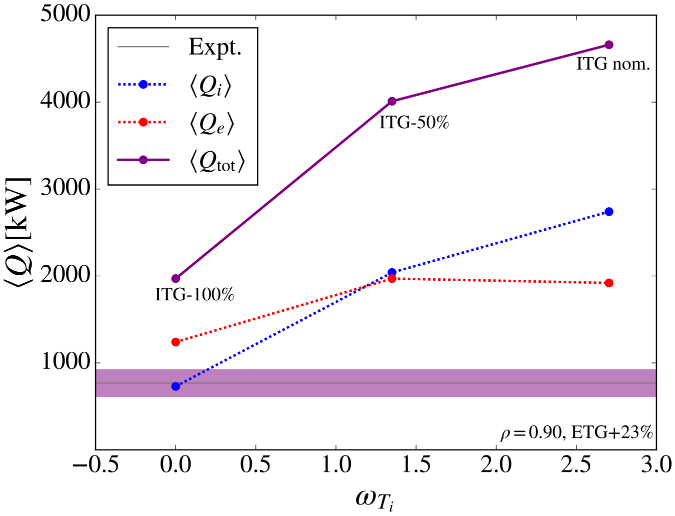

Figure 5.33: Sensitivity of the heat flux to changes in ITG when ETG+23% at $\rho = 0.90$. Reducing the ITG causes a large reduction in the ion heat flux, indicating that ITG modes are active and dominant for nominal ITG and ETG+23%. When the ITG is reduced to zero, the heat flux becomes electron dominated as originally predicted by linear simulations.

ITG turbulence are active in nonlinear simulations. This seems to suggest that there exists a hybrid ITG/TEM scenario with nominal ITG and ETG+23% (even though linear simulations did not predict this).

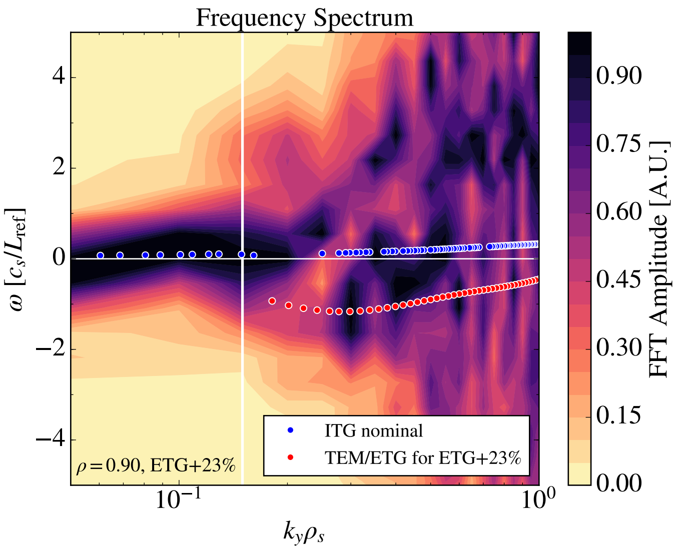

Figure 5.34: Frequencies of electrostatic potential fluctuations for the scenario with nominal ion temperature gradient and ETG+23%. The positive frequency of the nonlinear mode carrying most of the heat flux ($k_y\rho_s = 0.15$) indicates that ITG modes are nonlinearly unstable. This is unexpected from linear simulations, where ITG modes (*blue circles*) are linearly stable. This suggests that the TEM/ETG modes (*red circles*), which have their nonlinear turbulence onset at ETG+23%, may be driving the ITG modes nonlinearly unstable, contributing to the high heat-flux-stiffness seen in Fig. 5.28.

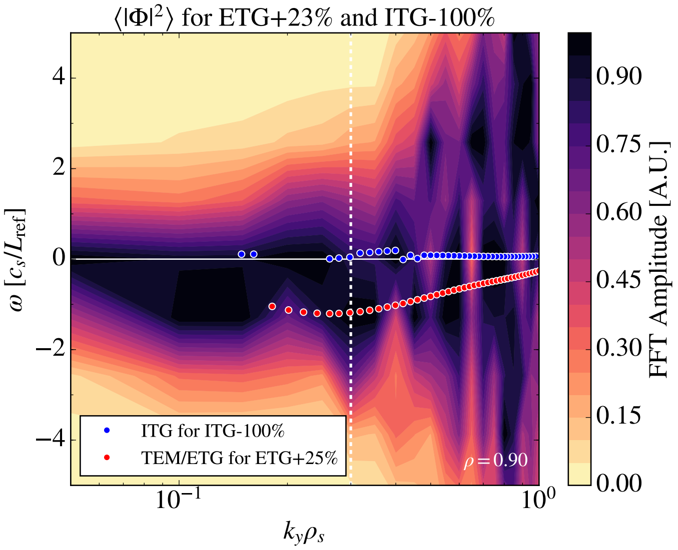

Figure 5.35: Frequencies of electrostatic potential fluctuations for the scenario with ETG+23% and zero ITG, i.e. ITG-100%. The negative frequency of the nonlinear mode carrying most of the heat flux ($k_y\rho_s = 0.30$) is consistent with linear TEM/ETG frequencies (*red circles*) rather than the ITG frequencies (*blue circles*).

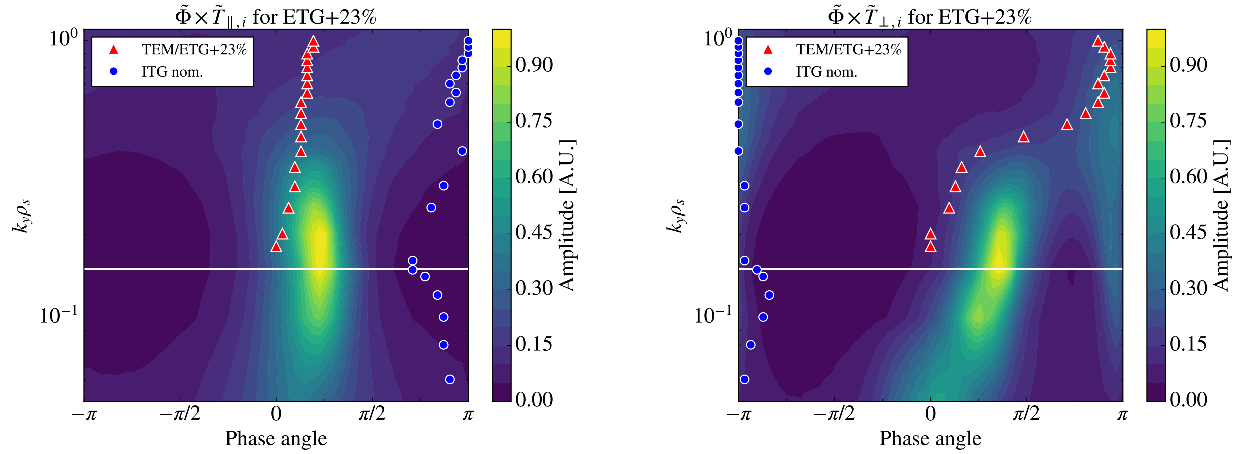

(a) Parallel ion temperature fluctuations

(b) Perpendicular ion temperature fluctuations

Figure 5.36: Cross-phases of ion temperature fluctuations and electrostatic potential fluctuations for the scenario with nominal ITG and ETG+23%. General agreement is found between the nonlinear cross-phases and the linear cross-phases for the TEM/ETG turbulence (*red triangles*) rather than the ITG turbulence (*blue circles*). This indicates the presence of TEM/ETG turbulence in the nonlinear simulations. Note that temperature and potential fluctuations are between zero and $\pi/2$ out of phase (with $\tilde{T}_{\perp,i}$ closer to $\pi/2$ out of phase). This could contribute to the high ion heat flux observed in the nonlinear simulations.

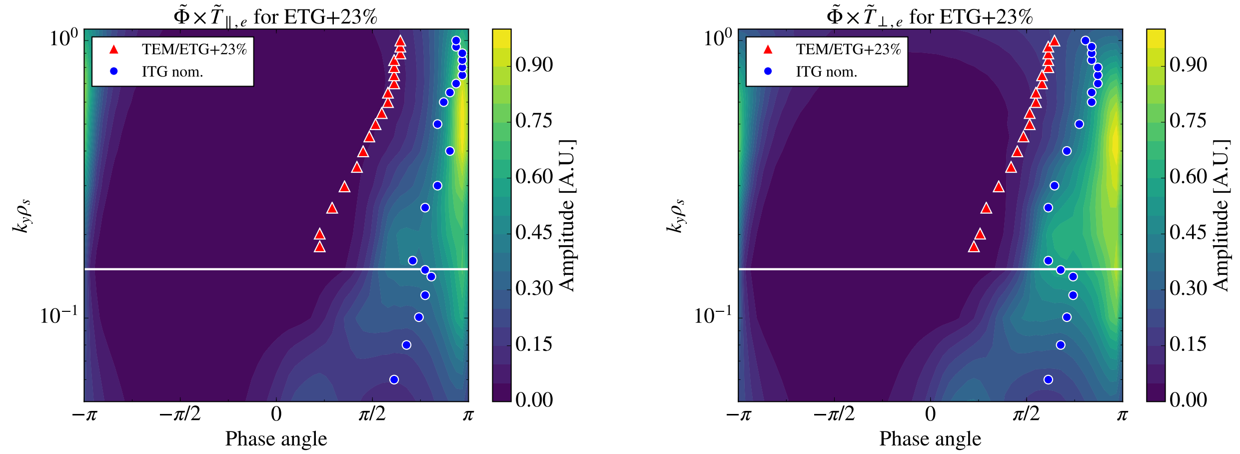

(a) Parallel electron temperature fluctuations

(b) Perpendicular electron temperature fluctuations

Figure 5.37: Cross-phases of electron temperature fluctuations and electrostatic potential fluctuations for the scenario with nominal ITG and ETG+23%. Agreement between linear and nonlinear cross-phases is generally better for the subdominant ITG mode (*blue circles*) than for the dominant TEM/ETG modes (*red triangles*). This is particularly true at wavenumbers responsible for heat transport, $k_y\rho_s \sim 0.15$ (*horizontal line*), which indicates a hybrid ITG/TEM scenario.

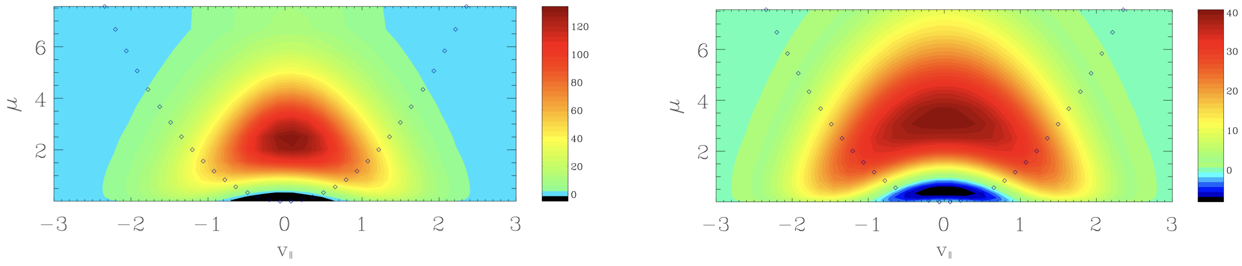

(a) Ion heat transport in velocity space

(b) Electron heat transport in velocity space

Figure 5.38: Electrostatic heat transport in velocity space for ETG+23% and ITG nominal (arbitrary units). The dotted line marks the trapped-passing particle boundary, where trapped particles have $\mu \gtrsim v_{\parallel}$. Figures a) and b) show that the heat transport of electrons and ions is dominated by perpendicular energy. Parallel energy transport, while weaker than the perpendicular energy transport, is relatively stronger for the electrons than for the ions.

We now study the cross-phases between fluctuations in the ion temperature $\tilde{T}_i$ and electrostatic potential $\tilde{\Phi}$ (see Fig. 5.36). We find that the nonlinear cross-phases are approximately in agreement with the linear cross-phases of the TEM/ETG modes. Moreover, the phase differences between the ion temperature and electrostatic potential fluctuations are between 0 and $\pi/2$. At wavenumbers relevant for electrostatic heat transport ($k_y \rho_s = 0.15$), the nonlinear cross-phases of $\tilde{T}_{\perp,i}$ and $\tilde{\Phi}$ are close to $\pi/2$, which is characteristic of high electrostatic heat transport (see Fig. 5.36). This suggests that heat transport mostly affects perpendicular energy and is therefore associated with trapped particles (see Fig. 5.38).

Similarly, we now study the cross-phases between fluctuations in the *electron* temperature $\tilde{T}_e$ and electrostatic potential $\tilde{\Phi}$ (see Fig. 5.37). For the wavenumbers carrying most of the heat flux, $k_y \rho_s \sim 0.15$, the nonlinear cross-phases generally agree with the linear cross-phases of the ITG modes. Moreover, at $k_y \rho_s \sim 0.15$, the nonlinear cross-phases are out of phase by approximately $\pi/2$, which is characteristic of significant electrostatic heat transport. For higher wavenumbers, the nonlinear cross-phases agree with the linear cross-phases of ITG modes rather than TEM/ETG modes. A similar hybrid ITG/TEM scenario was previously found in Ref. 107, with the difference that both the dominant TEM and subdominant ITG modes were linearly unstable. Our results indicate a hybrid ITG/TEM scenario, with linearly subdominant and stable ITG modes carrying most of the heat flux. This scenario could also be relevant to spherical tokamaks, where ITG modes are more often linearly stable than in conventional tokamaks due to the lower aspect ratio [125].

One possible explanation for this scenario could be that the turbulent fluctuations of TEM turbulence nonlinearly excite the linearly stable ITG modes. This is reasonable by elimination, as there is insufficient linear drive and no alternative nonlinear drive for the ITG modes other than the TEM turbulence. Therefore, it appears that ETG+23% is the critical gradient not only for TEM turbulence, but for hybrid ITG/TEM turbulence. This could explain the high heat-flux stiffness in our simulations at $\rho = 0.90$ (see Fig. 5.28). To further test this hypothesis directly (rather than indirectly as we have done), one could trace the nonlinear transfer of energy from one linear mode to another using the methods of proper orthogonal decomposition (POD), which have been pioneered and implemented into GENE by David Hatch [88]. This analysis is beyond the scope of the present work.

We now introduce electric field shear due to the L-mode E_r-well present in the edge region of most tokamaks. Generally, E_r-wells are much more pronounced in H-mode configurations, but are also present in L-mode plasmas [38] (see Fig. 5.5). We find that a value of $\omega_{E\times B} = 0.5\ c_s/L_{\mathrm{ref}}$, which is in the middle of the experimentally inferred range, is able to reduce the total heat flux approximately to the experimentally inferred values (see Fig. 5.39). Therefore,

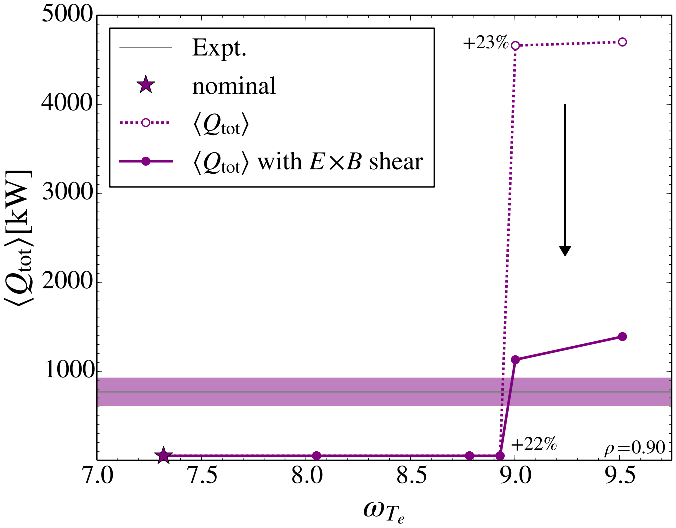

Figure 5.39: Effect of $\boldsymbol{E}\times\boldsymbol{B}$ shear on the total heat flux. Inclusion of the experimental $\boldsymbol{E}\times\boldsymbol{B}$ shearing rate as a simulation parameter at $\rho = 0.90$ helps match the experimental heat flux with ETG+23%. This indicates that the radial electric field is an important parameter of nonlinear simulations in the edge region.

the $\boldsymbol{E} \times \boldsymbol{B}$ shearing rate may be an important simulation parameter to accurately model the heat flux in the edge region of L-mode plasmas. The flux spectrum of nonlinear simulations with $\boldsymbol{E} \times \boldsymbol{B}$ shear peaks at $k_y \rho_s = 0.20$ rather than $k_y \rho_s = 0.15$ for simulations without shear (see Fig. 5.40). This supports the notion that $\boldsymbol{E} \times \boldsymbol{B}$ shear is effective at mitigating transport at large scales. We conclude that we are able to reproduce the total experimental heat flux at $\rho = 0.90$ with an increase of ω_{T_e} by $\sim 23\%$. This increase is within the experimental uncertainty of the Thomson scattering data at the 1.3σ level (see Fig. 5.4).

Lastly, multi-scale effects may be present at $\rho = 0.90$, but their investigation is computationally too expensive to fit within the scope of this work. Based on our experience with highly unstable ITG modes at $\rho = 0.80$, we predict that the effect of electron-scale streamers would likely be strongly reduced by the highly unstable ITG/TEM turbulence found at the ion scales at $\rho = 0.90$.

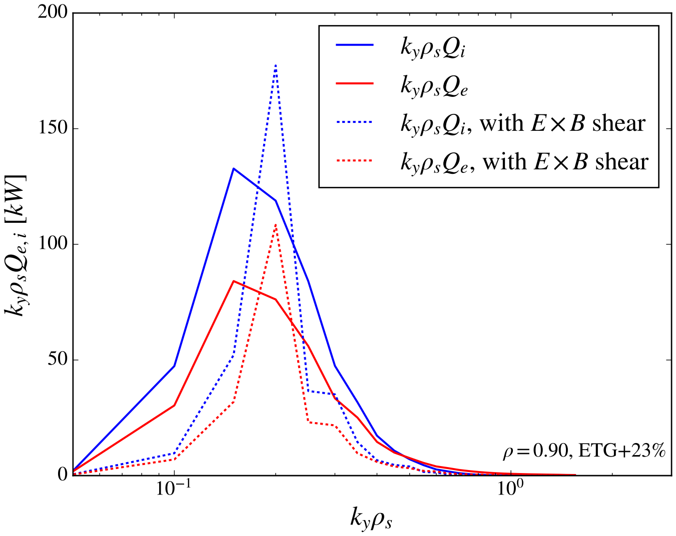

Figure 5.40: Flux spectrum at $\rho = 0.90$ with ETG+23%. For the nonlinear simulations with $\boldsymbol{E} \times \boldsymbol{B}$ shear, the flux spectrum peaks at $k_y \rho_s = 0.20$ rather than at $k_y \rho_s = 0.15$ for simulations without shear. This supports the notion that $\boldsymbol{E} \times \boldsymbol{B}$ shear is effective at mitigating transport at large scales in the near-edge and edge regions.

5.7.3 Sensitivity to the ion temperature gradient

Given the above evidence for a hybrid ITG/TEM scenario when ETG+23%, we now turn our attention to sensitivity of the ITG modes to changes in ITG when ETG is nominal.

Linear simulations show that linear growth rates of ITG modes are unstable when ITG+50% and ITG+80% (see Fig. 5.41). A systematic search finds that the critical linear gradient for ITG modes occurs at ITG+36% (see Fig. 5.42). This suggests that ITG modes are linearly stable to a relatively high degree. Since nonlinear critical gradients are typically higher than linear critical gradients, nonlinear simulations will be carried out with increases in ITG that are higher than the linear critical gradient of ITG+36%. Therefore, our study of the linear critical gradient has helped constrain the parameter space for nonlinear simulations. We will now test the sensitivity of the nonlinear heat flux to increases in ion temperature gradient.

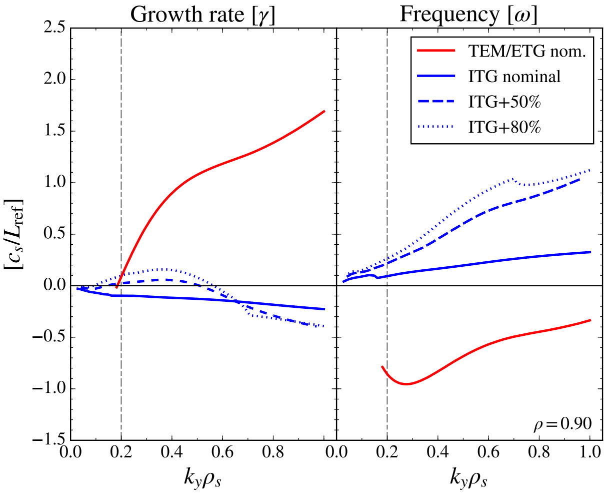

Figure 5.41: Sensitivity of linear growth rates and frequencies to changes in ITG at $\rho = 0.90$. Relatively large changes in ITG are required to drive ITG modes linearly unstable.

Nonlinear simulations at $\rho = 0.90$ show large changes in total heat flux with relatively small changes in ITG from ITG+38% to ITG+50% (see Fig. 5.43). This behavior is not entirely unexpected given our experience with the sensitivity of the heat flux to changes in ETG in the previous section. For instance, for the ITG+38% case we see very little heat flux as expected from to the proximity to the linear critical gradient of ITG+36%. However,

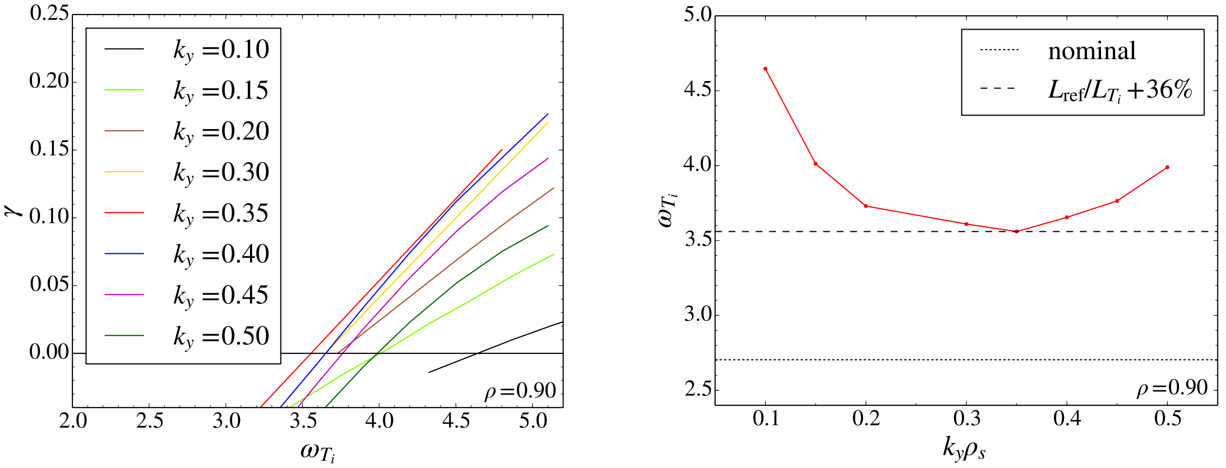

(a) Linear critical gradient for each k_y mode

(b) Minimum linear critical gradient

Figure 5.42: Determination of the critical linear ion temperature gradient at $\rho = 0.90$. The critical gradient is found to be ITG+36%, which is useful for constraining the parameter space for nonlinear simulations.

when increasing the ITG further to ITG+50%, we find that the ITG modes become highly unstable and drive heat flux up to 10 MW. This heat flux is predominantly carried in the ion channel, as expected from ITG modes. Moreover, the heat flux spectrum shows that the heat flux is carried predominantly at wavenumbers associated with the ion scales, i.e. $k_y\rho_s$ = 0.15-0.20 (see Fig. 5.44). However, it may be interesting to investigate whether the ITG modes could also be nonlinearly exciting TEM/ETG modes, which were previously found to be nonlinearly stable at nominal ETG. Such an investigation would proceed in a similar manner in the previous section (i.e. it would carry out indirect tests for the coexistence of TEM/ETG and ITG modes) and could also involve POD, which is beyond the scope of the present work.

As before, with the introduction of the experimentally inferred $\boldsymbol{E} \times \boldsymbol{B}$ shearing rate as a simulation parameter, the high sensitivity to the temperature gradient is tempered (see Fig. 5.43). This indicates that the radial electric field is an important parameter of nonlinear simulations in the edge region. Note that the ratio of heat fluxes is $\sim$ 4 and therefore consistent with the experimentally observed ratio of $Q_i/Q_e = 3.68 \pm 0.74$. Note that in nonlinear simulations with and without $\boldsymbol{E} \times \boldsymbol{B}$ shear effects this ratio is self-consistently preserved.

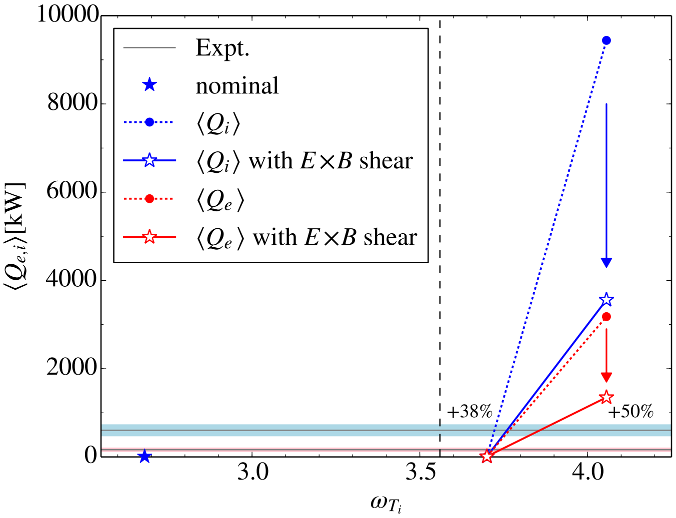

Figure 5.43: Sensitivity of the heat flux to changes in ITG at $\rho = 0.90$. Nonlinear simulations show large changes in heat flux with small changes in ITG, namely from +38% to +50% above nominal. The vertical dashed line represents the linear critical gradient of +36% above nominal, with all nonlinear simulations performed above this gradient. The experimentally inferred $\boldsymbol{E} \times \boldsymbol{B}$ shear tempers the sensitivity of the heat flux to the ion temperature gradient.

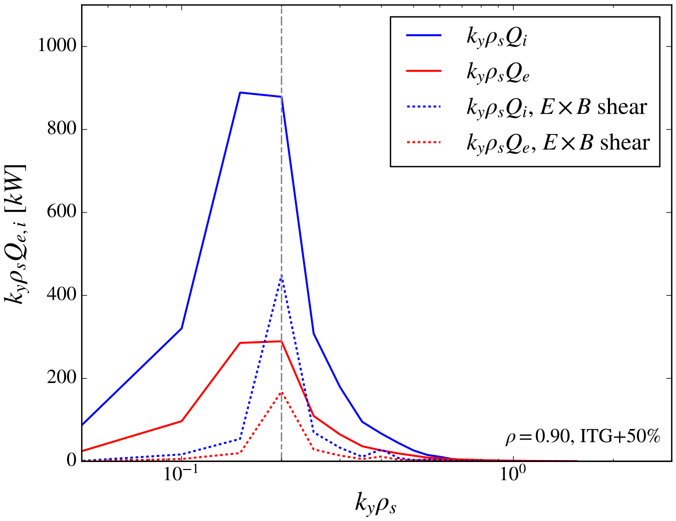

Figure 5.44: Flux spectra at $\rho = 0.90$ for ITG+50% with and without $\boldsymbol{E} \times \boldsymbol{B}$ shear. As expected, the electric field shear reduces the efficiency of turbulent heat transport at large scales (low wavenumbers). As for the ETG+23% case, the shear shifts the peak in the flux spectrum to a larger wavenumber and reduces the area under the curves, albeit to a greater degree than for the ETG+23% case.

5.8 Simulation Results at third radial position ($\rho = 0.95$)

We will now focus our attention further out to the edge region of a DIII-D L-mode plasma. Due to the high levels of uncertainty associated with the experimental temperature profile data of DIII-D shot #153624, we have used data from DIII-D shot #140426, which is a very similar L-mode plasma with improved profile data (see left panel of Fig. 5.45). This particular shot uses a similar geometry to #153624 and was therefore chosen as the preferred candidate for further edge studies (a competing candidate DIII-D #171482 was also considered). The high spatial resolution of the Carbon CER diagnostic throughout the near-edge and edge region is particularly useful for constraining simulation parameters (see Fig. 5.45).

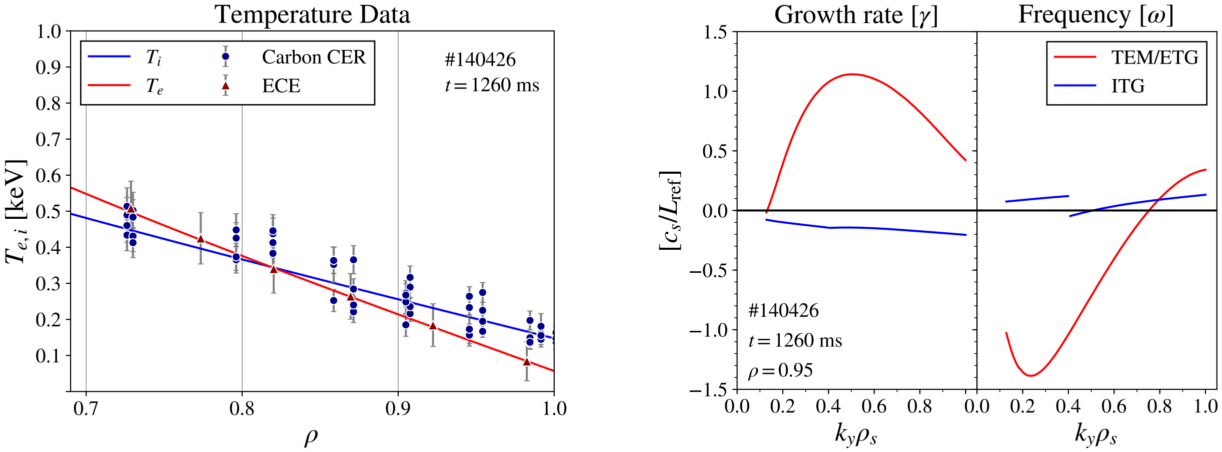

(a) Experimental temperature data.

(b) Linear mode spectrum.

Figure 5.45: a) Experimental temperature data of DIII-D discharge #140426 at $t = 1260$ ms. b) Linear mode spectrum at $\rho = 0.95$. Growth rates and frequencies show a prominent TEM/ETG branch and a sub-dominant ITG branch that is stable. This is comparable to the mode spectrum at $\rho = 0.90$ of discharge #153624.

Linear simulations show a linear mode spectrum that has a prominent TEM/ETG branch and a sub-dominant ITG branch that is stable (see right panel of Fig. 5.45). This is remarkably similar to the mode spectrum at $\rho = 0.90$ of DIII-D shot #153624. An important distinction is that the TEM/ETG branch is peaked in the low-k domain, namely at $k_y\rho_s = 0.50$. Moreover, the TEM/ETG branch is unstable for $k_y\rho_s > 0.13$ (rather than $k_y\rho_s > 0.18$ at $\rho = 0.90$ of the previous shot). Nonetheless, we again expect dominant TEM/ETG turbulence at the ion scales in nonlinear simulations.

Recall that nonlinear ion-scale simulations at $\rho = 0.80$ and $\rho = 0.90$ did not capture significant heat transport for nominal input parameters. To recover the experimental heat flux we increased the ion temperature gradient by $\sim 40\%$ at $\rho = 0.80$ and the electron temperature gradient by $\sim 23\%$ at $\rho = 0.90$. Remarkably, nonlinear simulations at $\rho = 0.95$ produce significant levels of turbulence for nominal experimental input parameters (see Fig. 5.46). Without taking into account the effect of electric field shear, the heat flux exceeds the experimentally observed heat flux by a large factor. However, taking the effect of electric field shear as measured by the DBS diagnostic into account[†], we are able to recover the experimental heat flux with nonlinear simulations at $\rho = 0.95$.

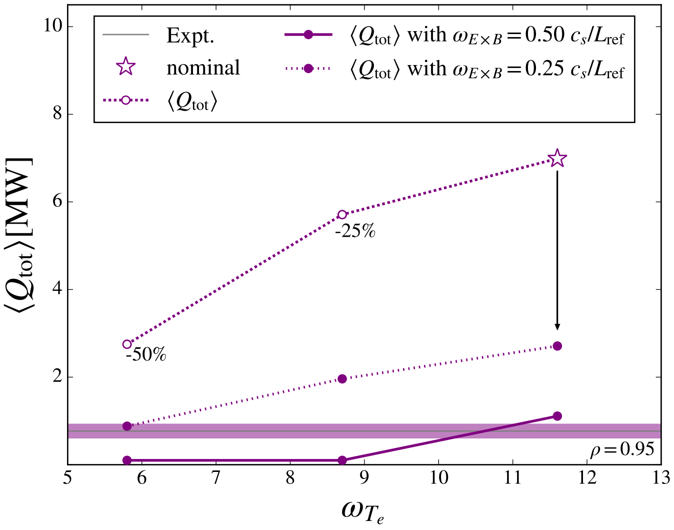

Figure 5.46: Nonlinear simulation results at third radial position ($\rho = 0.95$). Simulations are able to match the experimental heat flux with the inclusion of $\boldsymbol{E} \times \boldsymbol{B}$ shear and *nominal* ETG. The approximately linear dependence on ETG suggests that high heat flux stiffness is not a general feature of nonlinear turbulence in the near-edge region.

Moreover, the high degree of heat flux stiffness that has been observed at $\rho = 0.90$ is not found at $\rho = 0.95$. To study the heat flux stiffness, we have gradually reduced the electron temperate gradient to ETG−25% and ETG−50%. The heat flux responds approximately linearly to these changes in electron temperature gradient (see Fig. 5.46). These results

---

[†] We assume for simplicity that the $\boldsymbol{E} \times \boldsymbol{B}$ shear at $\rho = 0.95$ of shot #140426 is similar to the shear at the same radial position of shot #153624 (see Fig. 5.5), namely $\omega_{E\times B} = 0.50\ c_s/L_{\mathrm{ref}}$.

indicate that the turbulence is TEM/ETG dominated as expected from linear simulations. Therefore, high heat flux stiffness is not a general feature of nonlinear turbulence in the near-edge region.

The heat flux spectrum for nominal experimental parameters with and without $\boldsymbol{E} \times \boldsymbol{B}$ shear is shown in Fig. 5.47. For both simulation scenarios, the heat flux is dominated by electrons, which confirms our prediction from linear simulations of significant TEM/ETG turbulence. For simulations without $\boldsymbol{E} \times \boldsymbol{B}$ shear, the heat flux is carried predominantly by a mode at $k_y\rho_s = 0.18$, but there also appears to be a secondary mode active at $k_y\rho_s = 0.32$, as indicated by a sub-dominant peak in the heat flux spectrum there. For simulations with $\boldsymbol{E} \times \boldsymbol{B}$ shear, the heat flux spectrum has a single peak at $k_y\rho_s = 0.27$.

Future work could investigate whether the subdominant mode is an ITG mode in a similar method as described in the previous section. This study is beyond the scope of the present work. We tentatively conclude that the nonlinear behavior of turbulent modes is less predictable in the near-edge than in the core, and may involve multiple modes acting (and interacting) at the ion scales.

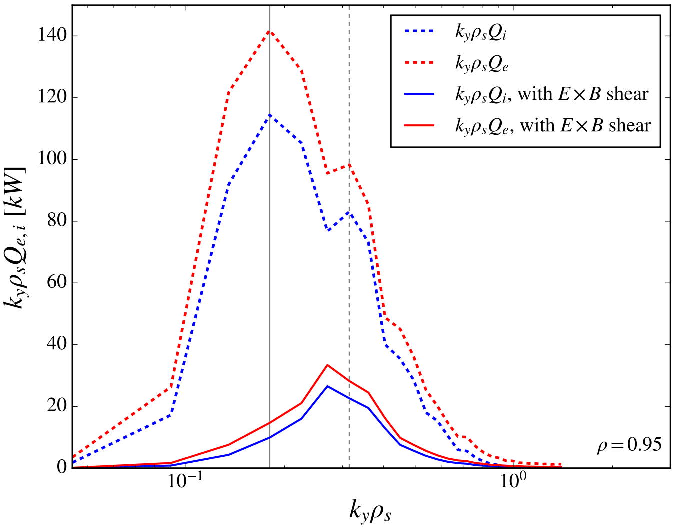

Figure 5.47: Heat flux spectrum at third radial position, $\rho = 0.95$. TEM/ETG modes dominate, with a hint of two very active nonlinear modes, namely at $k_y\rho_s = 0.18$ (*solid line*) and $k_y\rho_s = 0.32$ (*dashed line*).

5.9 Discussion

To address an apparent shortfall problem [59, 60], recent validation exercises studying L-mode plasmas in Alcator C-Mod, ASDEX Upgrade, and DIII-D tokamaks have reduced fears that the shortfall is a universal feature of near-edge L-mode plasmas [53, 54, 81, 107] (see section 5.2). The results presented here are consistent with previous work that has been able to reproduce the experimental heat flux by changing input parameters close to their experimental uncertainty [81, 107].

Results from multi-scale simulations with realistic Deuteron-electron mass ratio and geometry at $\rho = 0.80$ have been presented. An early heuristic rule, found with pioneering multi-scale simulations [49–52], has suggested that ETG-modes can contribute experimentally relevant heat flux if $\gamma_{\mathrm{ETG}}^{\max} / \gamma_{\mathrm{ITG}}^{\max} \gg \sqrt{m_i/m_e}$. This rule of thumb was found using a reduced mass ratio and simplified geometry in the core, and is not expected to apply universally. Nevertheless, this rule appears to hold in recent multi-scale simulations using more realistic parameters with the GKV code [65, 66] and GYRO [55, 126]. In the present work, an example of the limit of applicability of this rule may have been found. Recall that linear simulations give $\gamma_{\mathrm{ETG}}^{\max} / \gamma_{\mathrm{ITG+40\%}}^{\max} = 161$ (see section 5.6.1). However, multi-scale simulations have qualitatively found very little ETG contribution to the overall heat flux with an increase in ITG by 40% (see section 5.6.2). Physically, large-scale turbulent structures of ITG-modes are able to shear ETG streamers apart. Thus, when ITG modes are highly unstable, they strongly reduce the flux carried by high-k modes. More recently, the condition $\mathrm{Max}\left(\gamma_{\mathrm{ETG}}/k_y\right) \geq \mathrm{Max}\left(\gamma_{\mathrm{ITG}}/k_y\right)$ has been identified as a simple test to predict possible multi-scale effects [56]. This test has been validated with recent multi-scale simulations and seems to be less conservative than using only the ratio of maximum growth rates. For our linear simulations at $\rho = 0.80$, this linear condition is only marginally satisfied for the ITG+40% scenario; namely, we get $\mathrm{Max}\left(\gamma_{\mathrm{ETG}}/k_y\right) / \mathrm{Max}\left(\gamma_{\mathrm{ITG}}/k_y\right) = 1.16 > 1$ (see Fig. 5.9). Since this linear test is intended as a heuristic rule and not a hard-and-fast rule, our results of negligible multi-scale effects are not significantly at odds with this linear test. We therefore conclude that the recently proposed test appears to be more useful than relying only the ratio of maximum linear growth rates to instruct whether multi-scale simulations might be necessary.

There are several limitations associated with our study. First, it became necessary to include the $\boldsymbol{E} \times \boldsymbol{B}$ shear for nonlinear simulations at $\rho = 0.90$. As mentioned in section 5.5, the realistic shear in real geometry is given by the Hahm-Burrell formalism, which is not a flux function. For the purposes of our study, we assume that the flux-surface-average shear given by the Waltz-Miller formalism is representative of the total shear effect. This is a common assumption in the simulation community [113]. The more accurate Hahm-Burrell formalism has not been implemented in GENE yet. Nevertheless, our simplifying assumption does not affect the generality of our finding that $\boldsymbol{E} \times \boldsymbol{B}$ shear from the L-mode E_r-well is already important for simulations at $\rho = 0.90$. Second, we have carried out multi-scale simulations in the near-edge for the first time. These simulations would not be possible without simplifying assumptions. For instance, we have relied on GyroLES techniques to replace unresolved dissipation with a model. Moreover, we have relied on a large number of single-scale simulations to empirically determine the validity of our multi-scale simulation parameters. However, multi-scale convergence tests may be helpful to test the sensitivity of multi-scale effects to simulation parameter changes. Since these are computationally expensive they are beyond the scope of the present work. Third, note that particularly the ion temperature data used for this work has a large uncertainty associated with it, likely due to low Carbon density (see Fig. 5.4). We have estimated the relevant statistical uncertainties for the flux-matching temperature gradients to be $\sigma_{\text{ITG, stat}} \sim 15\%$ and $\sigma_{\text{ETG, stat}} \sim 8\%$ (see Section 5.4). We have estimated reasonable systematic uncertainties as $\sigma_{\text{sys}} \sim 10\%$. As a result of these error estimates, we find that our flux-matching gradients of ITG+40% and ETG+23% both fall within $\leq 2\sigma_{\text{stat}} + 1\sigma_{\text{sys}}$. It is worth repeating here that only slightly more than two thirds (68%) of normally distributed measurements fall within $1\sigma_{\text{stat}}$, while most (95%) fall within $2\sigma_{\text{stat}}$ and nearly all (99.7%) fall within $3\sigma_{\text{stat}}$. Therefore, our deviations from the experimental measurements of $\leq 2\sigma_{\text{stat}} + 1\sigma_{\text{sys}}$ are acceptable from a purely statistical perspective and sufficient for gyrokinetic validation. Nonetheless, there may be limitations in our validation method that exclude some relevant physics. For example, we are only considering a local flux-tube domain for our simulations and we are assuming a purely Maxwellian background distribution. While we have ruled out multi-scale effects, using a global model or including non-Maxwellian fast-ions could contribute sufficient missing physics to affect our conclusions. Including these phenomena is beyond the scope of the present work.

CHAPTER 6

Summary and Outlook

6.1 Summary

We have presented results from a study of a DIII-D L-mode plasma in the near-edge. At $\rho = 0.80$, the radial ion flux is quenched by strong poloidal zonal flows for nominal input parameters. In the ITG+40% scenario, nonlinear single-scale simulations give remarkable agreement with both the ion and electron heat fluxes of the experiment. This change in gradient is compatible with the combined statistical and systematic uncertainty in the ion temperature gradient at the 1.6σ level (see Fig. 5.4). At the electron-scales, radially elongated streamers are found to carry significant electron heat flux that is comparable to the experiment. This motivates multi-scale simulations, which were carried out for the first time in the near-edge with realistic mass ratio and geometry. Results suggest that the highly unstable ITG modes in the flux-matched ion-scale simulations strongly suppress turbulent transport at the electron-scales. Therefore, single-scale simulations are sufficient to match the experimentally inferred heat flux by changing the ion temperature gradient within the uncertainty of the experiment at $\rho = 0.80$. At $\rho = 0.90$, nonlinear simulations uncover a hybrid ITG/TEM scenario, which was not predicted by linear simulations. Moreover, nonlinear simulations are able to match the total experimental heat flux in the ETG+23% scenario when $\boldsymbol{E} \times \boldsymbol{B}$ flow shear (as evaluated from Doppler Backscattering measurements) is taken into account. This is consistent with the combined statistical and systematic uncertainty in the electron temperature measurements at the 1.3σ level. At $\rho = 0.95$ of a similar L-mode plasma, we find linear results qualitatively similar to the previous radial position in the previous plasma. Remarkably, nonlinear simulations are able to match the experimental heat flux with the inclusion of $\boldsymbol{E} \times \boldsymbol{B}$ shear and *nominal* temperature gradients. Therefore, our primary conclusion is that gyrokinetic simulations are able to match the heat-flux in the near-edge of the L-mode plasma by varying input parameters close to their experimental uncertainties at $\rho = 0.80$, $\rho = 0.90$ and $\rho = 0.95$.

6.2 Outlook

The present work invites several avenues for future research. For instance, future work could study the nature of multi-scale effects for the ITG+3.5% scenario at $\rho = 0.80$: When ITG modes are marginally unstable, previous multi-scale simulations in the core have found that (i) ETG streamers can contribute experimentally significant transport at small scales [53,54] and (ii) ETG streamers can dampen poloidal zonal flows and enhance ion-scale transport [55]. Similar effects might be found with our simulations in the near-edge when ITG modes are brought close to marginal stability. Building upon the results presented here, future work could quantify the effect of multi-scale interactions in the near-edge of L-mode plasmas.

The main ion temperature profile is often assumed to be equal to the impurity ion temperature measured with the CER diagnostic (see section 5.3). This could introduce systematic errors. However, recent diagnostic development at DIII-D is now able to extract the main ion temperature directly and is currently quantifying this known source of uncertainty [127]. A main ion CER (MICER) diagnostic has been developed to study the Deuterium ion (D^+) charge exchange signal. In order to test the conclusions of this work, future work could study a similar L-mode discharge using data from the more precise and more accurate MICER diagnostic currently under development at DIII-D [127].

Closer to the edge region, global simulations are likely required because the shearing rate changes substantially within a narrow radial region just inside the last closed flux surface. Resistive ballooning modes can also be expected to potentially contribute to thermal edge transport [61–63]. Future work could extend the local simulations of the near-edge of the present work to global simulations of the plasma edge just before an L-H transition [64,110].

Appendix A

A.1 Properties of Curvilinear Coordinates

The coordinate system of choice for the study of tokamak plasmas is based on curvilinear coordinates. The basis vectors in this system are neither orthogonal nor unit vectors, and their length and orientation can vary in space. This can lead to non-trivial properties. For example, curvilinear coordinates can be expressed in two bases (see Ref. 128 for details)

$$\begin{aligned}\mathbf{v} &= v^1\mathbf{e}_1 + v^2\mathbf{e}_2 + v^3\mathbf{e}_3 \\ &= v_1\mathbf{e}^1 + v_2\mathbf{e}^2 + v_3\mathbf{e}^3\,,\end{aligned} \tag{A1}$$

where

$$\mathbf{e}_i \cdot \mathbf{e}^j = \delta^i_j\,. \tag{A2}$$

The variables with an index in the superscript are called contravariant, while variables with an index in the subscript are called covariant. The contravariant basis vectors are defined as

$$\mathbf{e}^i = \nabla q^i\,, \tag{A3}$$

while the covariant basis vectors are defined as

$$\mathbf{e}_i = \frac{\partial \mathbf{r}}{\partial q^i}\,, \tag{A4}$$

where $\mathbf{r}$ is the position vector in these coordinates ($i = 1, 2, 3$). The metric coefficients can be defined in terms of these basis vectors as follows,

$$\begin{aligned}g_{ij} &= \mathbf{e}_i \cdot \mathbf{e}_j \\ g^{ij} &= \mathbf{e}^i \cdot \mathbf{e}^j\,.\end{aligned} \tag{A5}$$

The contravariant metric tensor elements can be obtained from the covariant metric tensor elements with the following inversion operation,

$$[g_{ij}] = J^2 \begin{bmatrix} g^{yy}g^{zz} - (g^{yz})^2 & g^{xz}g^{yz} - g^{xy}g^{zz} & g^{xy}g^{yz} - g^{xz}g^{yy} \\ g^{xz}g^{yz} - g^{xy}g^{zz} & g^{xx}g^{zz} - (g^{xz})^2 & g^{xy}g^{xz} - g^{xx}g^{yz} \\ g^{xy}g^{yz} - g^{xz}g^{yy} & g^{xy}g^{xz} - g^{xx}g^{yz} & g^{xx}g^{yy} - (g^{xy})^2 \end{bmatrix}, \tag{A6}$$

where

$$J^2 = \frac{1}{\det [g^{ij}]} = \det [g_{ij}] \tag{A7}$$

This allows any geometry to be represented in curvilinear coordinates assuming the metric tensor is given. In GENE, the metric tensor is provided from MHD equilibrium codes such as the TRACER-EFIT model.

Disclaimer

References

[1] A. S. Eddington, "The internal constitution of the stars," *Nature*, Vol. 106, pp. 14 EP –, 09 1920. URL: http://dx.doi.org/10.1038/106014a0 (Cited on page 1.)

[2] H. Bethe, "The fusion hybrid," *Phys. Today*, Vol. 32, No. 44–51, 1979. (Cited on page 2.)

[3] E. Gerstner, "Nuclear energy: The hybrid returns," *Nature News*, Vol. 460, No. 7251, pp. 25–28, 2009. (Cited on page 2.)

[4] G. Steigman, "Primordial nucleosynthesis in the precision cosmology era," *Annual Review of Nuclear and Particle Science*, Vol. 57, No. 1, pp. 463–491, 2017/11/08 2007. URL: https://doi.org/10.1146/annurev.nucl.56.080805.140437 (Cited on page 3.)

[5] O. A. Hurricane, D. A. Callahan, D. T. Casey, P. M. Celliers, C. Cerjan, E. L. Dewald, T. R. Dittrich, T. Döppner, D. E. Hinkel, L. F. B. Hopkins, J. L. Kline, S. Le Pape, T. Ma, A. G. MacPhee, J. L. Milovich, A. Pak, H. S. Park, P. K. Patel, B. A. Remington, J. D. Salmonson, P. T. Springer, and R. Tommasini, "Fuel gain exceeding unity in an inertially confined fusion implosion," *Nature*, Vol. 506, pp. 343 EP –, 02 2014. URL: https://doi.org/10.1038/nature13008 (Cited on page 3.)

[6] P. Batistoni, S. Popovichev, A. Cufar, Z. Ghani, L. Giacomelli, S. Jednorog, A. Klix, S. Lilley, E. Laszynska, S. Loreti, L. Packer, A. Peacock, M. Pillon, R. Price, M. Rebai, D. Rigamonti, N. Roberts, M. Tardocchi, D. Thomas, and J. Contributors, "14 MeV calibration of JET neutron detectors—phase 1: calibration and characterization of the neutron source," *Nuclear Fusion*, Vol. 58, No. 2, p. 026012, 2018. URL: http://stacks.iop.org/0029-5515/58/i=2/a=026012 (Cited on page 3.)

[7] H. J. de Blank, "Guiding center motion," *Fusion Science and Technology*, Vol. 49, No. 2T, pp. 59–66, 2006. doi: 10.13182/FST06-A1104. URL: https://doi.org/10.13182/FST06-A1104 (Cited on pages 4 and 58.)

[8] JET-EFDA (now EUROfusion), “Tokamak principle,” 2011. URL: https://www.euro-fusion.org/news/detail/tokamak-principle/? (Cited on page 5.)

[9] J. H. E. Proll, “Trapped-particle instabilities in quasi-isodynamic stellarators,” *PhD Thesis*, Jan 2014. URL: http://inis.iaea.org/search/search.aspx?orig_q=RN:46031821 (Cited on page 4.)

[10] ITER Physics Expert Groups on Confinement and Transport *et al.*, “Chapter 2: Plasma confinement and transport,” *Nuclear Fusion*, Vol. 39, No. 12, pp. 2175–2249, Dec 1999. doi: 10.1088/0029-5515/39/12/302. URL: https://doi.org/10.1088/0029-5515/39/12/302 (Cited on page 6.)

[11] H.-S. Bosch and G. Hale, “Improved formulas for fusion cross-sections and thermal reactivities,” *Nuclear Fusion*, Vol. 32, No. 4, p. 611, 1992. URL: http://stacks.iop.org/0029-5515/32/i=4/a=I07 (Cited on page 6.)

[12] J. D. Lawson, “Some criteria for a power producing thermonuclear reactor,” *Proceedings of the Physical Society. Section B*, Vol. 70, No. 1, p. 6, 1957. URL: http://stacks.iop.org/0370-1301/70/i=1/a=303 (Cited on page 7.)

[13] R. Moir and W. Barr, “‘Venetian-blind’ direct energy converter for fusion reactors,” *Nuclear Fusion*, Vol. 13, No. 1, p. 35, 1973. URL: http://stacks.iop.org/0029-5515/13/i=1/a=005 (Cited on page 7.)

[14] W. L. Barr, R. W. Moir, and G. W. Hamilton, “Experimental results from a beam direct converter at 100 kV,” *Journal of Fusion Energy*, Vol. 2, No. 2, pp. 131–143, Apr 1982. doi: 10.1007/BF01054580. URL: https://doi.org/10.1007/BF01054580 (Cited on page 7.)

[15] M. N. Rosenbluth and F. L. Hinton, “Generic issues for direct conversion of fusion energy from alternative fuels,” *Plasma Physics and Controlled Fusion*, Vol. 36, No. 8, p. 1255, 1994. URL: http://stacks.iop.org/0741-3335/36/i=8/a=003 (Cited on page 7.)

[16] A. J. Webster, "Fusion: Power for the future," *Physics Education*, Vol. 38, No. 2, p. 135, 2003. URL: http://stacks.iop.org/0031-9120/38/i=2/a=305 (Cited on page 8.)

[17] A. Dinklage, T. Klinger, G. Marx, and L. Schweikhard, Eds., *Plasma Physics: Confinement, Transport and Collective Effects.* Springer, Berlin, Heidelberg, 2005. (Cited on page 9.)

[18] R. Goldston and P. Rutherford, *Introduction to Plasma Physics.* Boca Raton: CRC Press, 1995. (Cited on page 9.)

[19] S. C. Cowley, "The quest for fusion power," *Nature Physics*, Vol. 12, pp. 384 EP –, 05 2016. URL: http://dx.doi.org/10.1038/nphys3719 (Cited on page 10.)

[20] B. Sorbom, J. Ball, T. Palmer, F. Mangiarotti, J. Sierchio, P. Bonoli, C. Kasten, D. Sutherland, H. Barnard, C. Haakonsen, J. Goh, C. Sung, and D. Whyte, "ARC: A compact, high-field, fusion nuclear science facility and demonstration power plant with demountable magnets," *Fusion Engineering and Design*, Vol. 100, pp. 378 – 405, 2015. doi: https://doi.org/10.1016/j.fusengdes.2015.07.008. URL: http://www.sciencedirect.com/science/article/pii/S0920379615302337 (Cited on page 10.)

[21] M. P. Gryaznevich, V. A. Chuyanov, D. Kingham, A. Sykes, and T. E. Ltd, "Advancing fusion by innovations: Smaller, quicker, cheaper," *Journal of Physics: Conference Series*, Vol. 591, No. 1, p. 012005, 2015. URL: http://stacks.iop.org/1742-6596/591/i=1/a=012005 (Cited on page 10.)

[22] J. Menard, L. Bromberg, T. Brown, T. Burgess, D. Dix, L. El-Guebaly, T. Gerrity, R. Goldston, R. Hawryluk, R. Kastner, C. Kessel, S. Malang, J. Minervini, G. Neilson, C. Neumeyer, S. Prager, M. Sawan, J. Sheffield, A. Sternlieb, L. Waganer, D. Whyte, and M. Zarnstorff, "Prospects for pilot plants based on the tokamak, spherical tokamak and stellarator," *Nuclear Fusion*, Vol. 51, No. 10, p. 103014, 2011. URL: http://stacks.iop.org/0029-5515/51/i=10/a=103014 (Cited on page 10.)

[23] J. Menard, T. Brown, L. El-Guebaly, M. Boyer, J. Canik, B. Colling, R. Raman, Z. Wang, Y. Zhai, P. Buxton, B. Covele, C. D'Angelo, A. Davis, S. Gerhardt, M. Gryaznevich, M. Harb, T. Hender, S. Kaye, D. Kingham, M. Kotschenreuther, S. Mahajan, R. Maingi, E. Marriott, E. Meier, L. Mynsberge, C. Neumeyer, M. Ono, J.-K. Park, S. Sabbagh, V. Soukhanovskii, P. Valanju, and R. Woolley, "Fusion nuclear science facilities and pilot plants based on the spherical tokamak," *Nuclear Fusion*, Vol. 56, No. 10, p. 106023, 2016. URL: http://stacks.iop.org/0029-5515/56/i=10/a=106023 (Cited on page 10.)

[24] J. W. Conner and H. R. Wilson, "Survey of theories of anomalous transport," *Plasma Physics and Controlled Fusion*, Vol. 36, No. 5, p. 719, 1994. URL: http://stacks.iop.org/0741-3335/36/i=5/a=002 (Cited on page 11.)

[25] W. Horton, "Drift waves and transport," *Rev. Mod. Phys.*, Vol. 71, pp. 735–778, Apr 1999. doi: 10.1103/RevModPhys.71.735. URL: https://link.aps.org/doi/10.1103/RevModPhys.71.735 (Cited on pages 11, 15, and 67.)

[26] M. Rosenbluth and C. Longmire, "Stability of plasmas confined by magnetic fields," *Annals of Physics*, Vol. 1, No. 2, pp. 120 – 140, 1957. doi: https://doi.org/10.1016/0003-4916(57)90055-6. URL: http://www.sciencedirect.com/science/article/pii/0003491657900556 (Cited on pages 11 and 19.)

[27] P. N. Guzdar, L. Chen, W. M. Tang, and P. H. Rutherford, "Ion–temperature–gradient instability in toroidal plasmas," *The Physics of Fluids*, Vol. 26, No. 3, pp. 673–677, 1983. doi: 10.1063/1.864182. URL: https://aip.scitation.org/doi/abs/10.1063/1.864182 (Cited on page 11.)

[28] G. W. Hammett and F. W. Perkins, "Fluid moment models for landau damping with application to the ion-temperature-gradient instability," *Phys. Rev. Lett.*, Vol. 64, pp. 3019–3022, Jun 1990. doi: 10.1103/PhysRevLett.64.3019. URL: https://link.aps.org/doi/10.1103/PhysRevLett.64.3019 (Cited on page 11.)

[29] W. Dorland, F. Jenko, M. Kotschenreuther, and B. N. Rogers, “Electron temperature gradient turbulence,” *Physical Review Letters*, Vol. 85, No. 26, pp. 5579–5582, 12 2000. doi: 10.1103/PhysRevLett.85.5579. URL: https://link.aps.org/doi/10.1103/PhysRevLett.85.5579 (Cited on pages 11, 15, 43, and 68.)

[30] F. Jenko, W. Dorland, M. Kotschenreuther, and B. N. Rogers, “Electron temperature gradient driven turbulence,” *Physics of Plasmas*, Vol. 7, No. 5, pp. 1904–1910, 2000. URL: https://doi.org/10.1063/1.874014 (Cited on pages 11, 15, 43, and 68.)

[31] F. Jenko and W. Dorland, “Prediction of significant tokamak turbulence at electron gyroradius scales,” *Physical Review Letters*, Vol. 89, No. 22, pp. 225 001–, 11 2002. URL: https://link.aps.org/doi/10.1103/PhysRevLett.89.225001 (Cited on pages 11, 15, and 68.)

[32] B. Coppi and G. Rewoldt, “New Trapped-Electron Instability,” *Phys. Rev. Lett.*, Vol. 33, pp. 1329–1332, Nov 1974. doi: 10.1103/PhysRevLett.33.1329. URL: https://link.aps.org/doi/10.1103/PhysRevLett.33.1329 (Cited on pages 11 and 22.)

[33] F. Ryter, C. Angioni, A. G. Peeters, F. Leuterer, H.-U. Fahrbach, and W. Suttrop, “Experimental Study of Trapped-Electron-Mode Properties in Tokamaks: Threshold and Stabilization by Collisions,” *Phys. Rev. Lett.*, Vol. 95, p. 085001, Aug 2005. doi: 10.1103/PhysRevLett.95.085001. URL: https://link.aps.org/doi/10.1103/PhysRevLett.95.085001 (Cited on pages 11 and 22.)

[34] W. Guttenfelder, S. Kaye, D. Kriete, R. Bell, A. Diallo, B. LeBlanc, G. McKee, M. Podesta, S. Sabbagh, and D. Smith, “Initial transport and turbulence analysis and gyrokinetic simulation validation in NSTX-U L-mode plasmas,” *Nuclear Fusion*, Vol. 59, No. 5, p. 056027, Apr 2019. doi: 10.1088/1741-4326/ab0b2c. URL: https://doi.org/10.1088/1741-4326/ab0b2c (Cited on page 11.)

[35] F. Wagner, G. Becker, K. Behringer, D. Campbell, A. Eberhagen, W. Engelhardt, G. Fussmann, O. Gehre, J. Gernhardt, G. v. Gierke, G. Haas, M. Huang, F. Karger, M. Keilhacker, O. Klüber, M. Kornherr, K. Lackner, G. Lisitano, G. G. Lister, H. M.

Mayer, D. Meisel, E. R. Müller, H. Murmann, H. Niedermeyer, W. Poschenrieder, H. Rapp, H. Röhr, F. Schneider, G. Siller, E. Speth, A. Stäbler, K. H. Steuer, G. Venus, O. Vollmer, and Z. Yü, "Regime of Improved Confinement and High Beta in Neutral-Beam-Heated Divertor Discharges of the ASDEX Tokamak," *Phys. Rev. Lett.*, Vol. 49, pp. 1408–1412, Nov 1982. doi: 10.1103/PhysRevLett.49.1408. URL: https://link.aps.org/doi/10.1103/PhysRevLett.49.1408 (Cited on pages 13 and 66.)

[36] ASDEX Team, "The H-Mode of ASDEX," *Nuclear Fusion*, Vol. 29, No. 11, p. 1959, 1989. URL: http://stacks.iop.org/0029-5515/29/i=11/a=010 (Cited on page 13.)

[37] M. Keilhacker, "H-mode confinement in tokamaks," *Plasma Physics and Controlled Fusion*, Vol. 29, No. 10A, p. 1401, 1987. URL: http://stacks.iop.org/0741-3335/29/i=10A/a=320 (Cited on page 13.)

[38] F. Wagner, "A quarter-century of H-mode studies," *Plasma Physics and Controlled Fusion*, Vol. 49, No. 12B, p. B1, 2007. URL: http://stacks.iop.org/0741-3335/49/i=12B/a=S01 (Cited on pages 13, 15, 66, 71, and 109.)

[39] J. W. Connor and H. R. Wilson, "A review of theories of the L-H transition," *Plasma Physics and Controlled Fusion*, Vol. 42, No. 1, p. R1, 2000. URL: http://stacks.iop.org/0741-3335/42/i=1/a=201 (Cited on pages 13 and 66.)

[40] D. A. Batchelor, M. Beck, A. Becoulet, R. V. Budny, C. S. Chang, P. H. Diamond, J. Q. Dong, G. Y. Fu, A. Fukuyama, T. S. Hahm, D. E. Keyes, Y. Kishimoto, S. Klasky, L. L. Lao, K. Li, Z. Lin, B. Ludaescher, J. Manickam, N. Nakajima, T. Ozeki, N. Podhorszki, W. M. Tang, M. A. Vouk, R. E. Waltz, S. J. Wang, H. R. Wilson, X. Q. Xu, M. Yagi, and F. Zonca, "Simulation of Fusion Plasmas: Current Status and Future Direction," *Plasma Science and Technology*, Vol. 9, No. 3, p. 312, 2007. URL: http://stacks.iop.org/1009-0630/9/i=3/a=13 (Cited on pages 13, 15, and 66.)

[41] P. W. Terry, "Suppression of turbulence and transport by sheared flow," *Rev. Mod. Phys.*, Vol. 72, pp. 109–165, Jan 2000. doi: 10.1103/RevModPhys.72.109. URL: http://link.aps.org/doi/10.1103/RevModPhys.72.109 (Cited on page 13.)

[42] P. H. Diamond and Y.-B. Kim, "Theory of mean poloidal flow generation by turbulence," *Physics of Fluids B*, Vol. 3, No. 7, pp. 1626–1633, 1991. doi: 10.1063/1.859681. URL: http://scitation.aip.org/content/aip/journal/pofb/3/7/10.1063/1.859681 (Cited on page 14.)

[43] P. H. Diamond, Y.-M. Liang, B. A. Carreras, and P. W. Terry, "Self-regulating shear flow turbulence: A paradigm for the L to H transition," *Phys. Rev. Lett.*, Vol. 72, pp. 2565–2568, Apr 1994. doi: 10.1103/PhysRevLett.72.2565. URL: http://link.aps.org/doi/10.1103/PhysRevLett.72.2565 (Cited on page 14.)

[44] S. B. Korsholm, P. K. Michelsen, V. Naulin, J. J. Rasmussen, L. Garcia, B. A. Carreras, and V. E. Lynch, "Reynolds stress and shear flow generation," *Plasma Physics and Controlled Fusion*, Vol. 43, No. 10, p. 1377, 2001. URL: http://stacks.iop.org/0741-3335/43/i=10/a=308 (Cited on page 14.)

[45] P. Snyder, W. Solomon, K. Burrell, A. Garofalo, B. Grierson, R. Groebner, A. Leonard, R. Nazikian, T. Osborne, E. Belli, J. Candy, and H. Wilson, "Super H-mode: theoretical prediction and initial observations of a new high performance regime for tokamak operation," *Nuclear Fusion*, Vol. 55, No. 8, p. 083026, 2015. URL: http://stacks.iop.org/0029-5515/55/i=8/a=083026 (Cited on page 14.)

[46] P. Snyder, J. Hughes, T. Osborne, C. Paz-Soldan, W. Solomon, M. Knolker, D. Eldon, T. Evans, T. Golfinopoulos, B. Grierson, R. Groebner, A. Hubbard, E. Kolemen, B. LaBombard, F. Laggner, O. Meneghini, S. Mordijck, T. Petrie, S. Scott, H. Wang, H. Wilson, and Y. Zhu, "High fusion performance in Super H-mode experiments on Alcator C-Mod and DIII-D," *Nuclear Fusion*, Vol. 59, No. 8, p. 086017, Jun 2019. doi: 10.1088/1741-4326/ab235b. URL: https://doi.org/10.1088/1741-4326/ab235b (Cited on page 14.)

[47] E. Mazzucato, D. R. Smith, R. E. Bell, S. M. Kaye, J. C. Hosea, B. P. LeBlanc, J. R. Wilson, P. M. Ryan, C. W. Domier, N. C. Luhmann, H. Yuh, W. Lee, and H. Park, "Short-Scale Turbulent Fluctuations Driven by the Electron-Temperature Gradient in the National Spherical Torus Experiment," *Physical Review Letters*, Vol. 101, No. 7, pp. 075 001–, 08 2008. URL: https://link.aps.org/doi/10.1103/PhysRevLett.101.075001 (Cited on pages 15 and 68.)

[48] T. L. Rhodes, W. A. Peebles, M. A. V. Zeeland, J. S. deGrassie, R. V. Bravenec, K. H. Burrell, J. C. DeBoo, J. Lohr, C. C. Petty, X. V. Nguyen, E. J. Doyle, C. M. Greenfield, L. Zeng, and G. Wang, "Response of multiscale turbulence to electron cyclotron heating in the DIII-D tokamak," *Physics of Plasmas*, Vol. 14, No. 5, p. 056117, 2007. URL: https://doi.org/10.1063/1.2714019 (Cited on pages 15 and 68.)

[49] F. Jenko, "On the Nature of ETG Turbulence and Cross-Scale Coupling," *J. Plasma Fusion Res. SERIES*, Vol. 6, pp. 11–16, 2004. URL: http://www.jspf.or.jp/Journal/JPFR/itc13/jpfr2004_06-11.pdf (Cited on pages 15, 68, 81, 89, 90, and 117.)

[50] T. Görler and F. Jenko, "Scale Separation between Electron and Ion Thermal Transport," *Phys. Rev. Lett.*, Vol. 100, p. 185002, May 2008. doi: 10.1103/PhysRevLett.100.185002. URL: https://link.aps.org/doi/10.1103/PhysRevLett.100.185002 (Cited on pages 15, 68, 81, 89, 90, 92, and 117.)

[51] T. Görler and F. Jenko, "Multiscale features of density and frequency spectra from nonlinear gyrokinetics," *Physics of Plasmas*, Vol. 15, No. 10, 2008. URL: http://scitation.aip.org/content/aip/journal/pop/15/10/10.1063/1.3006086 (Cited on pages 15, 68, 81, 89, 90, 92, and 117.)

[52] R. E. Waltz, J. Candy, and M. Fahey, "Coupled ion temperature gradient and trapped electron mode to electron temperature gradient mode gyrokinetic simulations," *Physics of Plasmas*, Vol. 14, No. 5, p. 056116, 2007. URL: https://doi.org/10.1063/1.2436851 (Cited on pages 15, 68, 81, 89, 90, and 117.)

[53] N. Howard, A. White, M. Reinke, M. Greenwald, C. Holland, J. Candy, and J. Walk, "Validation of the gyrokinetic model in ITG and TEM dominated L-mode plasmas," *Nuclear Fusion*, Vol. 53, No. 12, p. 123011, 2013. URL: http://stacks.iop.org/0029-5515/53/i=12/a=123011 (Cited on pages 15, 67, 68, 83, 117, and 121.)

[54] N. Howard, C. Holland, A. White, M. Greenwald, and J. Candy, "Multi-scale gyrokinetic simulation of tokamak plasmas: enhanced heat loss due to cross-scale coupling of plasma turbulence," *Nuclear Fusion*, Vol. 56, No. 1, p. 014004, 2016. URL: http://stacks.iop.org/0029-5515/56/i=1/a=014004 (Cited on pages 15, 67, 68, 83, 117, and 121.)

[55] S. Maeyama, Y. Idomura, T.-H. Watanabe, M. Nakata, M. Yagi, N. Miyato, A. Ishizawa, and M. Nunami, "Cross-scale interactions between electron and ion scale turbulence in a tokamak plasma," *Phys. Rev. Lett.*, Vol. 114, p. 255002, Jun 2015. URL: http://link.aps.org/doi/10.1103/PhysRevLett.114.255002 (Cited on pages 15, 68, 117, and 121.)

[56] G. Staebler, N. Howard, J. Candy, and C. Holland, "A model of the saturation of coupled electron and ion scale gyrokinetic turbulence," *Nuclear Fusion*, Vol. 57, No. 6, p. 066046, 2017. URL: http://stacks.iop.org/0029-5515/57/i=6/a=066046 (Cited on pages 15, 68, 82, and 117.)

[57] F. Imbeaux, J. Citrin, J. Hobirk, G. Hogeweij, F. Köchl, V. Leonov, S. Miyamoto, Y. Nakamura, V. Parail, G. Pereverzev, A. Polevoi, I. Voitsekhovitch, V. Basiuk, R. Budny, T. Casper, J. Fereira, A. Fukuyama, J. Garcia, Y. Gribov, N. Hayashi, M. Honda, I. Hutchinson, G. Jackson, A. Kavin, C. Kessel, R. Khayrutdinov, C. Labate, X. Litaudon, P. Lomas, J. Lönnroth, T. Luce, V. Lukash, M. Mattei, D. Mikkelsen, I. Nunes, Y. Peysson, P. Politzer, M. Schneider, G. Sips, G. Tardini, S. Wolfe, V. Zhogolev, ASDEX Upgrade Team, C-Mod Team, DIII-D Team, JET-EFDA contributors, JT-60U Team, Tore Supra Team, contributors of the EU-ITM ITER Scenario Modelling group, ITPA 'Integrated Operation Scenarios'

group members and experts, and ITPA 'Transport and Confinement' group members and experts, "Current ramps in tokamaks: from present experiments to ITER scenarios," *Nuclear Fusion*, Vol. 51, No. 8, p. 083026, 2011. URL: https://doi.org/10.1088/0029-5515/51/8/083026 (Cited on page 16.)

[58] J. Candy and R. E. Waltz, "Anomalous Transport Scaling in the DIII-D Tokamak Matched by Supercomputer Simulation," *Phys. Rev. Lett.*, Vol. 91, p. 045001, Jul 2003. doi: 10.1103/PhysRevLett.91.045001. URL: http://link.aps.org/doi/10.1103/PhysRevLett.91.045001 (Cited on pages 16, 24, and 67.)

[59] C. Holland, A. E. White, G. R. McKee, M. W. Shafer, J. Candy, R. E. Waltz, L. Schmitz, and G. R. Tynan, "Implementation and application of two synthetic diagnostics for validating simulations of core tokamak turbulence," *Physics of Plasmas*, Vol. 16, No. 5, p. 052301, 2009. URL: https://doi.org/10.1063/1.3085792 (Cited on pages 16, 67, and 117.)

[60] T. Rhodes, C. Holland, S. Smith, A. White, K. Burrell, J. Candy, J. DeBoo, E. Doyle, J. Hillesheim, J. Kinsey, G. McKee, D. Mikkelsen, W. Peebles, C. Petty, R. Prater, S. Parker, Y. Chen, L. Schmitz, G. Staebler, R. Waltz, G. Wang, Z. Yan, and L. Zeng, "L-mode validation studies of gyrokinetic turbulence simulations via multiscale and multifield turbulence measurements on the DIII-D tokamak," *Nuclear Fusion*, Vol. 51, No. 6, p. 063022, 2011. URL: http://stacks.iop.org/0029-5515/51/i=6/a=063022 (Cited on pages 16, 67, and 117.)

[61] C. Bourdelle, X. Garbet, R. Singh, and L. Schmitz, "New glance at resistive ballooning modes at the edge of tokamak plasmas," *Plasma Physics and Controlled Fusion*, Vol. 54, No. 11, p. 115003, 2012. URL: http://stacks.iop.org/0741-3335/54/i=11/a=115003 (Cited on pages 19, 22, 67, and 121.)

[62] B. I. Cohen, M. V. Umansky, W. M. Nevins, M. A. Makowski, J. A. Boedo, D. L. Rudakov, G. R. McKee, Z. Yan, and R. J. Groebner, "Simulations of drift resistive ballooning L-mode turbulence in the edge plasma of the DIII-D tokamak," *Physics*

of Plasmas, Vol. 20, No. 5, p. 055906, 2013. URL: https://doi.org/10.1063/1.4804638 (Cited on pages 19, 22, 67, and 121.)

[63] T. Rafiq, A. H. Kritz, V. Tangri, A. Y. Pankin, I. Voitsekhovitch, and R. V. Budny, "Integrated modeling of temperature profiles in L-mode tokamak discharges," *Physics of Plasmas*, Vol. 21, No. 12, p. 122505, 2014. doi: 10.1063/1.4903464. URL: https://doi.org/10.1063/1.4903464 (Cited on pages 19, 22, 67, and 121.)

[64] L. Schmitz, L. Zeng, T. L. Rhodes, J. C. Hillesheim, E. J. Doyle, R. J. Groebner, W. A. Peebles, K. H. Burrell, and G. Wang, "Role of Zonal Flow Predator-Prey Oscillations in Triggering the Transition to H-Mode Confinement," *Phys. Rev. Lett.*, Vol. 108, p. 155002, Apr 2012. URL: http://link.aps.org/doi/10.1103/PhysRevLett.108.155002 (Cited on pages 20, 70, 77, and 121.)

[65] T.-H. Watanabe and H. Sugama, "Velocity-space structures of distribution function in toroidal ion temperature gradient turbulence," *Nuclear Fusion*, Vol. 46, No. 1, p. 24, 2006. URL: http://stacks.iop.org/0029-5515/46/i=1/a=003 (Cited on pages 24, 67, and 117.)

[66] S. Maeyama, A. Ishizawa, T.-H. Watanabe, N. Nakajima, S. Tsuji-Iio, and H. Tsutsui, "Numerical techniques for parallel dynamics in electromagnetic gyrokinetic Vlasov simulations," *Computer Physics Communications*, Vol. 184, No. 11, pp. 2462 – 2473, 2013. URL: http://www.sciencedirect.com/science/article/pii/S0010465513002087 (Cited on pages 24, 67, and 117.)

[67] Y. Chen and S. E. Parker, "A δf particle method for gyrokinetic simulations with kinetic electrons and electromagnetic perturbations," *Journal of Computational Physics*, Vol. 189, No. 2, pp. 463 – 475, 2003. URL: https://doi.org/10.1016/S0021-9991(03)00228-6 (Cited on pages 24 and 67.)

[68] Yang Chen and Scott E. Parker, "Electromagnetic gyrokinetic δf particle-in-cell turbulence simulation with realistic equilibrium profiles and geometry," *Journal*

of Computational Physics, Vol. 220, No. 2, pp. 839 – 855, 2007. URL: https://doi.org/10.1016/j.jcp.2006.05.028 (Cited on pages 24 and 67.)

[69] F. Jenko, W. Dorland, M. Kotschenreuther, and B. N. Rogers, "Electron temperature gradient driven turbulence," *Physics of Plasmas*, Vol. 7, No. 5, pp. 1904–1910, 2000. URL: http://dx.doi.org/10.1063/1.874014 (Cited on pages 24, 67, and 78.)

[70] G. G. Howes, S. C. Cowley, W. Dorland, G. W. Hammett, E. Quataert, and A. A. Schekochihin, "Astrophysical gyrokinetics: Basic equations and linear theory," *The Astrophysical Journal*, Vol. 651, No. 1, pp. 590–614, Nov 2006. doi: 10.1086/506172. URL: https://doi.org/10.1086/506172 (Cited on page 26.)

[71] A. J. Brizard and T. S. Hahm, "Foundations of nonlinear gyrokinetic theory," *Rev. Mod. Phys.*, Vol. 79, pp. 421–468, Apr 2007. doi: 10.1103/RevModPhys.79.421. URL: https://link.aps.org/doi/10.1103/RevModPhys.79.421 (Cited on pages 29, 30, 32, 33, 42, and 54.)

[72] R. G. Littlejohn, "Variational principles of guiding centre motion," *Journal of Plasma Physics*, Vol. 29, No. 1, pp. 111–125, 1983. doi: 10.1017/S002237780000060X (Cited on pages 30, 32, and 33.)

[73] J. B. Taylor, "Magnetic moment under short-wave electrostatic perturbations," *The Physics of Fluids*, Vol. 10, No. 6, pp. 1357–1359, 1967. doi: 10.1063/1.1762289. URL: https://aip.scitation.org/doi/abs/10.1063/1.1762289 (Cited on page 32.)

[74] J. R. Cary and R. G. Littlejohn, "Noncanonical hamiltonian mechanics and its application to magnetic field line flow," *Annals of Physics*, Vol. 151, No. 1, pp. 1 – 34, 1983. doi: https://doi.org/10.1016/0003-4916(83)90313-5. URL: http://www.sciencedirect.com/science/article/pii/0003491683903135 (Cited on page 33.)

[75] T. S. Hahm, "Nonlinear gyrokinetic equations for tokamak microturbulence," *The Physics of Fluids*, Vol. 31, No. 9, pp. 2670–2673, 1988. doi: 10.1063/1.866544. URL: https://aip.scitation.org/doi/abs/10.1063/1.866544 (Cited on pages 33 and 34.)

[76] D. Told, “Gyrokinetic microturbulence in transport barriers,” Ph.D. dissertation, Ulm University, 2012. (Cited on pages 35, 37, and 43.)

[77] T. Dannert, “Gyrokinetische Simulation von Plasmaturbulenz mit gefangenen Teilchen und elektromagnetischen Effekten,” Ph.D. dissertation, Technical University of Munich, 2005. URL: http://nbn-resolving.de/urn/resolver.pl?urn:nbn:de:bvb:91-diss2005013115025 (Cited on pages 35, 36, and 37.)

[78] M. L. Boas, *Mathematical Methods in the Physical Sciences*, third edition ed. John Wiley & Sons, 2006. (Cited on page 36.)

[79] A. Banon Navarro, “Gyrokinetic Large Eddy Simulations,” Ph.D. dissertation, Université libre de Bruxelles, Faculté des Sciences – Physique, Bruxelles, 2012. (Cited on pages 40, 43, 48, 51, 55, 56, and 57.)

[80] T. Görler, “Multiscale effects in plasma microturbulence,” Ph.D. dissertation, Universität Ulm, 2009. (Cited on pages 43, 59, and 60.)

[81] T. Görler, A. E. White, D. Told, F. Jenko, C. Holland, and T. L. Rhodes, “A flux-matched gyrokinetic analysis of DIII-D L-mode turbulence,” *Physics of Plasmas*, Vol. 21, No. 12, p. 122307, 2014. URL: http://dx.doi.org/10.1063/1.4904301 (Cited on pages 47, 48, 67, and 117.)

[82] G. Merlo, “Flux-tube and global grid-based gyrokinetic simulations of plasma microturbulence and comparisons with experimental TCV measurements,” 2016. doi: 10.5075/epfl-thesis-7065. URL: http://infoscience.epfl.ch/record/219007 (Cited on page 48.)

[83] K. H. Burrell, “Tests of causality: Experimental evidence that sheared E×B flow alters turbulence and transport in tokamaks,” *Physics of Plasmas*, Vol. 6, No. 12, pp. 4418–4435, 1999. doi: 10.1063/1.873728. URL: https://doi.org/10.1063/1.873728 (Cited on pages 48 and 79.)

[84] H. Biglari, P. H. Diamond, and P. W. Terry, “Influence of sheared poloidal rotation on edge turbulence,” *Physics of Fluids B: Plasma Physics*, Vol. 2, No. 1, pp. 1–4, 1990. doi: 10.1063/1.859529. URL: https://doi.org/10.1063/1.859529 (Cited on pages 48 and 79.)

[85] I. Shesterikov, Y. Xu, G. R. Tynan, P. H. Diamond, S. Jachmich, P. Dumortier, M. Vergote, M. Van Schoor, G. Van Oost, and T. Team, “Experimental Evidence for the Intimate Interaction among Sheared Flows, Eddy Structures, Reynolds Stress, and Zonal Flows across a Transition to Improved Confinement,” *Phys. Rev. Lett.*, Vol. 111, p. 055006, Aug 2013. doi: 10.1103/PhysRevLett.111.055006. URL: https://link.aps.org/doi/10.1103/PhysRevLett.111.055006 (Cited on pages 48 and 79.)

[86] G. W. Hammett, W. Dorland, N. F. Loureiro, and T. Tatsuno, “Implementation of Large Scale $E \times B$ Shear Flow in the GS2 Gyrokinetic Turbulence Code,” *APS Meeting Abstracts*, p. 1136, Oct 2006. URL: http://meetings.aps.org/link/BAPS.2006.DPP.VP1.136 (Cited on pages 49, 50, and 79.)

[87] A. Bañón Navarro, P. Morel, M. Albrecht-Marc, D. Carati, F. Merz, T. Görler, and F. Jenko, “Free Energy Cascade in Gyrokinetic Turbulence,” *Phys. Rev. Lett.*, Vol. 106, p. 055001, Jan 2011. doi: 10.1103/PhysRevLett.106.055001. URL: https://link.aps.org/doi/10.1103/PhysRevLett.106.055001 (Cited on page 54.)

[88] D. R. Hatch, P. W. Terry, F. Jenko, F. Merz, and W. M. Nevins, “Saturation of Gyrokinetic Turbulence through Damped Eigenmodes,” *Phys. Rev. Lett.*, Vol. 106, p. 115003, Mar 2011. doi: 10.1103/PhysRevLett.106.115003. URL: https://link.aps.org/doi/10.1103/PhysRevLett.106.115003 (Cited on pages 54 and 109.)

[89] R. Meyrand, A. Kanekar, W. Dorland, and A. A. Schekochihin, “Fluidization of collisionless plasma turbulence,” *Proceedings of the National Academy of Sciences*,

Vol. 116, No. 4, pp. 1185–1194, 2019. doi: 10.1073/pnas.1813913116. URL: https://www.pnas.org/content/116/4/1185 (Cited on page 54.)

[90] P. Morel, A. Bañón Navarro, M. Albrecht-Marc, D. Carati, F. Merz, T. Görler, and F. Jenko, "Gyrokinetic large eddy simulations," *Physics of Plasmas*, Vol. 18, No. 7, p. 072301, 2011. URL: http://dx.doi.org/10.1063/1.3601053 (Cited on pages 55 and 79.)

[91] P. Morel, A. Bañón Navarro, M. Albrecht-Marc, D. Carati, F. Merz, T. Görler, and F. Jenko, "Dynamic procedure for filtered gyrokinetic simulations," *Physics of Plasmas*, Vol. 19, No. 1, p. 012311, 2012. URL: http://dx.doi.org/10.1063/1.3677366 (Cited on pages 55 and 79.)

[92] A. Bañón Navarro, B. Teaca, F. Jenko, G. W. Hammett, T. Happel, and ASDEX Upgrade Team, "Applications of large eddy simulation methods to gyrokinetic turbulence," *Physics of Plasmas*, Vol. 21, No. 3, p. 032304, 2014. URL: https://doi.org/10.1063/1.4868235 (Cited on pages 55 and 79.)

[93] S. A. Smith and G. W. Hammett, "Eddy viscosity and hyperviscosity in spectral simulations of 2D drift wave turbulence," *Physics of Plasmas*, Vol. 4, No. 4, pp. 978–990, 1997. doi: 10.1063/1.872210. URL: https://doi.org/10.1063/1.872210 (Cited on page 57.)

[94] J. W. Connor, R. J. Hastie, and J. B. Taylor, "Shear, Periodicity, and Plasma Ballooning Modes," *Phys. Rev. Lett.*, Vol. 40, pp. 396–399, Feb 1978. doi: 10.1103/PhysRevLett.40.396. URL: https://link.aps.org/doi/10.1103/PhysRevLett.40.396 (Cited on page 58.)

[95] R. L. Miller, M. S. Chu, J. M. Greene, Y. R. Lin-Liu, and R. E. Waltz, "Noncircular, finite aspect ratio, local equilibrium model," *Physics of Plasmas*, Vol. 5, No. 4, pp. 973–978, 1998. doi: 10.1063/1.872666. URL: https://doi.org/10.1063/1.872666 (Cited on page 59.)

[96] X. Lapillonne, S. Brunner, T. Dannert, S. Jolliet, A. Marinoni, L. Villard, T. Görler, F. Jenko, and F. Merz, "Clarifications to the limitations of the s-α equilibrium model

for gyrokinetic computations of turbulence," *Physics of Plasmas*, Vol. 16, No. 3, p. 032308, 2009. doi: 10.1063/1.3096710. URL: https://doi.org/10.1063/1.3096710 (Cited on page 59.)

[97] M. Kotschenreuther, X. Liu, D. Hatch, L. Zheng, and S. M. Mahajan, "Regimes of weak ITG/TEM modes for transport barriers without velocity shear," 2019. (Cited on page 59.)

[98] H. Sugama, T.-H. Watanabe, and M. Nunami, "Linearized model collision operators for multiple ion species plasmas and gyrokinetic entropy balance equations," *Physics of Plasmas*, Vol. 16, No. 11, p. 112503, 2009. URL: https://doi.org/10.1063/1.3257907 (Cited on pages 60, 62, and 79.)

[99] P. Helander and D. J. Sigmar, *Collisional Transport in Magnetized Plasmas*. Cambridge University Press, 2002. (Cited on page 61.)

[100] T. Casper, W. Meyer, G. Jackson, T. Luce, A. Hyatt, D. Humphreys, and F. Turco, "Validation of the thermal transport model used for ITER startup scenario predictions with diii-d experimental data," *Nuclear Fusion*, Vol. 51, No. 1, p. 013001, Dec 2010. doi: 10.1088/0029-5515/51/1/013001. URL: https://doi.org/10.1088/0029-5515/51/1/013001 (Cited on page 66.)

[101] V. Parail, R. Albanese, R. Ambrosino, J.-F. Artaud, K. Besseghir, M. Cavinato, G. Corrigan, J. Garcia, L. Garzotti, Y. Gribov, F. Imbeaux, F. Koechl, C. Labate, J. Lister, X. Litaudon, A. Loarte, P. Maget, M. Mattei, D. McDonald, E. Nardon, G. Saibene, R. Sartori, and J. Urban, "Self-consistent simulation of plasma scenarios for ITER using a combination of 1.5d transport codes and free-boundary equilibrium codes," *Nuclear Fusion*, Vol. 53, No. 11, p. 113002, Sep 2013. doi: 10.1088/0029-5515/53/11/113002. URL: https://doi.org/10.1088/0029-5515/53/11/113002 (Cited on page 66.)

[102] J. A. Krommes, "The gyrokinetic description of microturbulence in magnetized plasmas," *Annual Review of Fluid Mechanics*, Vol. 44, No. 1, pp. 175–201,

2012. doi: 10.1146/annurev-fluid-120710-101223. URL: https://doi.org/10.1146/annurev-fluid-120710-101223 (Cited on page 66.)

[103] C. Holland, L. Schmitz, T. L. Rhodes, W. A. Peebles, J. C. Hillesheim, G. Wang, L. Zeng, E. J. Doyle, S. P. Smith, R. Prater, K. H. Burrell, J. Candy, R. E. Waltz, J. E. Kinsey, G. M. Staebler, J. C. DeBoo, C. C. Petty, G. R. McKee, Z. Yan, and A. E. White, "Advances in validating gyrokinetic turbulence models against L- and H-mode plasmas," *Physics of Plasmas*, Vol. 18, No. 5, p. 056113, 2011. URL: https://doi.org/10.1063/1.3574518 (Cited on page 67.)

[104] C. Holland, C. Petty, L. Schmitz, K. Burrell, G. McKee, T. Rhodes, and J. Candy, "Progress in GYRO validation studies of DIII-D H-mode plasmas," *Nuclear Fusion*, Vol. 52, No. 11, p. 114007, 2012. URL: http://stacks.iop.org/0029-5515/52/i=11/a=114007 (Cited on page 67.)

[105] A. Bañón Navarro, T. Happel, T. Görler, F. Jenko, J. Abiteboul, A. Bustos, H. Doerk, D. Told, and A. U. Team, "Gyrokinetic studies of core turbulence features in ASDEX Upgrade H-mode plasmas," *Physics of Plasmas*, Vol. 22, No. 4, p. 042513, 2015. URL: https://doi.org/10.1063/1.4919022 (Cited on page 67.)

[106] D. Hatch, D. Told, F. Jenko, H. Doerk, M. Dunne, E. Wolfrum, E. Viezzer, T. A. U. Team, and M. Pueschel, "Gyrokinetic study of ASDEX Upgrade inter-ELM pedestal profile evolution," *Nuclear Fusion*, Vol. 55, No. 6, p. 063028, 2015. URL: http://stacks.iop.org/0029-5515/55/i=6/a=063028 (Cited on page 67.)

[107] D. Told, F. Jenko, T. Görler, F. J. Casson, and E. Fable, "Characterizing turbulent transport in ASDEX Upgrade L-mode plasmas via nonlinear gyrokinetic simulations," *Physics of Plasmas*, Vol. 20, No. 12, p. 122312, 2013. URL: http://dx.doi.org/10.1063/1.4858899 (Cited on pages 67, 74, 85, 108, and 117.)

[108] R. E. Waltz, J. Candy, and R. V. Bravenec, "Revising the L-mode Edge Transport Shortfall with More Accurate Gyrokinetic Simulations," in *APS Meeting Abstracts*,

Oct 2017. URL: http://meetings.aps.org/link/BAPS.2017.DPP.TP11.108 (Cited on page 67.)

[109] J. Candy, E. Belli, and R. Bravenec, "A high-accuracy Eulerian gyrokinetic solver for collisional plasmas," *Journal of Computational Physics*, Vol. 324, pp. 73 – 93, 2016. URL: http://www.sciencedirect.com/science/article/pii/S0021999116303400 (Cited on page 67.)

[110] L. Schmitz, "The role of turbulence–flow interactions in L- to H-mode transition dynamics: Recent progress," *Nuclear Fusion*, Vol. 57, No. 2, p. 025003, 2017. URL: http://stacks.iop.org/0029-5515/57/i=2/a=025003 (Cited on pages 70, 77, and 121.)

[111] J. C. Hillesheim, W. A. Peebles, T. L. Rhodes, L. Schmitz, A. E. White, and T. A. Carter, "New plasma measurements with a multichannel millimeter-wave fluctuation diagnostic system in the DIII-D tokamak," *Review of Scientific Instruments*, Vol. 81, No. 10, p. 10D907, 2010. URL: https://doi.org/10.1063/1.3466900 (Cited on page 70.)

[112] T. S. Hahm and K. H. Burrell, "Flow shear induced fluctuation suppression in finite aspect ratio shaped tokamak plasma," *Physics of Plasmas*, Vol. 2, No. 5, pp. 1648–1651, 1995. doi: 10.1063/1.871313. URL: https://doi.org/10.1063/1.871313 (Cited on page 74.)

[113] R. E. Waltz and R. L. Miller, "Ion temperature gradient turbulence simulations and plasma flux surface shape," *Physics of Plasmas*, Vol. 6, No. 11, pp. 4265–4271, 1999. doi: 10.1063/1.873694. URL: https://doi.org/10.1063/1.873694 (Cited on pages 75 and 118.)

[114] E. Delabie, "Neutral beam driven hydrogen spectroscopy in fusion plasmas," Ph.D. dissertation, Department of Applied Physics - Technische Universiteit Eindhoven, 2011. URL: https://research.tue.nl/en/publications/neutral-beam-driven-hydrogen-spectroscopy-in-fusion-plasmas (Cited on page 77.)

[115] S. R. Haskey, B. A. Grierson, C. Chrystal, A. Ashourvan, K. H. Burrell, R. J. Groebner, E. A. Belli, L. Stagner, D. J. Battaglia, T. Stoltzfus-Dueck,

and A. Bortolon, “Main ion and impurity edge profile evolution across the L- to H-mode transition on DIII-D,” *Plasma Physics and Controlled Fusion*, Vol. 60, No. 10, p. 105001, Aug 2018. doi: 10.1088/1361-6587/aad702. URL: https://doi.org/10.1088/1361-6587/aad702 (Cited on page 77.)

[116] M. A. Beer, S. C. Cowley, and G. W. Hammett, “Field-aligned coordinates for nonlinear simulations of tokamak turbulence,” *Physics of Plasmas*, Vol. 2, No. 7, pp. 2687–2700, 1995. URL: https://doi.org/10.1063/1.871232 (Cited on page 78.)

[117] P. Xanthopoulos and F. Jenko, “Clebsch-type coordinates for nonlinear gyrokinetics in generic toroidal configurations,” *Physics of Plasmas*, Vol. 13, No. 9, p. 092301, 2006. URL: https://doi.org/10.1063/1.2338818 (Cited on page 78.)

[118] S. C. Cowley, R. M. Kulsrud, and R. Sudan, “Considerations of ion-temperature-gradient-driven turbulence,” *Physics of Fluids B*, Vol. 3, No. 10, pp. 2767–2782, 1991. URL: http://scitation.aip.org/content/aip/journal/pofb/3/10/10.1063/1.859913 (Cited on pages 78 and 87.)

[119] P. Xanthopoulos, W. A. Cooper, F. Jenko, Y. Turkin, A. Runov, and J. Geiger, “A geometry interface for gyrokinetic microturbulence investigations in toroidal configurations,” *Physics of Plasmas*, Vol. 16, No. 8, p. 082303, 2009. URL: https://doi.org/10.1063/1.3187907 (Cited on page 79.)

[120] P. Gohil and K. H. Burrell and R. J. Groebner and J. Kim and W. C. Martin and E. L. McKee and R. P. Seraydarian, “The charge exchange recombination diagnostic system on the DIII-D tokamak,” in *The 14th IEEE/NPSS Symposium Fusion Engineering*, Sep 1991, pp. 1199–1204 vol.2. URL: http://dx.doi.org/10.1109/FUSION.1991.218656 (Cited on page 83.)

[121] A. M. Dimits, G. Bateman, M. A. Beer, B. I. Cohen, W. Dorland, G. W. Hammett, C. Kim, J. E. Kinsey, M. Kotschenreuther, A. H. Kritz, L. L. Lao, J. Mandrekas, W. M. Nevins, S. E. Parker, A. J. Redd, D. E. Shumaker, R. Sydora, and J. Weiland, “Comparisons and physics basis of tokamak transport models and

turbulence simulations," *Physics of Plasmas*, Vol. 7, No. 3, pp. 969–983, 2000. URL: http://scitation.aip.org/content/aip/journal/pop/7/3/10.1063/1.873896 (Cited on pages 85 and 86.)

[122] J. F. Drake, P. N. Guzdar, and A. B. Hassam, "Streamer formation in plasma with a temperature gradient," *Phys. Rev. Lett.*, Vol. 61, pp. 2205–2208, Nov 1988. doi: 10.1103/PhysRevLett.61.2205. URL: https://link.aps.org/doi/10.1103/PhysRevLett.61.2205 (Cited on page 87.)

[123] M. Nunami, M. Nakata, S. Toda, A. Ishizawa, R. Kanno, and H. Sugama, "Simulation studies on temperature profile stiffness in itg turbulent transport of helical plasmas for flux-matching technique," *Physics of Plasmas*, Vol. 25, No. 8, p. 082504, 2018. URL: https://doi.org/10.1063/1.5036564 (Cited on page 87.)

[124] F. Jenko, W. Dorland, and G. W. Hammett, "Critical gradient formula for toroidal electron temperature gradient modes," *Physics of Plasmas*, Vol. 8, No. 9, pp. 4096–4104, 2001. URL: http://dx.doi.org/10.1063/1.1391261 (Cited on page 89.)

[125] A. W. Morris, R. J. Akers, J. W. Connor, G. F. Counsell, R. J. Fonck, M. P. Gryaznevich, V. Gusev, T. C. Hender, S. M. Kaye, G. P. Maddison, R. Majeski, T. J. Martin, K. G. McClements, S. Medvedev, Y.-K. M. Peng, C. M. Roach, D. C. Robinson, S. Sharapov, A. Sykes, M. Valovic, M. J. Walsh, and H. R. Wilson, "The role of the spherical tokamak in clarifying tokamak physics," *Plasma Physics and Controlled Fusion*, Vol. 41, No. 12B, pp. B191–B207, dec 1999. doi: 10.1088/0741-3335/41/12b/314. URL: https://doi.org/10.1088/0741-3335/41/12B/314 (Cited on page 109.)

[126] N. T. Howard, C. Holland, A. E. White, M. Greenwald, and J. Candy, "Synergistic cross-scale coupling of turbulence in a tokamak plasma," *Physics of Plasmas*, Vol. 21, No. 11, 2014. URL: https://doi.org/10.1063/1.4902366 (Cited on page 117.)

[127] S. R. Haskey, B. A. Grierson, K. H. Burrell, C. Chrystal, R. J. Groebner, D. H. Kaplan, N. A. Pablant, and L. Stagner, "Measurement of deuterium density profiles in

the H-mode steep gradient region using charge exchange recombination spectroscopy on DIII-D," *Review of Scientific Instruments*, Vol. 87, No. 11, p. 11E553, 2016. URL: https://aip.scitation.org/doi/abs/10.1063/1.4963148 (Cited on page 121.)

[128] J. D. C. William D. D'haeseleer, William N.G. Hitchon and J. L. Shohet, *Flux Coordinates and Magnetic Field Structure: A Guide to a Fundamental Tool of Plasma Theory*. Springer, Berlin, Heidelberg, 1991. URL: https://doi.org/10.1007/978-3-642-75595-8 (Cited on page 122.)